DOT/FAA/TCTT-24/10

Detection of Signatures from Internal Contaminant Sources Using Intelligent Algorithms

April 2024

Technical Thesis

NOTICE

This document is disseminated under the sponsorship of the U.S. Department of Transportation in the interest of information exchange. The U.S. Government assumes no liability for the contents or use thereof. The U.S. Government does not endorse products or manufacturers. Trade or manufacturers' names appear herein solely because they are considered essential to the objective of this report. The findings and conclusions in this report are those of the author(s) and do not necessarily represent the views of the funding agency. This document does not constitute FAA policy. Consult the FAA sponsoring organization listed on the Technical Documentation page as to its use.

This report is available at the Federal Aviation Administration William J. Hughes Technical Center's Full-Text Technical Reports page: actlibrary.tc.faa.gov in Adobe Acrobat portable document format (PDF).

Form DOT F 1700.7 (8-72)   Reproduction of completed page authorized

1. Report No. DOT/FAA/TCTT-24/9	2. Government Accession No.	3. Recipient's Catalog No.
4. Title and Subtitle Detection of Signatures from Internal Contaminant Sources Using Intelligent Algorithms		5. Report Date April 2024
		6. Performing Organization Code
7. Author(s) Saleel Anthrathodiyil		8. Performing Organization Report No.
9. Performing Organization Name and Address Graduate School of the University of Maryland, College Park, MD		10. Work Unit No. (TRAIS)
		11. Contract or Grant No. 692M152240003
12. Sponsoring Agency Name and Address Federal Aviation Administration William J. Hughes Technical Center Aviation Research Division Atlantic City International Airport Atlantic City NJ 08405		13. Type of Report and Period Covered Research Thesis/ Aug 30, 2022- November 30, 2023
		14. Sponsoring Agency Code ANG-E21

15. Supplementary Notes

Thesis submitted to the Faculty of the Graduate School of the University of Maryland, College Park, in partial fulfillment of the requirements for the degree of Master of Science

16. Abstract

Electrical odors and smoke incidents in aviation have become a pressing concern, with over half of the detector activations resulting in false alarms, leading to uncertainties for flight crews. The escalating costs of diversions and growing awareness of associated health risks underscore the need for more reliable detection and discrimination from false alarms. This study harnesses advanced multi-sensor array technologies, intelligent algorithms, and Metal Oxide Sensors (MOS) sensors equipped with AI capabilities to detect and analyze signatures from candidate internal contaminant sources located in the cockpit. Printed circuit boards from avionics, aviation cables of different insulation, and external contaminant sources were put to failure testing to analyze the early fire signatures. These signatures were subsequently assessed using clustering algorithms and multivariate analysis to pinpoint distinct markers. Comprehensive gas analysis and light obscuration measurements further characterized the environment. Experiments were executed at both the University of Maryland and the Federal Aviation Administration (FAA) Technical Center, replicating diverse conditions, including an altitude simulation of 8000 ft. The focus was on the capability to distinguish between samples during the smoldering phase, leveraging a multivariate approach and gas analysis. The study also incorporated Aspirating Smoke Detection (ASD) to characterize the responses during large-scale testing. The findings pave the way for identifying and integrating innovative technologies, achieving accurate detection of early-stage signatures from internal contaminants during potential aircraft smoke events..

17. Key Words		18. Distribution Statement This document is available to the U.S. public through the National Technical Information Service (NTIS), Springfield, Virginia 22161. This document is also available from the Federal Aviation Administration William J. Hughes Technical Center at actlibrary.tc.faa.gov.
19. Security Classif. (of this report) Unclassified	20. Security Classif. (of this page) Unclassified	21. No. of Pages 133 22. Price

ABSTRACT

Title of Thesis:	DETECTION OF SIGNATURES FROM INTERNAL CONTAMINANT SOURCES USING INTELLIGENT ALGORITHMS
	Saleel Anthrathodiyil, Master of Science, 2023
Thesis Directed By:	Professor James A. Milke, Department of Fire Protection Engineering

Electrical odors and smoke incidents in aviation have become a pressing concern, with over half of the detector activations resulting in false alarms, leading to uncertainties for flight crews. The escalating costs of diversions and growing awareness of associated health risks underscore the need for more reliable detection and discrimination from false alarms. This study harnesses advanced multi-sensor array technologies, intelligent algorithms, and Metal Oxide Sensors (MOS) sensors equipped with AI capabilities to detect and analyze signatures from candidate internal contaminant sources located in the cockpit. Printed circuit boards from avionics, aviation cables of different insulation, and external contaminant sources were put to failure testing to analyze the early fire signatures. These signatures were subsequently assessed using clustering algorithms and multivariate analysis to pinpoint distinct markers. Comprehensive gas analysis and light obscuration measurements further characterized the environment. Experiments were executed at both the University of Maryland and the Federal Aviation Administration (FAA) tech center, replicating diverse conditions, including an altitude simulation of 8000 ft. The focus was on the capability to distinguish between samples during the smoldering phase, leveraging a multivariate

1

approach and gas analysis. The study also incorporated Aspirating Smoke Detection (ASD) to characterize the responses during large-scale testing. The findings pave the way for identifying and integrating innovative technologies, achieving accurate detection of early-stage signatures from internal contaminants during potential aircraft smoke events.

DETECTION OF SIGNATURES FROM INTERNAL CONTAMINANT SOURCES USING
INTELLIGENT ALGORITHMS

By

SALEEL ANTHRATHODIYIL

Thesis submitted to the Faculty of the Graduate School of the
University of Maryland, College Park, in partial fulfillment
of the requirements for the degree of

Master of Science

2023

ACKNOWLEDGEMENTS

Table of Contents

List of Tables

List of Figures

List of Abbreviations

AC: Advisory Circular

ICS: Internal Contaminant Sources

ASD: Aspirating smoke detection

FSF: Fire, smoke, or fumes

FAA: Federal Aviation Administration

FAATC: Federal Aviation Administration Technical Center

UMD: University of Maryland

VESDA: Very early smoke detection apparatus

MSEM: Multi-Sensor Environmental Monitors

MOS: Metal Oxide Sensors

QMB: Quartz Microbalance Sensors

FTIR: Fourier Transform Infrared Spectroscopy

GC-MS: Gas Chromatography-Mass Spectrometry

ANN: Artificial Neural Network

E-nose: Electronic Nose

CO: Carbon Monoxide

CO2: Carbon Dioxide

K-Means: K-Means Clustering

KNN: K-Nearest Neighbors

PCA: Principal Component Analysis

CDA: Canonical Discriminant Analysis

SVM: Support Vector Machine

CDAnalysis: Chemometric Data Analysis

NH$_3$: Ammonia

Alc: Alchohol/ Ethanol

CH$_2$O: Formaldehyde

C$_2$H$_4$: Ethylene

PCB: Printed Circuit Board

DAQ: Data Acquisition System

THC: Total Hydrocarbon Content

PC: Principal Component

CV: Cross Validation

HP: Heater Profile

RDC: Repeating Duty Cycle

TVOC: Total Volatile Organic Compounds

1   INTRODUCTION

The detection of signatures originating from the failure of internal contaminant sources (ICS) plays a vital role in proactively identifying potential aircraft fires before they pose substantial risks to both occupants and the aircraft itself while successfully discriminating against the fire and non-fire sources. ICS occurrences primarily result from system failures, internal component malfunctions, and instances of short circuits or overloads in the multitude of cables distributed throughout the aircraft. The comprehensive report by Cherry (2017), consolidated from various aviation incident databases, has emphasized the recurrent incidence of false detector activations on aircraft. Consequently, an efficacious sensor system designed to recognize fire precursors must be able to discriminate between fire-related signatures and non-fire sources (false alarms) while also exhibiting high sensitivity towards the former. Although research endeavors focusing explicitly on aircraft applications in this domain are relatively new, previous projects undertaken at the University of Maryland have attempted to detect fire precursors while successfully distinguishing between pre-fire signatures and nuisance sources (Cestari et al. 2005).

1.1   Motivation and Overview

The primary goal of this research is to enhance aircraft and passenger safety through early detection of fire precursors amidst nuisance sources. The ability of detectors to correctly identify the smoke sources with higher confidence and discriminate from a non-alarming smoke or fire event will enhance the current detection capabilities. By doing so, potential calamities that might threaten passengers, crew, and the aircraft's integrity can be averted. Moreover, the study addresses the prevalent issue of false alarms in current systems, aiming to reduce unnecessary disturbances. Economically, the research aims to curtail the financial losses associated with aircraft fires by preventing extensive damage and potential lawsuits. Unforeseen consequences of onboard fires

include flight diversions, accidents, and personal injuries. Furthermore, the unpredictable repercussions of onboard fires, smoke, and fumes can trigger undesirable outcomes such as flight diversions, accidents, and personal injuries.

1.1.1 Flight Diversion Costs

A comprehensive review from 2002 to 2011 highlighted the financial consequences of these incidents. The financial burden associated with flight diversions is substantial, with widebody aircraft diversions reaching a peak of $105,063 and narrowbody aircraft incurring costs close to $75,804. Importantly, this evaluation revealed that more than half of the expenses tied to all fire, smoke, and fume (FSF) incidents for passenger aircraft were due to these unforeseen landings. This financial evaluation does not encompass potential ancillary costs related to unscheduled landings. These could include, but are not limited to, aircraft damage, injuries to personnel, and expenses stemming from emergency evacuations. Moreover, an assessment of the average yearly cost resulting from unscheduled landings throughout the ten-year study period approximates an expenditure of US$11,000,000. Table 1.1- Reproduced from Cherry (2017) shows the diversion costs.

	Range of Data $ 2016		
	Min	Mean	Max
Regional	958	25,762	50,565
Narrow	1,379	26,159	75,804
Wide	6,859	62,469	105,063

Table 1.1 Range of Diversion Costs [Cherry, 2017]

1.1.2   Emergency Evacuation

Emergency evacuations can result in considerable expenses, predominantly replacing escape slides and subsequent costs linked to potential injuries. According to a report by Cherry (2017), there were 130 incidents involving the deployment of escape slides throughout a 106-month study period, each incident averaging a cost of $68,000. Consequently, the yearly expenditure assessed for removing and replacing escape slides throughout this study period is estimated to be around US$600,000.

1.1.3   Significant Events

Cherry (2017) identified and quantified the significant events that include fire, smoke, or fume occurrences and detector events, notably those that activated the onboard fire or smoke warning system (Cherry, 2017, p. 97) from the incident reporting system database, identified approximately 560 significant events during the study period, with an average occurrence rate of 50 per million flights. Particularly noteworthy was the upward trend in the annual number of all fire, smoke, or fume events in occupied areas of passenger airplanes, averaging about 1,000 incidents per year (Cherry, 2017, p. 25). The prevalence of these incidents on widebody airplanes is likely associated with extended flight duration and increased passenger count, which consequently augments the number of potential fire, smoke, or fume sources. When analyzed based on flight hours, widebody airplanes exhibit an occurrence rate comparable to all passenger airplanes, with regional airplanes showing higher rates. In contrast, narrowbody airplanes demonstrate the lowest occurrence rates per flight and per-hour.

1.1.4 FSF Events by Source

Based on data from Cherry (2017), Figure 1.1 provides an in-depth breakdown of the sources of Fire, Smoke, and Fume (FSF) events in the occupied areas of wide-body, Narrow Body, and regional passenger airplanes. It shows that air systems—including engines, APU, bleed systems, and air conditioning—significantly contribute to FSF events across all aircraft types. Electrical systems are the most common source of FSF incidents, responsible for approximately two-thirds of such events on widebody passenger airplanes, especially when factors like lighting and in-flight entertainment systems are considered.
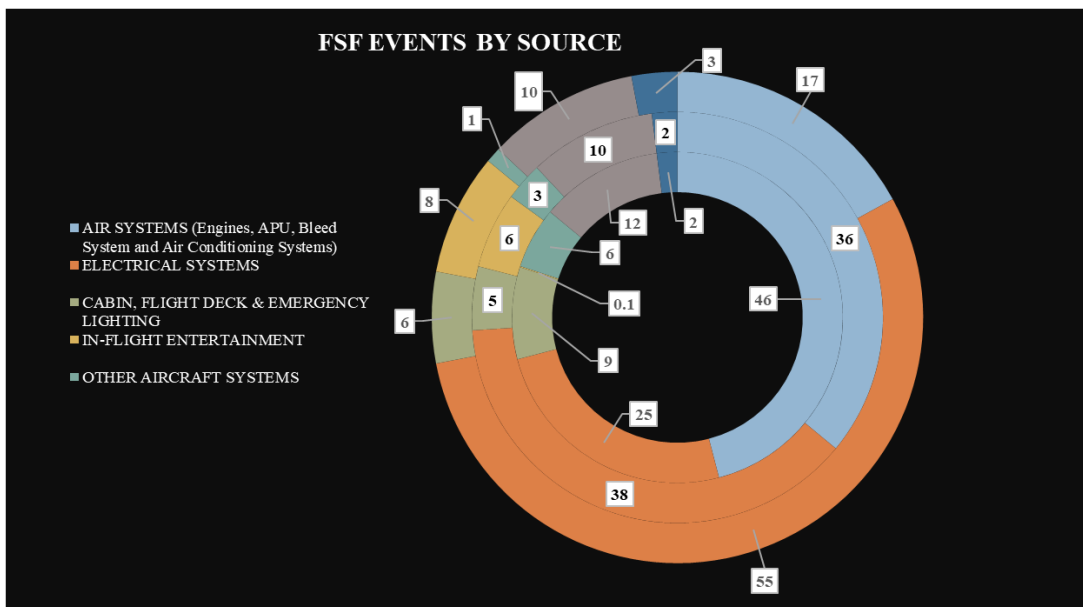
Figure 1.1 FSF Events by the source from Cherry (2017) across various passenger planes, Wide Body Passenger Airplanes (Outer Circle), Narrow Body Passenger Airplanes (Middle Circle) & Regional Passenger Airplanes (Inner Circle)
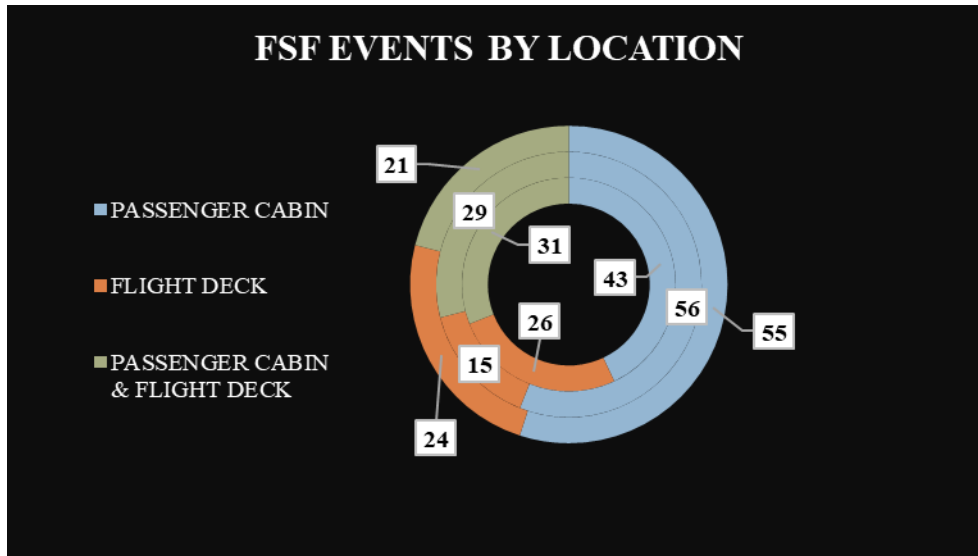
Figure 1.2 - FSF Events by the location from Cherry (2017) across various passenger planes, Wide Body Passenger Airplanes (Outer Circle), Narrow Body Passenger Airplanes (Middle Circle), and regional Passenger Airplanes (Inner Circle)

From the data from Cherry (2017) illustrated in Figure 1.2 - for passenger airplanes, approximately 80% of Fire, Smoke, or Fume (FSF) events trigger manifestations within the cabin, with 50% leading to FSF occurrences on the flight deck. FSF incidents occurring solely in the cabin on regional passenger airplanes are less frequent than their larger counterparts. This reduced incidence is likely due to fewer potential contaminant sources, such as cabin lighting and in-flight entertainment systems, typically found in more limited quantities in regional airplanes.

1.1.6 Proportion Of FSF Events Causing Flight Disruptions

The proportion of Significant Events			
	Passenger Cabin	Flight Deck	Passenger Cabin and Flight Deck
Regional Passenger Airplanes	32%	30%	29%
Narrow Body Passenger Airplanes	39%	41%	46%
Wide Body Passenger Airplanes	20%	35%	35%
	Cargo Bay Main Deck	Flight Deck	Cargo Bay Main Deck & Flight Deck
Freighter Airplanes	42%	33%	43%

Table 1.2 Occupied Areas - Proportion of FSF Events in Passenger Airplanes are Significant [Cherry, 2017]

Reproduced from Cherry (2017, p34), Table 1.2 illustrates the significant events on passenger airplanes that have resulted in flight disruptions. It can be observed that disruptions are more frequently induced by events occurring in the flight deck than those confined to the cabin areas. The urgency to respond to events in the cockpit is heightened due to the presence of critical instrumentation and the potential asphyxiation risks to pilots. Consequently, these events necessitate immediate action, potentially causing more disruptions than those in the passenger cabins, where there may be a more significant window of time to investigate and confirm the nature of the incidents.

1.1.7 Detector Event by Fire, Smoke, And Fume Source

During the study period by Cherry (2017), a comprehensive analysis of FSF detector events across various locations in the airplane was conducted for both passenger and freighter airplanes. It was

shown that there was some reduction in the rate of occurrence of both genuine and false detector warnings, with an average occurrence of 3.6 per million engine flights for all detector events and 2.7 per million engine flights for significant events. Intriguingly, the rate of false warnings was found to be considerably higher in freighter airplanes compared to all categories of passenger airplanes. A similar trend was observed for APUs, with a decline in the annual number of detector events over the course of the study. The data, encompassing all airplanes (passenger and freighter), related to all flight deck announcements, irrespective of cause or consequences. However, the rate of occurrence of APU detector events on freighter airplanes was approximately twice that on passenger airplanes, averaging around 4 per million flights. The study acknowledges the reduction in false warnings, but no firm conclusions could be drawn regarding the underlying reasons or the broader significance of this trend due to the complexity of the parameters. Figure 1.3– shows the trend Analysis of Detector Events by Source at Diverse Aircraft Locations, including engine, APU, Cargo bays, and manned areas, from the data compiled from Cherry (2017).
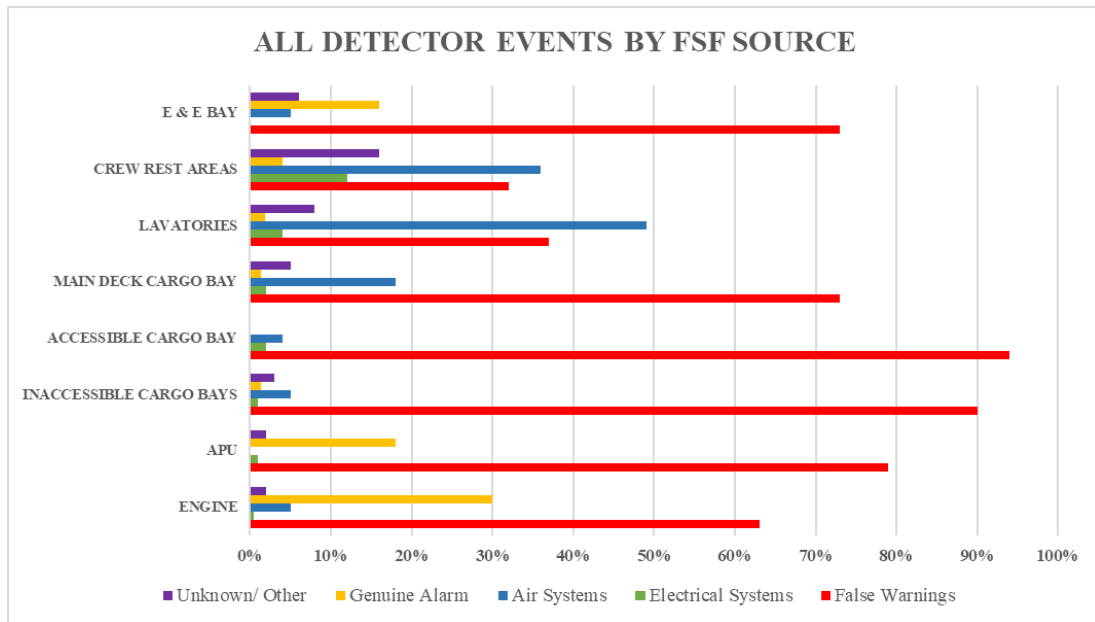
Figure 1.3 Trend Analysis of Detector Events by Source at Diverse Aircraft Locations for both passenger and freighter aircraft

Despite the advancement and increased reliability of fire detection technologies within aircraft systems, the prevalence of false alarms continues to overshadow genuine alarms to a significant extent. This trend has both technical and psychological implications, particularly for pilots and crew members. An accumulation of false alarms may inadvertently lead to a neglect of real alarms in the future, a phenomenon rooted in the psychological response to repeated non-threatening stimuli. According to Breznitz (1984), each false alarm incrementally reduces the credibility of a warning system, a principle articulated in his seminal work, *Cry Wolf: The Psychology of False Alarms*. This underscores the need for continual advancements in detection systems, striving for greater reliability and sensitivity. Such progress is essential to maintaining confidence in these systems and, more importantly, safeguarding property and lives in complex, high-value applications.

1.2 Fire Detection Technologies

A comprehensive understanding of commercially available fire detection technologies is essential in evaluating fire safety measures and strategies. This section provides an overview of the various detection mechanisms used in the study. By scrutinizing these technologies, the study aims to contribute valuable insights to the ongoing dialogue on fire safety and prevention, aligning the empirical findings with the broader goal of enhancing fire safety.

1.2.1 Gas detectors

Gas-sensing fire detectors are specifically designed to identify the presence of particular gases that may be emitted during a fire. Unlike traditional smoke detectors that detect particles, gas sensing detectors operate on the principle of identifying certain combustion byproducts, such as carbon monoxide (CO), carbon dioxide (CO_2), or other fire-related gases. These detectors can provide an

23

early warning of a fire, even before smoke is visible, making them particularly valuable in environments where early detection is crucial. Gas sensing detectors can also be less prone to false alarms from cooking or dust, as they are tuned to specific gas signatures associated with the foreseeable sources in particular locations. The choice of sensor technology may vary depending on the specific gases to be detected and can include electrochemical, semiconductor, and infrared sensors. These advanced technologies contribute to the accuracy and reliability of gas-sensing fire detectors, enhancing overall fire safety and protection. By utilizing the gaseous signatures of fires, an innovative system incorporating multiple gas sensors, Taguchi sensors, and thermocouples has been developed to enhance fire detection capabilities. This integrated approach allows for precise detection and differentiation between different types of fires, such as flaming and smoldering fires (Hagen et al., 2000).

1.2.2   Aspirating smoke detectors

As a significant interest point in this study, aspirating smoke detectors (ASD), also known as air-sampling smoke detectors, were utilized as a part of the advanced early warning detection mechanisms. Representing a cutting-edge approach, ASD provides solutions where conventional methods may not be sufficient. These detectors consist of a tubing network that draws air samples into a central detection unit at a distance from the protected area. Once inside the detection unit, either a laser or LED light source interacts with the air sample, and a sensor assesses the ensuing scattering or obscuration of light by smoke particles. Both conventional and addressable systems of ASD are available in the market.

In a specific test conducted at a warehouse measuring 43 m in length and 12 m in width, resulting in a gross floor area of 516 m^2, the ASD system was evaluated alongside conventional smoke detectors and projected beams. Various smoke sources, including liquid heptane (100 ml), timber,

24

and smoke pellets, were used to mimic real-world fire conditions. The results revealed that the ASD system outperformed both the conventional and projected beam detectors. When conventional spot-type detectors responded, the ASD system was found to have responded an average of 52.2 seconds earlier, underlining its superior early detection capabilities (Tylor et al., 2016). Figure 1.4 - illustrates an example configuration of a VESDA network.
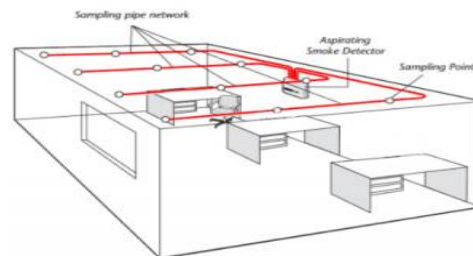
Figure 1.4 An example VESDA Network. Reproduced from PHF Fire

1.2.3   Applicability of different detector technologies

In recent years, there has been a substantial focus on enhancing fire detection methodologies within aircraft, particularly in cargo compartments and other unoccupied areas. This interest is driven by the increased use of composite materials and Li-ion battery-powered devices, fueled by the changes in fire safety regulations in 2019 with a focus more on performance-based approaches. A comprehensive body of research has evaluated fire detection technologies and their challenges under flaming and smoldering conditions to assess their reliability and effectiveness (Milke et al., 2017). These studies have contributed to the advancement of detection technologies and explored the challenges and applicability of various methods. A detailed comparison of the different smoke detection methods reproduced from the work of Milke et al., (2017), including their respective responses and limitations, is provided in Tables 1.3 and 1.4.

Technology	Sensitivity – Flaming Fires	Sensitivity – Smoldering Fires	Nuisance alarm susceptibility	Maintenance
Ionization	H	M	H	H
Photoelectric	M	H	M	M
ASD	H	M-H	M	H
Projected beam	M	H	M	H
Video	H	H	M	H
Spot heat	H	L	L	L
Linear heat	H	L	L	L
Radiation	H	L	L	H
Gas	M-H	M-H	H	H
H- High, M- Moderate, L- Low				

Table 1.3 Applicability of fire detection technologies for commercial aircraft [Milke, 2017]

Technology	Principal Challenge
Ionization	Nuisance alarm susceptibility, modest response to smoldering fires
Photoelectric	Modest response to flaming fires with limited visible smoke
ASD	Maintenance of filters
Projected beam	Maintenance of photo-receiver, provision of a clear pathway for the light beam

Video	Provision of clearance space for viewing, lighting
Spot heat	Slow response to smoldering fires
Linear heat	Slow response to smoldering fires
Radiation	Maintenance of optics
Gas	Stability of sensors

Table 1.4 Challenges in applying detection technologies in commercial aircraft. [Milke, 2017]

1.2.4 Fire Detection and Smoke Testing Protocols for Aircraft

FAA identifies different probable onboard smoke sources, highlighting failures of electrical equipment due to short-circuited wires and overheating of devices due to the loss of thermostats or controlling mechanisms (FAA, AC-25-9A). Airplanes with a passenger capacity of 20 or more must be equipped with specific signaling mechanisms for alerting the flight crew to a fire in an isolated, non-occupiable room (Title 14, Chapter I, Subchapter C, part 25). These regulations also outline requirements for lavatories, mandating smoke detection systems that provide warnings in the cockpit or visible/audible warnings in the passenger cabin (14 CFR, 25.854). Furthermore, standards for cargo or baggage compartment smoke or fire detection systems stipulate the provision of visual indication within one minute of fire detection and to detect a fire at temperatures below those that would threaten structural integrity (14 CFR, 25.858).

The advisory circular emphasizes protection against continuously generated smoke in the cockpit through smoke evacuation procedures, and it also suggests a smoke detection system for the crew rest area to minimize hazards. Various materials can be used as test fuels as per the advisory

circular, for smoke detection tests, including plastic, paper, rags, burlap, and any other acceptable fuels. One of the backgrounds for these smoke detection tests is that fire detection systems in cockpits must be able to provide a warning before the fire reaches an uncontrollable state or causes damage to liners, wiring, equipment, structure, essential systems, or other critical components. (FAA, AC 25-9A). The current guidelines do not specifically encompass various avionics, which are heavily utilized and have been frequent sources of smoke or fumes in aircraft. The avionics and wiring used in the cockpit have been the primary focus of this study.

Furthermore, while 25-9A's smoke detection testing includes only smoldering tests, the UL 268 Smoke Detectors for Fire Alarm Systems mandate testing in flaming and smoldering modes (UL, 268). The smoldering combustion test, conducted in a chamber filled with smoke from smoldering fire, requires the detector to alarm within 10 minutes of the test's start. Conversely, in the flaming combustion test, where the chamber is filled with smoke from a flaming fire, the detector must alarm within 3 minutes of the test's initiation according to both standards (NFPA, 72; UL, 268). This comprehensive overview of standards and practices underscores the complexity and significance of managing smoke detection and control in aviation, reflecting ongoing efforts to enhance passenger safety and operational efficiency.

1.3 Electronic Nose (E-nose) Technology

An Electronic Nose (E-nose) is an advancement in detection technologies that emulate the human sense of smell. It is specifically designed to detect odors and identify their components based on a set of signature training data. Just as the human nose recognizes smells through unique sensory patterns, the E-nose classifies odors according to corresponding signature patterns associated with various samples. The need for measuring the particulates in a sample makes the sensory techniques

complex as compared to measuring various forms of energy. The core of the E-nose's functionality resides in its mechanism for analyzing the chemical composition of the samples. This mechanism comprises an array of different sensors, each reacting to specific chemical signatures tied to different samples. Each sensor's response contributes to a collective pattern is used in detecting the odor. Once this pattern is established, the E-nose employs a recognition system, such as a trained neural network, to identify new samples. By comparing the detected pattern with stored signatures in its database, the E-nose can discern and categorize various samples, including toxic and odorless ones.

The three crucial parts of an E-nose system are: -

- Sampling System: This component uses an aspirating pump within the device housing to draw the targeted components toward a sensor array. Some E-nose configurations also collect ambient conditions before measuring the sample, allowing them to obtain a baseline for comparison.

- Sensor Array: Housed within the device, a diverse set of sensors reacts with the target gases, and the system records the responses. The sensor configurations can vary, including but not limited to Metal Oxide Sensors (MOS), Polymer composite sensors, and Electrical conductivity sensors.

- Pattern Recognition: After capturing the responses from the sensor array, the system proceeds to analyze and identify the target sample. Various pattern recognition techniques are employed for this purpose, such as Artificial Neural Networks (ANNs), support vector machines (SVMs), clustering analysis, and Principal Component Analysis (PCA). These methods facilitate the system's ability to discern specific odors by interpreting the unique signature patterns corresponding to each sample.

E-nose systems predominantly operate in two distinct modes: training and prediction (Sensigent, n.d.). During the training mode, the sensors are exposed to target gases/ samples, forming a vast and comprehensive training set. This preparation serves to acquaint the sensors with various chemical signatures, facilitating subsequent stages of neural network training. Once the sensory data is collected, they undergo post-processing and are fed into a training algorithm. Various neural network methods/clustering analyses may be employed to construct a robust predictive model during this phase. Then it can be run in prediction mode, allowing the E-nose to identify specific chemical species. The system refers to the training set and utilizes the algorithms developed during training to recognize and classify the gases of interest.

2   LITERATURE REVIEW

2.1   Historical Overview of In-Flight Fire Incidents

The tragic incident involving Swissair Flight MD-11 on September 2, 1998, which claimed the lives of 215 passengers and 14 crew members, served as a significant catalyst for research into smoke and fumes within aircraft cabins. The investigation into this catastrophe revealed that a fire originating on the upper right side of the cockpit caused the crew to lose control of the aircraft. This fire was subsequently identified as having been sparked by a short circuit wire arcing event that ignited the thermal and acoustic insulation cover materials (Transportation Safety Board of Canada, 1999). This incident's tragic loss of life emphasized the critical importance of fire detection and suppression within aircraft. Consequently, there has been substantial progress in these areas, with a marked increase in research and development aimed at improving systems for detection and monitoring.

Another distressing event was the crash of EgyptAir Flight 804 on May 19, 2016, resulting in the deaths of 56 passengers and ten crew members. Investigators believe that a fire in the cockpit led to this tragic loss. Similarly, the devastating crashes of UPS Flight 6 in 2010 and Asiana Flight 991 in July 2011 were traced back to fires originating in cargo compartments. These regrettable incidents serve as stark reminders of the need for early warning and detection systems in aircrafts. Consequently, these tragedies have galvanized the aviation industry's efforts to enhance safety measures and mitigate the risks associated with onboard fires. The industry's ongoing commitment to research, technological innovation, and regulatory compliance reflects an acute awareness of the dire consequences of failing to adequately address these critical safety concerns and never-ending challenges within the industry.

2.2 Aircraft Air Quality: Contaminant Sources, Implications, and Monitoring Technologies

In an aircraft, contaminants can be broadly classified into external and internal sources according to their origin. Both categories play a crucial role in affecting air quality within the cabin and flight deck, and their understanding has significant implications for safety and health regulations. External Contaminants can enter the aircraft through engines or the Auxiliary Power Unit (APU). External contaminants might also encompass substances outside the airplane, such as deicing fluid, engine/APU lubricating oil, and various fumes. Internal sources of contaminants are present within the cabin or flight deck. Examples include occupants, electronics, food and drink, and carry-on bags. (FAA *Reauthorization, 2018)*. A notable area of concern highlighted by this study is the of avionics components and wire insulations in the cockpit. Fires involving energized electrical equipment containing PCBs could release vapors from burning PCBs and other toxic byproducts of combustion, such as polychlorinated dibenzo-p-dioxins (FAA *Reauthorization, 2018).*

E-noses or multisensor array techniques have been explored for cabin air quality monitoring and measurement in the past. A particular sensor array mechanism, Aerotracer, developed by AIRSENSE Analytics, is utilized by maintenance crews to detect, and identify common Volatile Organic Compounds (VOCs). It is sensitive enough to classify odor concentrations on a sensing scale, which enables the identification of the odor's source. (Kos et al., 2018). Notably, Aerotracer's deployment is primarily during maintenance rather than in-flight operations, limiting its real-time monitoring capabilities.

2.3   Trends and Analysis of Fire, Smoke, and Fume Events in Commercial Aircrafts

The study by Cherry (2017) focused on the analysis of fumes, smoke, and fire (FSF) events on airplanes from the period of 2002 to 2011, and it examined a total of 145,32 events. Within this dataset, 38% of the events were identified as significant according to the criteria established in the study. The average number of significant events per year stood at approximately 560, translating to an average occurrence rate of 50 per million flights. Additionally, the study revealed an upward trend in the annual number of all FSF events, increasing from a range of 800 in 2002 to 1400 in 2011 (Cherry, 2017). This increase could be attributed to the growth in air traffic during the corresponding years. When considering only significant FSF events in occupied areas, the average rate of occurrence for regional and narrow-body airplanes was found to be roughly 30 per million flights, and for wide-body passenger airplanes, it was approximately 80 per million flights.

Air systems (engines, APU, bleed systems, and air conditioning systems) are reported to be the predominant sources of fire, smoke, and fume events in occupied areas of both passenger and freighter airplanes. However, the electrical systems are reported as the most frequent source of FSF, with approximately two-thirds of occurrences attributed to this source on wide-body passenger airplanes, mainly when lighting and in-flight entertainment systems are considered. When examining the location of FSF events in the occupied areas of all passenger and freighter airplanes, the data suggests that approximately 80% of events result in FSF within the cabin, while 50% of the events lead to FSF on the flight deck. In contrast, for freighter airplanes, the majority of FSF events are reported to occur on the flight deck. Around 25% to 30% of all FSF events in the occupied areas for passenger and freighter airplanes resulted in an unscheduled landing (Cherry, 2017).

The analysis yields that, among all passenger and freighter airplanes, approximately 40% of false warnings originating in the engine bay led to unscheduled landings. Further examination of the data reveals a decline in the cumulative rate of occurrence of false warning detector events in inaccessible cargo bays for freighter planes, from a range of 15 to 5 per million flights between 2003 and 2011. This rate aligns closely with that observed for passenger planes by 2011. For passenger airplanes, approximately 2% of these events are caused by fire, smoke, or fumes within the lavatory. Additionally, the proportion of false warnings for the detector events in the lavatories is found to be approximately 37% for all events and 21% for significant events (Cherry, 2017).

2.4 Smoke Particle Dynamics and Aircraft Bleed Air Contamination: Insights from Recent Studies

In a study by Fabian and Gandhi (2008), the authors analyzed the mean particle diameter for smoke emanating from flaming and non-flaming fires. They found that when producing a light obscuration of 0.5%/ft, the mean particle diameter ranged from 0.08 to 0.22 µm. Despite the consistency in the level of light obscuration across these smokes, they noted a variance in detectability by light scattering or ionization detectors. This variation is attributable to the fact that these detection technologies depend on the particle diameter's square and first power, respectively. Figure 2.1 - representing these findings was reproduced from the work of Fabian et al. (2007) as part of the smoke characterization project.
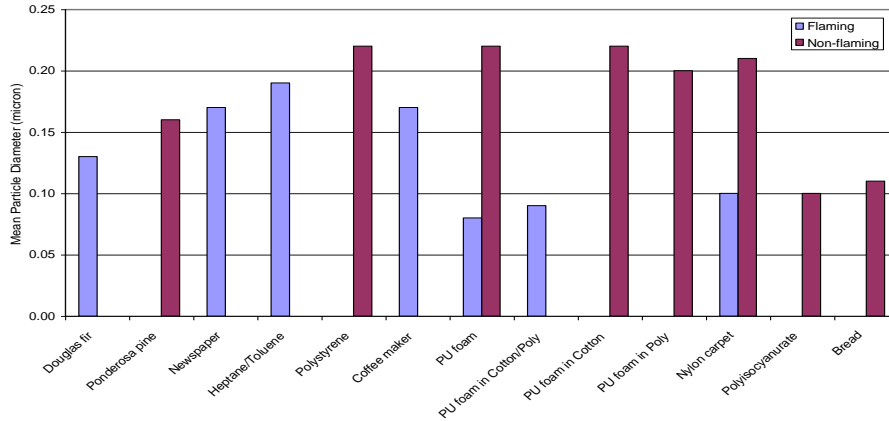
Figure 2.1 Mean particle diameters for light obscuration of 0.5 %/ft [Fabian, et al., 2007]

Milke et al. (2008) combined the previous studies to characterize the smoke detector responses and reviewed a compilation of experimental programs that utilized various fuels and were conducted in different spatial dimensions. Despite these variations, the 80th percentile values for obscuration levels at smoke detector response were mostly similar, except for ionization detectors in non-flaming tests by NIST. For flaming fires without forced ventilation, obscuration levels ranged from 1.4 to 10.7 %/ft for ionization detectors and 2.7 to 12.9 %/ft for photoelectric detectors. With ventilation, the 80th percentile values differed notably between the two technologies. For non-flaming fires without ventilation, the values ranged from 4.4 to 18.5 %/ft for ionization and 1.6 to 12.1 %/ft for photoelectric detectors. Excluding the NIST study, suggested guidelines for obscuration level could be 12 %/ft for ionization detectors and 10 %/ft for photoelectric detectors. Figure 2.2 - Show the 80th percentile obscuration level at detector response in various smoke characterization programs.

35
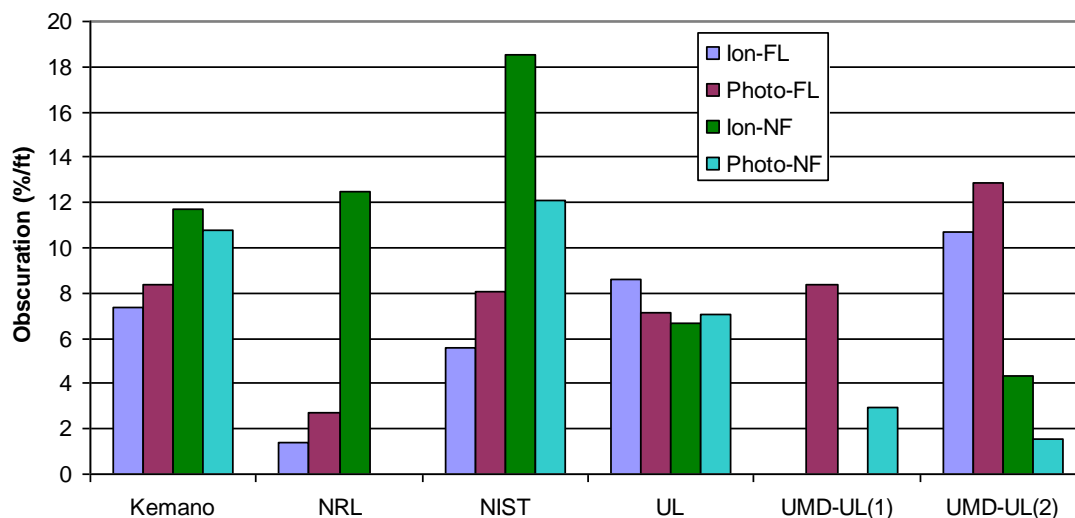
Figure 2.2 80th percentile obscuration level at detector response in various smoke characterization programs. [Milke et al., 2008]

Overfelt and Jones (2012) discuss the principal contaminants from an aircraft bleed air supply. These contaminants could be aerosolized droplets of a Jet engine or APU lubricating oil, along with partially or fully pyrolyzed byproducts of combustion of the working fluids (Overfelt and Jones, 2012). Table 2.1 reproduced from the report, details the probable contamination event and the corresponding contaminant. Furthermore, Table 2.2 explores the commercial sensor technology available to detect these contaminants. The target contaminant sources under investigation in this study differ from those explored in earlier bleed air quality research. However, there are similarities in the methods employed, particularly in using sensing technologies. Some of the technologies utilized in the multisensory array for this investigation overlap with those implemented in previous studies.

Potential Bleed Air Contamination Event	Probable Contaminant
Engine oil leak producing aerosolized droplets of oil in the engine compressor.	• Very fine mist of engine oil aerosols • Small amounts of carbon monoxide (CO) and carbon dioxide (CO2)
Partially pyrolyzed jet engine oil	• Very fine mist of engine oil aerosols • Carbon monoxide (CO) • Carbon dioxide (CO2) • Misc. unburned hydrocarbons • Ultrafine smoke particles
Fully pyrolyzed jet engine oil	• Carbon monoxide (CO) • Carbon dioxide (CO2) • Ultrafine smoke particles

Table 2.1 Summary of Potential Bleed Air Contaminants [Overfelt et al., 2012]

Possible Bleed Air Contaminant	Commercial Sensor Technology
Engine oil aerosols Ultra-fine smoke particles	Light scattering photoelectric detectors (dia>0.5 μm) or ionization detectors (dia<0.5 μm) depending upon the aerosol/particle size distribution
Carbon Monoxide (CO)	Electrochemical cell sensor with selectivity optimized for CO
Carbon Dioxide (CO2)	Non-dispersive Infrared (NDIR) sensor optimized for CO2)
Misc. unburned hydrocarbons	Catalytic bead sensor OR photoionization detector depending upon the specific hydrocarbon(s) to be detected

Table 2.2 Possible Bleed Air Contaminants and Potential Sensor Technologies [Overfelt et al., 2012]

2.5   Advancements in Fire Detection: Multi-Sensor Integration and Algorithmic Approaches

Milke (1999) explored multiple fire signatures with integrated intelligence to improve fire detection speed and accuracy. By combining CO and CO2 sensors, the device could efficiently differentiate between flaming and non-flaming fires based on their respective gas concentration rates. Milke and Zevotek (2016) further examined the responses of smoke detectors to signatures from cooking activities. Their experimental approach encompassed a range of measurements, including CO, CO_2, and an array of smoke detector technologies. This array comprised ionization, photoelectric, and advanced algorithm ionization smoke detectors. They posited that combining multiple sensors with an intelligent algorithm could optimize the response time. To maximize the available reaction time and deliver the most promising precursor signal, an algorithm can be formulated that harnesses essential gas temperature and optical density values. This strategy would ensure the timely detection of potential cooking fires while reducing the likelihood of nuisance alarms.

On the earlier work for a multidimensional sensor for gas analysis, Muller and Lange (1986) verified a sensor array's capability to accurately detect and differentiate between three distinct gases. Given the high efficacy of recognition demonstrated, it is postulated in their work that this methodology can be scaled to identify a more extensive array of gases. It is evident from the findings that an optimal chemical sensor system should encompass an array of sensing elements. Ideally, each of these sensors should exhibit sensitivity to all target gases. A crucial criterion is that any cross-sensitivities among these sensors should maintain linear independence. Moreover, preliminary evaluations in the study indicated that even basic pattern recognition methodologies, such as the computation of correlation coefficients, are notably efficient in discerning pertinent

insights from the array of signal spectra. Moriizumi, Nakamoto, and Sakuraba (1992) studied pattern recognition for electronic noses, focusing on utilizing Artificial Neural Networks (ANNs). Their study revealed the effectiveness of the backpropagation algorithm in differentiating aromas specific to alcoholic beverages. Additionally, they examined the potential of the Fuzzy Learning Vector Quantization algorithm in odor discrimination. The research also confirmed that analog BP-ANN (Backpropagation - Artificial neural network) hardware, when paired with tin oxide sensors, showed significant prowess in gas discrimination.

Ramesham et al., (2001) used a Cyranose E-nose equipped with 32 conductive polymer sensors to detect outgassing species emerging from wire insulation under induced thermal stress. Remarkably, the E-nose demonstrated the capability to detect the corresponding signatures within a rapid timeframe of 5 to 20 seconds during the experimental tests. Fujinaka et al. (2008) verified an intelligent electronic nose system designed with 8 MOGS (Metal Oxide Gas Sensor) to detect fires at an early stage. The system demonstrated the ability to identify fire sources during their initial stages with a 99% accuracy rate. Additionally, results derived from multivariate K-Means algorithms indicated a 98% accuracy in predicting the sources. In a study by Scorsone et al. (2006), an effort was made to develop an electronic nose for fire detection by initially exploring the chemical markers from different types of smoke using GC-MS and FTIR analysis. Their findings highlighted that the chemical compositions of various smokes are distinct enough to differentiate between fire and non-fire events. During a test with smoldering wood, the response time of the electronic nose's CP sensors was about 350 seconds. This timing closely mirrored the detection timings recorded by the FTIR analyzer for the primary five chemical species and the initial detection by the optical detector. Notably, Carbon Monoxide (CO) was detected in just 200

seconds. A critical observation arose when a standard optical detector raised a fire alarm approximately 600 seconds after the wood ignited in the fire cabinet.

In a comprehensive study by Ni et al. (2008), the potential of a digital nose in early warning systems for electrical fires was examined. The team investigated the off-gassing under thermal stress from various insulations to gauge the early detection capabilities and evaluated the discriminative abilities of the sensor array using multivariate analyses such as PCA and KNN algorithms. This electronic nose was equipped with an 11-sensor array, which included electrochemical sensors, quartz microbalance (QMB) sensors with distinct polymer coatings, and heated metal oxide sensors (MOS). It was observed that the best performance was achieved using the electrochemical and MOS sensors. The E-nose model displayed a higher tolerance to random discrepancies in the MOS sensor readings than in the electrochemical sensors. Prolonged drifts in the MOS or electrochemical sensor responses barely influenced the accuracy of the E-nose. Also, they identified a difference in vapor compositions generated from electrical versus non-electrical heating through mass spectra analysis, emphasizing the potential of the sensor array in differentiating between electrical fires and other types of fires.

3   <u>RESEARCH AND METHODOLOGY</u>

3.1   Introduction

The primary focus of this study is on the possible internal contaminant sources found within aircraft cockpits. In collaboration with the FAA Fire Safety Branch and through industrial donations, samples were collected for various avionic components, wire insulations, and other potential nuisance sources commonly present in aircraft environments.

The research methodology was delineated across three distinct experimental setups, each conducted in different locations and chambers of varying sizes:

1. An initial small-scale test occurred in a closed chamber at the University of Maryland's Fire Protection Engineering, Koffel Lab.

2. This was followed by large-scale experiments in a simulated cockpit mockup, mirroring the volume specifications of a Boeing 737 at the FAA William J. Hughes Technical Center in New Jersey.

3. The third setup involved testing in a reduced pressure vessel, where the internal air pressure was maintained at 10.9 psi, replicating cabin pressure at 8,000 ft at the FAA tech center.

In each experiment, a standardized procedure was employed to systematically induce thermal impact into the samples, facilitating the generation of specific signatures. These signatures were subsequently analyzed using an array of sensors. The collected data was then processed through multivariate analysis for a more in-depth understanding and insights.

3.2   Experimental Design and Data Acquisition

3.2.1   UMD Test Chamber

The experiments were conducted using a test chamber designed for the ASTM E662 - Standard Test Method for Specific Optical Density of Smoke Generated by Solid Materials (ASTM E662, 2021). The chamber dimensions were 0.9144 m in height, 0.9144 m in width, and 0.6096 m in depth, offering a total volume of approximately 0.52 m^3. To safeguard against any potential overpressure events, the chamber was equipped with a blow-out panel, secured with aluminum foil, covering 806.45 cm^2. A radiant heater featuring a 2.54 cm diameter opening was installed within the chamber. Samples were positioned vertically, 2.54 cm from the heater's center, through a sample holder that could be controlled from the outside. The furnace was situated along the chamber's centerline, equidistant from the front and back sides of the chamber. The opening of this furnace faced toward the chamber's right wall, positioned approximately 30.48 cm away. The furnace's centerline was elevated, approximately 19.68 cm above the chamber's floor. The radiant heater was calibrated to exert a 25 kW/m^2 heat flux. Samples subjected to this heat had an average exposed area of 16.5 cm^2, with a total area of 19.35 cm^2. A 91 cm segment of Ultra chemical-resistant Tygon tubing was employed to transport gaseous signatures from the containment box to the electronic nose (E-nose). To avoid damage to the internal filters in the E-nose, an inline filter with a pore size of 0.22 μm was integrated within the pathway on the tubing upstream from the chamber. The wiring connections for the cable insulation tests were channeled through a vent on the chamber's front side. Additionally, the experimental setup included a photometric system designed to assess light obscuration levels for the smoke from the samples through a Data Acquisition (DAQ) system. Figure 3.1 – shows the small-scale experimental setup.
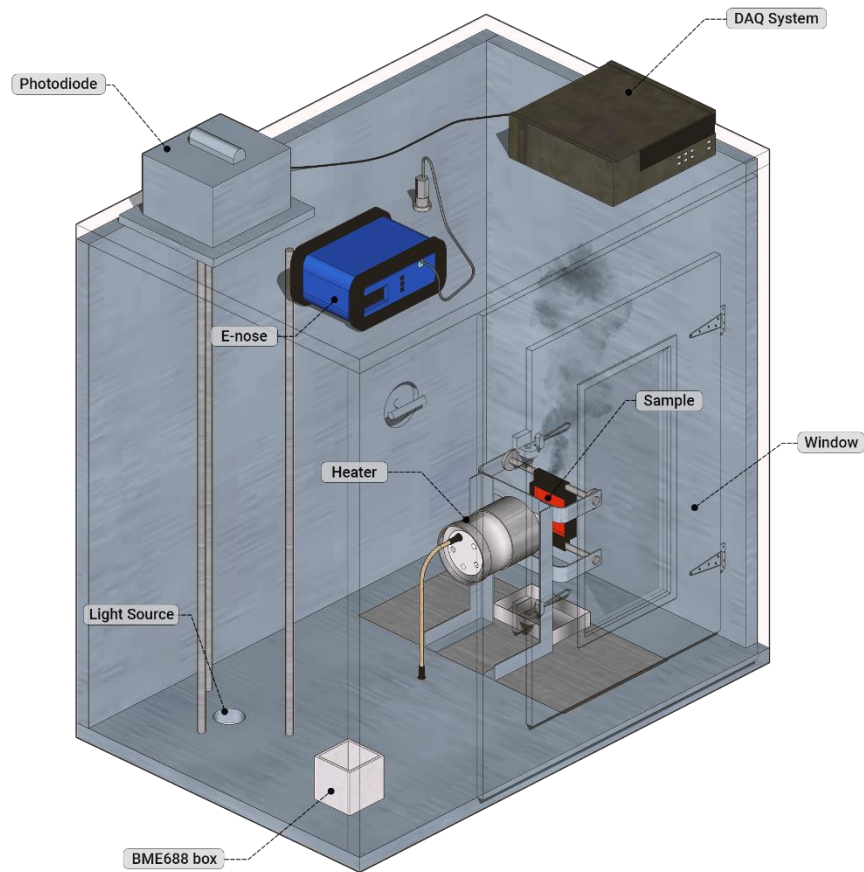
Figure 3.1 UMD Experiment Box

3.2.2   Multi-Sensor E-Nose

The MSEM-160 digital nose, manufactured by Sensigent LLC, was utilized predominantly for this research. This battery-powered portable device incorporates various sensor technologies and data fusion algorithms to measure and assess samples effectively. Relying on Sensigent's proprietary NoseChip technology, the MSEM-160 features an array of up to 32 sensors, including nano-composite sensors (NCA), electrochemical (EC), metal oxide semiconductor (MOS), photoionization (PID), as well as temperature and humidity sensors. The instrument houses an air sampling pump with a 0.4 LPM capacity to draw the samples into the sensor system. The data is

manually processed to identify the gases. But it continuously records the THC, odor, and other calibrated gases like NH_3, H_2S, CH_2O, and C_2H_4. Odor units were measured in OU/m3 as defined as per EN13725 (EN13725, 2022), where 1 OU = 0.04 ppm 1- butanol. Two filters are used inside the MSEM, to clean the sensors with clean air after the measurement. One single bed air filter containing a granular activated carbon purge 1 and a combination of activated carbon and a 13x molecular sieve for the mixed bed into purge 2. The filtered and outside air flow is controlled by an instrument valve and monitored through operating software.

The E-nose instrument is equipped with an air sampling pump with a capacity of 0.4 LPM, engineered to channel the samples directly onto the integrated sensor array. Although the data necessitates manual processing for gas identification using the E-nose system, the system offers continuous logging capabilities, recording parameters such as Total Hydrocarbon Content (THC), odor, and other specifically calibrated gases, including NH_3, H_2S, CH_2O, and C_2H_4. The MSEM is supplied with a factory calibration for chemical sensors based on EN13725 and ASTM E544. Table 3.1, reproduced from Manufacturer (2022), displays the corresponding sensor array and cross-sensitivity, while Figure 3.2 presents an image of the Sensigent© MSEM 160 E-nose.

Sensor	Type	Range, ppm	Limit, ppm	Cross-Sensitivity
TVOC	PID	0-200	1000	VOC
ODOR	MOS, NCA	0-2000	5000	Hydrocarbons, VOC, reducing gases, oxidizing gases
Hydrogen sulfide, H2S	EC	0-50	100	NH3 0, CH3SH <10%,

				NO2 <20%, SO2 <10%
Ammonia, NH3	EC	0-100	100	H2S, SO2, NO2, Cl2
Ethene, C2H4	EC	0-10	20	CO ,60%
Formaldehyde, CH2O	EC	0-10	30	CO 15%, H2 2%, alcohols

Table 3.1 MSEM Sensors cross-sensitivity to other gases
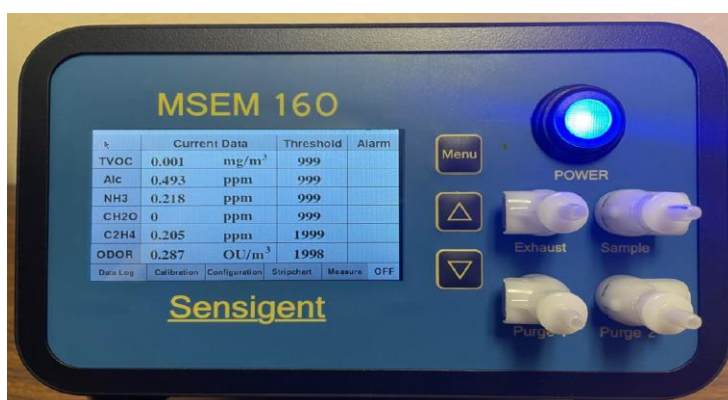
Figure 3.2 MSEM 160 E-nose

The sensor array consists of 32 sensors, each serving a specific function for the E-nose. A detailed list of these sensors and their primary purposes can be found in Table 3.2.

Type Of the Sensor	Primary Purpose
Dew Point	Moisture measurement
TVOC	Gas detection
ODOR	Gas detection
Alc (EC Sensor)	Gas detection

NH$_3$ (EC Sensor)	Gas detection
CH$_2$O (EC Sensor)	Gas detection
C$_2$H$_4$ (EC Sensor)	Gas detection
MOS	Pattern Identification
PID	Pattern Identification
Poly Composite	Pattern Identification

Table 3.2 MSEM Sensor Configuration

3.2.3 Bosch BME-688 gas sensor

The Bosch BME688 is a new electronic nose technology development with a Bosch© BME series of environmental monitoring sensors. This sensor has multiple capabilities like gas detection, humidity measurement, pressure sensing, and temperature monitoring within its compact form factor with a size of 3 X 3 X 0.9 mm^3 and a sensitivity to a wide spectrum of volatile organic compounds (VOCs). A unique proposition of the BME688 is its integration with Bosch's proprietary AI suite., which can train the neural network with different classes of samples. This helps the sensor integrate with the Internet of Things (IoT) and real-time monitoring in interconnected systems. Figure 3.3 shows the image of a BME688 sensor.
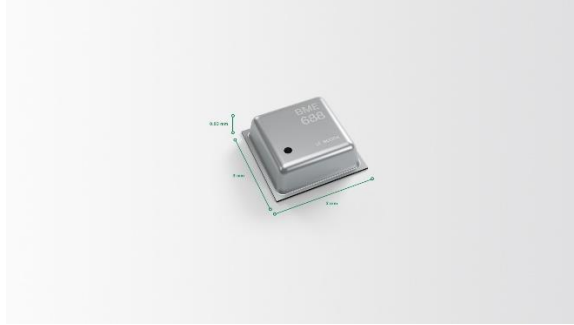
Figure 3.3 Bosch BME688 sensor

Bosch's AI Studio offers an interface to assist users in developing algorithms tailored for specific applications using the BME688 development kit. This platform, underpinned by programming in Python, leverages leading-edge machine-learning technologies like TensorFlow, Keras, and NumPy. The technical specifications of the BME688 sensor are provided in Table 3.3.

Parameter	Technical Specifications
Pressure	300 – 1100 hPa
Humidity	0 – 100%
Temperature	-40 – 85 degree C
Interface	12C and SPI
Gas Sensor power consumption	< 0.1 mA in ultra-low power mode

Table 3.3 BME688 Technical data

The BME688 development kit, an array of 8 BME688 sensors, can be integrated with the BME AI-Studio Software, ensuring tailored optimization of performance, output data rate (ODR), and power consumption based on specific application requirements. The kit's architecture incorporates eight BME688 sensors, an Adafruit© HUZZAH32 Feather board powered by an ESP32

microcontroller unit (MCU), a MicroSD card slot for data storage, and a CR1220 coin cell battery dedicated to clock operations. The development kit can be connected to Bosch's BME AI mobile application through Bluetooth for gas analysis.

3.2.4 Data Collection and Processing

The signatures from the internal contaminant sources were generated from identified samples using two different thermal stress methods depending on the sample. These signatures were subsequently monitored using the E-nose. Initially, the E-nose operated in training mode to gather sensor data. This data was then processed manually to develop an algorithm through multivariate analysis using the proprietary software from Sensigent, culminating in a trained algorithm for future predictions. The samples were then tested in similar conditions to test the prediction capabilities of these algorithms. The BME688 followed a similar methodology. However, its training data was processed via the Bosch AI Studio, generating tailored algorithms. These algorithms were subsequently tested using the Bosch BME mobile studio or an integrated development environment (IDE) employing the BSEC library.

3.2.5 Large-Scale Testing at the FAA Tech Center

The large-scale testing took place at the testing space of FAATC designed to mimic the cockpit volume of a Boeing 737. This mock setup comprised a rectangular chamber with dimensions 2.0 m x 1.82 m x 1.82 m. Though constructed from plywood, the chamber's interior was well insulated with an aluminum coating to offer a representative and protective environment.

- Chamber Specifications:
  - Exterior Construction: Plywood
  - Interior Layer: Aluminum
  - Dimensions: 2.0 m x 1.82 m x 1.82 m

- Access Points:

  - A top opening, which served as an exhaust during venting.

  - A side wall opening to facilitate chamber access.

  - Power and light were available inside the space.

- Heating Mechanism:

  - Employed a heater set to a heat flux of 25 kW/m^2, consistent and similar to the conditions used in the small-scale tests.

- Gas Analysis Capabilities:

  - Gas analyzer used to analyze CO, CO_2, and O_2 concentrations in the chamber.

  - Measurements were taken both at a height of 1.7 m from the floor.

- E-nose Instrumentation:

  - The MSEM sampling was undertaken 1 m from the floor.

  - The Bosch sensors were positioned at 1 m inside the chamber for 10 minutes during the smoldering phase, after which they were removed.

- Additional gas detection technologies:

  - A VESDA (Very Early Smoke Detection Apparatus) system was integrated with the chamber, which operated concurrently with the E-nose to measure and record relevant data.

During the large-scale testing phase, the BME688 sensor was not used for collecting new training data. Its primary purpose was to verify the predictions made by algorithms created from earlier small-scale experiments using similar samples. Figure 3.4 and 3.5 shows the experimental setup at the FAATC.

Figure 3.4 FAATC mockup inside and outside view
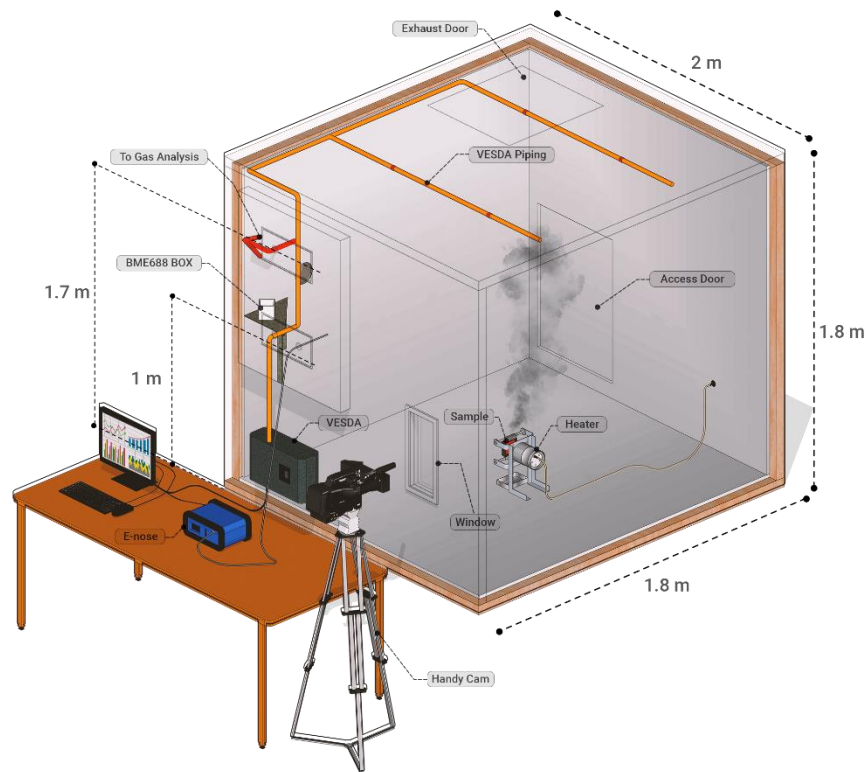
Figure 3.5 FAATC Test-Setup

In a subsequent testing phase, experiments were conducted in a specially designed chamber with a volume of 1.30 m^3 that could operate under reduced pressure conditions. This chamber's internal pressure was reduced to 10.9 psi during the smoldering phase of the experiments. Maintaining consistency with the earlier experiments, the heat flux was set at 25 kW/m^2 with a similar heater setup. Both the MSEM and Bosch sensors were actively employed during these tests. Figure 3.6 – shows the actual image of the pressure chamber.

Figure 3.6 Low-Pressure Vessel

3.3   Calculations and Algorithms

3.3.1   Light obscuration measurements

Light obscuration measurements were concurrently executed with the E-nose measurements during the small-scale tests at UMD. This was performed within the experiment chamber to provide supplementary measurements representing the smoke produced from the sample materials. Essentially, the light obscuration method gauges the reduction in light intensity caused by the particulate matter in a medium. A decrease in light signifies increased density or concentration of particles from the smoke. The calculations for this metric were based on equation 1, which provides a quantifiable measure of the amount of light obscured by the smoke particles.

$$\text{Obscuration (\%)} = \left(1 - \frac{I}{I_0}\right) \times 100 \qquad \text{Equation (1)}$$

- I_0 – Light intensity without any smoke present.
- I – Light intensity when the smoke is present.

3.3.2 MSEM Data Operations

The MSEM responses were analyzed using the proprietary software provided by Sensigent. The calculations were carried out according to the requirements of the study to get the best results. Tailored calculations were performed, optimizing the settings within the software's framework to derive the most informative and reliable outcomes.

In the subsections, various data scaling methodologies and normalization procedures used in machine learning and multivariate analysis are explored. These techniques are instrumental in optimizing the performance of various algorithms employed in data processing. The operation of dimensionality reduction methods such as Principal Component Analysis (PCA) and Canonical Discriminant Analysis (CDA), clustering algorithms like Soft Independent Modeling of Class Analogy (SIMCA), K-Nearest Neighbors (KNN), Support Vector Machines (SVM), and K-Means clustering (K-Means), are discussed in detail.

Signal-to-Noise Ratio Reduction

The raw data obtained from sensors often contains noise or unwanted signals, which can impede accurate analysis. Digital filtering techniques are employed to eliminate artifacts, including high and low-frequency noise, thereby enhancing the signal-to-noise ratio (S/N). In the post-processing phase of the study, a standardized processing approach was employed for sensor responses. This method, denoted as ΔR/R, characterizes the sensor's resistance response relative to a predetermined

baseline value, specifically, the resistance at the commencement of a given measurement. Mathematically, it's expressed as:

$$\text{Sensor Response} = \frac{R_{\max} - R_O}{R_O}$$

Equation (2)

- R_O - Initial resistance at the onset of the measurement.
- $R_{\max}$ - Peak resistance observed during the measurement

The Savitzky-Golay filter, a heavily used signal processing tool, enhances the signal-to-noise ratio in datasets without considerably distorting the inherent signal trends. This tool is the suggested and default option by the manufacturer. This filter operates by conducting a local polynomial regression on a specific subset of input data points, thus determining the smoothed value for each point. Mathematically, the smoothed value y_i' for a given data point y_i is calculated as:

$$y_i' = \sum_{j=-n}^{n} c_j y_{i+j}$$

Equation (3)

Where c_j are the convolution coefficients determined by the degree of the polynomial and the width of the window used for the regression, and n is half the width of the window. This method ensures that features like maxima, minima, and width of the distribution are preserved, making it particularly suitable for datasets with underlying trends that need noise reduction without compromising the signal's resolution.

Baseline Correction

Baseline correction is essential in multi-sensor measurements to ensure consistent data interpretation across sensors. Variations in baseline can arise from differences in sensor calibrations, drift, or environmental factors during the measurements. By adjusting for these

deviations, baseline correction enhances the comparability of data, ensuring that observed signals are attributed to measured events rather than instrumental inconsistencies.

The Advanced Minimum Maximum (*Adv Min Max*) algorithm, the default option from the Sensigent, is used in the analysis for baseline correction, which is important when analyzing data from a multisensory system to ensure accurate interpretation of the sensed environment. The algorithm processes each sample exposure in the sensor response file to compute ΔR within this framework. It achieves this by identifying the single maximum value, R_{max}, from the last three data points during the measurement. Concurrently, it estimates the baseline, R_{min}, by assessing the linear trend of the 10 points preceding the onset of the sample exposure. The baseline-corrected value, ΔR, is then computed using equation 4.
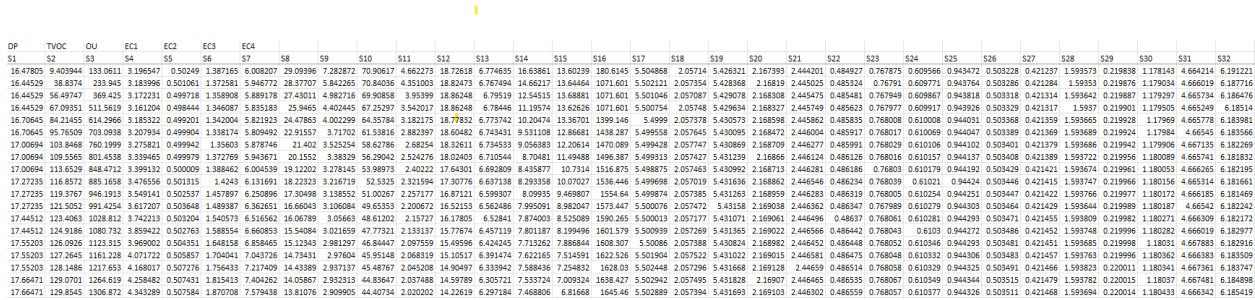
$$\Delta R = R_{max} - R_{min}$$ Equation (4)

Normalization and Scaling

In multi-sensor data analysis, normalization and scaling techniques are important to ensure consistent data range across sensors, facilitating more accurate comparative analyses. This uniformity in data presentation prevents any single sensor with larger magnitude responses from disproportionately influencing multi-sensor fusion outcomes. Furthermore, data on a consistent scale provides clearer insights for visualization and pattern recognition purposes.

Normalization

The time-varying sensor responses are arranged along the rows against their respective sensors in the column in the matrix representation used for sensor data analysis. Figure 3.7 Illustrate a sensor response from a CSV file.

Figure 3.7 Sensor responses from a CSV file

Norm1- Area normalization

"norm1" or L1 norm-based area normalization is a row-wise application on a dataset matrix. To elucidate, consider a matrix where each row represents the array of sensor responses for a singular signatures or exposure. By applying the "norm1" normalization row-wise, the responses from all sensors about a specific sample are scaled such that their cumulative absolute values amount to unity.

Mathematically, for a given row vector $r = [r_1, r_2, \ldots, r_n]$ in the matrix, the L1 normalization process can be formulated as:

$$r_{\text{norm}}[i] = \frac{r_i}{\sum_{j=1}^{n} |r_j|} \quad \text{for each } i = 1, 2, \ldots, n \qquad \text{Equation (5)}$$

Following this operation, the totality of the absolute values in each row converges to one. This ensures consistent scaling across varied samples and emphasizes the relative importance of each sensor's response.

Norm2 – Vector Normalization

The "norm2" or L2 norm-based vector normalization is another valuable approach in this context. Unlike the "norm1" method, which emphasizes the absolute cumulative response, the "norm2" technique focuses on the Euclidean length of the sensor response vector for a specific sample.

Considering our matrix, where each row represents an array of sensor responses for a single sample or exposure, the "norm2" normalization is applied row-wise. Let's take a row of sensor responses $r = [r_1, r_2, ..., r_n]$. Post the L2 normalization, the Euclidean length (or magnitude) of each transformed row vector will be unitary.

Mathematically, the L2 normalization can be described as:

$$r_{\mathbf{norm}}[i] = \frac{r_i}{\sqrt{\Sigma_{j=1}^{n} r_j^2}} \quad \text{for each } i = 1, 2, ..., n \qquad \text{Equation (5)}$$

After this operation, the length of the resultant vector from each row is standardized to one. By ensuring that each vector has a consistent length, the L2 norm-based normalization brings out the relative directionality and orientation of the sensor responses, which can be paramount for certain analytical operations and pattern recognition tasks in multisensory systems.

Another method, a "*none*" option, which refrains from applying any normalization to the sensor responses, is also explored as part of the study. This approach retains the original scale and magnitude of sensor outputs. While normalization techniques often aim to alleviate scale discrepancies between sensors, this is tried to study the raw, unaltered concentration-dependent response of the sensors. By opting for the "*none*" method, we were able to observe the direct and

true magnitude of the sensor's response to different sample exposures and their prediction dependency for the sensors.

Data Scaling: Mean Centering and Autoscaling

To focus on variability around the mean, mean centering is employed by subtracting the mean of each variable (32 sensor values). Mathematically, for a given data matrix X, the mean-centered matrix is $X_c = X - \bar{X}$, where $\bar{X}$ represents the mean of X.

Another data scaling method, autoscaling, is achieved by first mean centering the data and then dividing by the standard deviation of each variable. Hence, for a mean-centered matrix X_c the autoscaled matrix X_s is given by $X_s = \frac{X_c}{\sigma}$, where σ denotes the standard deviation of X_c. This ensures that each column (or variable) of the processed data possesses unit variance.

Both options are explored according to the cross-validation results for multiple data sets. Evaluating mean centering and autoscaling via cross-validation (CV) methods provides insights into which technique yields superior class differentiation and identification accuracy and is used as the first measure of choosing the right algorithm for the prediction.

Clustering Algorithms

Multivariate analysis algorithms are crucial in comprehensively analyzing datasets that encompass multiple variables simultaneously. Their primary function is to detect patterns and determine relationships within multidimensional data. Given the inherent complexity of many datasets, these algorithms become indispensable, offering capabilities such as dimensionality reduction, classification, clustering, and regression. These tools aid in simplifying data interpretation, ensuring that essential patterns and relationships are not overlooked, and enhancing predictive

modeling for the sensor measurements. Table 3.4 – provides information on the algorithms explored in this study.

Algorithms		Linearity	Supervision
PCA	Principal Components Analysis	Linear	Unsupervised
CDA	Canonical Discriminant Analysis	Linear	Supervised
SIMCA	Soft Independent Modeling of Class Analogies	Linear	Supervised
KNN	K-Nearest Neighbor	Nonlinear	Supervised
K-Means	K-Means Clustering	Nonlinear	Unsupervised
SVM	Support Vector Machine	Nonlinear	Supervised

Table 3.4 Various Classification Algorithms and Dimensionality Reduction techniques

Cross Validation and Prediction Probabilities

Cross-validation is an integral procedure to assess the robustness and validity of the algorithms. By doing the cross-validation operation, the software systematically omits a subset of samples from the training set, creating a temporary model using the remaining data according to the chosen scaling and classification algorithm. The samples initially set aside are then classified using this provisional model. For the CDA algorithm, this iterative process incorporates various counts of principal components (PCs), homing in on the optimal number that maximizes cross-validation accuracy (%CV). This metric, the %CV, represents the proportion of the omitted samples correctly classified using the best number of PCs. Upon finalizing the cross-validation, the system visualizes the results in Canonical (or "Mahalanobis") space, offering an intuitive representation of sample distributions and class separations.

In the Canonical Discriminant Analysis analysis, each predicted sample is assigned a Combined Probability (CProb). This metric serves as an indicator of the software's conviction regarding the accuracy of a particular classification. The CProb values, which range between 0 and 1, offer insights into the confidence level of the prediction, with values closer to 1 indicating higher confidence.

Subsequently, the CProb value for each sample gets translated into a rating based on a 5-star system, where five stars epitomize maximum confidence and 1 star represents minimum confidence in the classification. An associated metric called the MDist value (Mahalanobis distance) is calculated for each prediction. This value gauges the proximity of a given sample to the centroid of its assigned class within the training set, as represented in Mahalanobis space. Lower MDist values are more favorable, indicating that the sample is tightly clustered around its designated class and aligns well with its classification.

Utilizing a comprehensive CV process within the software framework, employing algorithms like K-Nearest Neighbors (KNN), K-Means Clustering (K-means), and Canonical Discriminant Analysis (CDA) with both data scaling methods, ensure the selection of the most robust combination for precise pattern recognition for a particular training set.

Principal Component Analysis (PCA)

Principal Component Analysis (PCA) is a fundamental data visualization and exploration technique used in multisensory data analysis. The inherent complexity of dealing with numerous sensor responses, often exceeding 32, necessitates the dimensionality reduction capability of PCA. This method effectively reduces the data's dimensionality from N sensor responses to more manageable M principal components. These components are visually structured: the first principal

component (PC1) encapsulates the most substantial variance in the dataset. Subsequent components, such as PC2 and PC3, are orthogonal to their predecessors and represent consecutively reduced variances. PCA is unsupervised, emphasizing that the algorithm does not rely on class labels to discern distinctions between classes. Instead, PCA depends entirely on the statistical variances within the dataset, offering an unbiased insight into the data structure.

Mathematically, the process begins by centering the data matrix X, resulting in a centered matrix $X_c = X - \bar{X}$, where $\bar{X}$ is the mean of X. Subsequently, the covariance matrix C of the centered data is computed as

$$C = \frac{1}{n-1} X_c^T X_c \qquad \text{Equation (5)}$$

with n denoting the number of observations. An eigen decomposition of C is then performed, leading to a matrix E of eigenvectors and a diagonal matrix Λ of eigenvalues, satisfying the relation $C\,E = E\,\Lambda$. These eigenvectors, or principal components, define directions in the original feature space that capture the maximum variance. The data can then be projected into a reduced space spanned by the first M principal components, yielding $Y = X_c E_M$.

Canonical Discriminant Analysis (CDA)

Canonical Discriminant Analysis (CDA) is another advanced multivariate technique predominantly employed when dealing with multisensory systems. Unlike PCA, which is unsupervised and based on capturing the most variance within a dataset, CDA is a supervised method requiring known class memberships for its operation. The ultimate objective of CDA is to maximize the distance between the means of different classes while minimizing the scatter or variance within each class. This facilitates enhanced separation and, thus, better discrimination between classes based on the sensor readings.

Given a dataset X with known class labels, the between-class scatter matrix S_B and the within-class scatter matrix S_W are computed. The goal of CDA is to find a transformation matrix W that will maximize the ratio of the determinant of the between-class scatter to the within-class scatter. Mathematically, this can be represented as:

$$W = \text{argmax}/\text{W} \frac{|W^T S_B W|}{|W^T S_W W|} \qquad \text{Equation (6)}$$

Once this transformation matrix is determined, the dataset can be projected into a new space wherein the classes are optimally separated. CDA's strength is its inherent focus on class separation, making it particularly effective for classification tasks in multisensory systems.

SIMCA Analysis

The Soft Independent Modeling of Class Analogy (SIMCA) technique is tailored for complex datasets commonly encountered in multisensory systems with multiple observations. Central to SIMCA's interpretive power is its utilization of Q versus T^2 plots, which serve as graphical representations to delineate typical observations from potential outliers. The T^2 statistic, colloquially termed as Hotelling's T^2, measures the extent to which an observation is projected within the subspace demarcated by the model's principal components. This is mathematically represented by:

$$T^2 = (x - \mu)^T P \Lambda^{-1} P^T (x - \mu) \qquad \text{Equation (7)}$$

Here, x is the mean-centered data point, μ symbolizes the dataset's mean, P denotes the matrix of principal component loadings, and Λ is a diagonal matrix comprising the eigenvalues. The Q statistic, often referred to as the squared prediction error (SPE), encapsulates the residual difference between actual data and the predictions rendered by the model. It is articulated as:

$$Q = e^T e \hspace{4cm} \text{Equation (8)}$$

Where e is the residual vector emerging from reconstructing x via its related principal components. Through the application of the Q versus T^2 plots, data analysts are equipped to swiftly reduce observations that align seamlessly with the constructed model from those that deviate.

KNN Algorithms

The K-Nearest Neighbor (KNN) classification algorithm, grounded in nonlinear cluster analysis, leverages spatial proximity to determine class assignments in supervised machine learning. In essence, for a given unclassified observation, KNN discerns 'k' nearest training samples to it, often using the Euclidean distance as the determining metric. The object of interest is then ascribed to the class most predominant among its neighbors. In practice, for k = 1, the classification is straightforward, as the object is unequivocally assigned to the class of its singular nearest neighbor. It's worth noting that the optimal value of 'k' is data-dependent: while larger 'k' values can mitigate the influence of noise on the classification, they might concurrently blur the class boundaries.

$$d(x, y) = \sqrt{\sum_{i=1}^{N}(x_i - y_i)^2} \hspace{3cm} \text{Equation (9)}$$

The Euclidean distance between two points x and y in an N-dimensional space is expressed as per the above equation.

K-Means Algorithms

The K-Means clustering algorithm is a partitioning method that segregates N observations into K distinct, non-overlapping clusters. The principal objective is to assign each observation to a cluster such that it belongs to the cluster with the nearest mean. The essence of K-Means lies in its simplicity: each observation is associated with the cluster whose centroid — the arithmetic mean

position of all the points in that cluster — is nearest to it. This proximity is commonly gauged using the Euclidean distance as a metric. The algorithm optimizes the placements of centroids to minimize the within-cluster sum of squares (variance), ensuring that the overall spread or scatter within each cluster is minimized. Iteratively, data points are assigned to the nearest centroid, and the centroid's position is recalibrated based on the points associated with it. Mathematically, the objective function J that K-Means seeks to minimize is:

$$J = \sum_{i=1}^{K} \sum_{x \in C_i} ||x - \mu_i||^2 \qquad \text{Equation (10)}$$

C_i represents the ith cluster, μ_i is the centroid of cluster C_i and x is a data point within cluster C_i. This two-step process is repeated until convergence is achieved, meaning centroids no longer change significantly. One inherent assumption of K-Means is that clusters are spherical and roughly of the same size, which directly arises from its reliance on variance as a measure of cluster scatter and the use of Euclidean distance.

Support Vector Machine (SVM) Algorithms

The Support Vector Machine (SVM) is a sophisticated supervised machine learning technique predominantly designed for binary classification, though it can also tackle multiclass challenges. Notably, SVM often outperforms linear discrimination algorithms like PCA and CDA, especially when dealing with intricate datasets that exhibit inherent non-linearity. At its core, SVM aims to identify the best hyperplane that distinctly divides the two classes. In simpler two-dimensional scenarios, this hyperplane manifests as a straight line, but in more complex multi-dimensional spaces, it evolves into a plane or even a more intricate hyper-surface. One of the distinct attributes of SVM is its adeptness at managing non-linear data by projecting it into a higher-dimensional space, a feat achieved through the "kernel trick". The data points lying nearest to this hyperplane,

known as "support vectors", essentially shape and define its optimal positioning. SVM's overarching goal is to amplify the distance, or margin, between the identified hyperplane and the closest data point from each class.

3.4   Bosch BME688 Measurements

The integrated Micro-Electro-Mechanical System (MEMS) heater in BME688 plays a critical role in the gas measurement. The heater profile in the BME688 refers to a predetermined sequence of temperature setpoints and durations, which dictates how the heater is cycled on and off and at what temperatures during the gas measurement process. The heater profile (HP) is a significant parameter because different gases may have varying optimal temperatures for detection. In this study, multiple heater profiles were employed within the development kit with different measuring cycle times. Each heater cycle was assigned to two sets of sensors to ensure comprehensive data collection. Also, all the sensors were operated under the RDC-1-0 (Repeating Duty Cycle) continuous duty cycle (No sleeping cycle). Each duty cycle is an iteration of a heater profile. The duration of a scanning cycle is equal to the duration of the heater cycle, and the duration of each Sleeping Cycle is always equal to the duration of a Scanning Cycle. This operational mode led to an average power consumption of 12mA for each full cycle.

In this study, multiple heater profiles were employed, notably HP-301, HP-354, HP-411, and HP-501 and operated with a RDC-1-0 continuous duty cycle. Figure 3.8 shows the heater profiles and the temperatures.
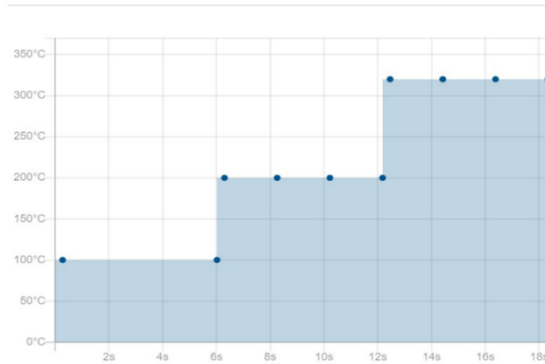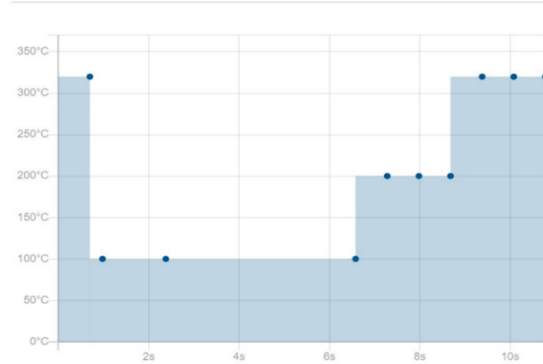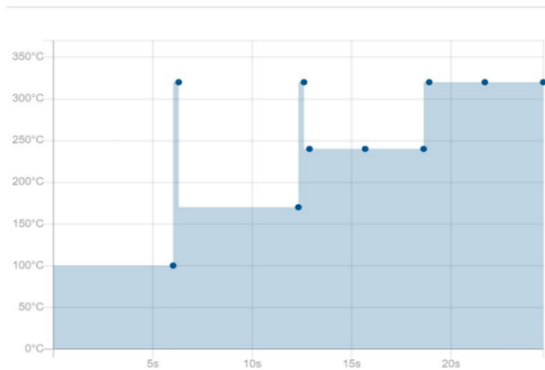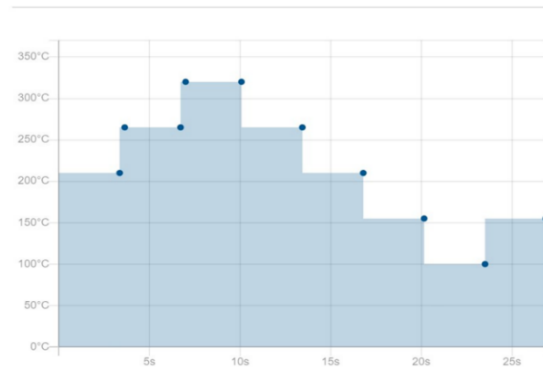
Figure 3.8 Heater profiles and temperatures

The capabilities of the BME AI Studio are used to train the neural network, focusing solely on the Gas Data Channel for our data inputs. The dataset was judiciously partitioned, allocating 70% for training and reserving 30% for validation to gauge the model's performance on unseen data. To optimize the sensor's neural network, the Adam optimizer was employed. This optimizer uses its adaptive moment estimation properties, effectively blending the strengths of the well-regarded optimization techniques: AdaGrad and RMSprop. Such a combination fosters rapid convergence and skillful navigation of the weight space. To promote computational efficacy and occasionally hasten convergence, training data was divided into batches, each consisting of 32 examples. It underwent an exhaustive training routine spanning up to 2048 epochs to ensure the model's

adaptability and precision further. Emphasizing the significance of an epoch, it embodies a full forward and backward traversal of the entire dataset through the neural network.

3.5   Samples Used in the Study

For this study, a diverse set of samples were collected with specific areas of interest: avionics, aircraft cables, and potential nuisance sources in the aircraft cockpit. These divisions were pivotal in comprehensively understanding and analyzing each subset's distinct properties and characteristics. Table 3.5 itemizes the samples under each category that were used during the small-scale testing.

PRINTED CIRCUIT BOARDS (PCB)		
Identification Number	Sample original Serial Number	Specification
A1	200-09058-000	KX 155A Audio Board
A2	634-2698-002	ATR Connector
A3	105-02307-00	Transducer
A4	153-018105-02	Inverter Board
A5	634-3517-005	Chassis Adapter
A6	440-00059-03 NEC, NL10276BC20-04	GDU Display
A7	-	Multi-Function Displays
A8	105-02133-00	Navigation System
A9	FR-4 1/8"	Fire Retardant Garolite
WIRE SAMPLES		
B1	10/0.1 Equip Standard VESDA Testing Cable	PVC Wire
B2	M81381 / 12-20	Aromatic Polyimide insulation
B3	M22759/ 34-16-9	ETFE (Tefzel coating)
B4	BMS13-60-19	PTFE
B5	55A0811-20-9	ETFE
NUISANCE SOURCES		
WO	Hardwood	-
BR	Bread	-

Table 3.5 Samples used in the small-scale experiment

A Major part of the study emphasized the examination of Printed Circuit Boards (PCBs) given their presence on the flight deck of an aircraft. A representative selection of these PCB samples is depicted in Figure 3.9. To ensure uniformity and manageability, each of these samples were cut into a 7.6 X 7.6 square centimeter size, which was subjected to thermal impact using the heater. The subsequent results chapter will comprehensively present an in-depth visual documentation, along with discussions on the impacts of heating and other significant observations.
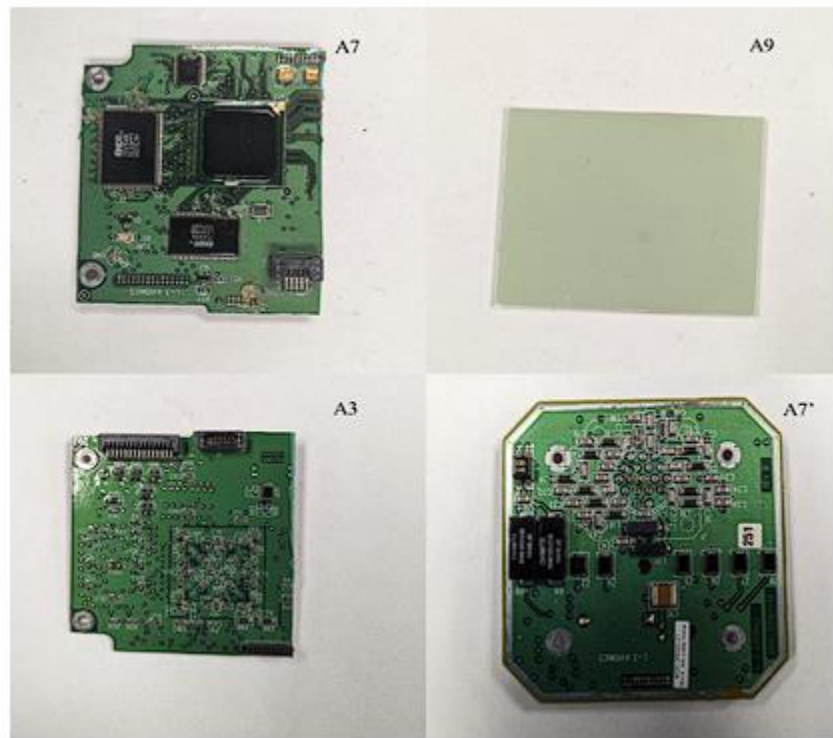
Figure 3.9 Various PCB samples used in the small-scale experiment

In-flight occurrences of vapors generated from recirculation fans have been frequently reported. Such phenomena can be attributed to various factors, including overheated windings, short circuits, or possible abrasions of the fan blades with external materials. This critical area was explored with investigations into printed circuit boards and wire insulations during the testing sessions at the

FAA. Notably, two recirculation fans were procured through industry donations, which were subsequently subjected to failure testing, with all relevant readings recorded with E-nose and BME688 sensors. A comprehensive list of samples employed for the large-scale testing at the FAA technical center is detailed in Table 3.6, and Figure 3.10 provides images of the recirculation fans used in the study.

Sr No	Sample original Serial Number	Assigned Name	Type
PRINTED CIRCUIT BOARDS			
1	105-01134-00 Ver 3	AE	Unknown
2	105-02109-00 Ver 1	AC	Unknown
3	S4151-009060720020	AF	Unknown
4	FR – 1/8"	FR	Fire Retardant Garolite
WIRE SAMPLES			
5	M81381 / 12-20	AP	Aromatic Polyimide Insulation
6	M22759/ 34-16-9	ETFE	ETFE (Tefzel Coating)
7	BMS13-60-19	PTFE	PTFE
8	M5086/1-22-9	PVC	PVC
FAN SAMPLES			
9	645405-1	HF	Recirculation Fan
10	4100941D	BF	Fan Mixed Flow
NUISANCE SOURCES			
11	SKYDROL 500 B-4	HY	Hydraulic Oil
12	MOBIL JET OIL II	JO	Aviation Jet Oil

Table 3.6 Samples used in the large-scale testing

Figure 3.10 Recirculation Fans collected from the industry for testing

3.6 Experimental Protocols

The various samples utilized in the study were systematically categorized into four distinct groups:

Printed Circuit Boards (PCBs), Aircraft Cables, Recirculation Fans, and Nuisance Sources.

Each category followed a protocol to create signature readings, ensuring repeatability and

precision:

1. **Printed Circuit Boards and Nuisance Sources**

To capture the gaseous signatures from the samples, the MSEM 160 and Bosch BME688 were powered on, allowing a warm-up duration of 30 minutes, ensuring sensor stabilization. Following this stabilization period, the photodiode was activated, allowing us to obtain baseline light obscuration readings under ambient, smoke-free conditions. The heater was then engaged, and a 15-minute interim was observed to ensure a consistent thermal profile. The E-nose was subjected to two sequential measurement cycles to further understand and capture pre-test data. With these preliminary readings in place, the sample was placed near the heater, receiving direct heat exposure for a 10-minute duration. Upon completion of this heating period, the heater was turned off, and the MSEM initiated a series of five measurement cycles. Bosch BME688 sensor was run simultaneously to capture gas sensor profiles. For predictive analytics objectives, this entire procedure was repeated using either the same sample or a closely related variant to produce the signatures.

2. **Aircraft Cables**

To study the off-gassing vapors emanating from cable insulations, a test transformer made by Xtralis was utilized, designed explicitly for wire burn tests. This transformer had a conversion capability of 110 V to 6.3 V, with a 20 A output rating. For the tests, wire samples were prepared to a length of 70 cm, with both ends stripped up to 15mm. These designed samples were then connected to the transformer terminals. The transformer was remotely activated for 60 seconds, inducing the wires to produce smoke due to the applied voltage.

This resultant smoke was subsequently subjected to analysis using the electronic nose (E-nose). A minimum of five measurement cycles were conducted to ensure robustness in the readings. Each of these cycles was composed of three stages: a pre-purge stage (60 seconds), an active

measurement stage (60 seconds), and a post-purge stage (60 seconds). Alongside the E-nose measurements, light obscuration readings were simultaneously captured prior and during the measurement to provide a comprehensive overview of the smoke characteristics along with the cable integrity.

3. Large Scale Experiments

In the comprehensive experiments conducted at the FAATC, the heater was set to a heat flux of 25 kW/m^2, positioned at the central juncture of an 180 x 200 cm^2 mock space. A 91 cm ultra chemical-resistant Tygon tubing was used for sampling for the E-nose at 1m above the floor level. Concurrently, gas analysis sampling for carbon monoxide (CO) and carbon dioxide (CO$_2$) and Oxygen (O$_2$) concentrations was placed at an elevated height of 170 cm from the floor. The Bosch BME688 sensor was kept at the 1m level from the floor, ensuring parity in sampling heights. A video recording was operational to ensure comprehensive visual documentation of the procedure when the samples were placed near the heater. After the heating duration of 10 minutes, the sample was manually retracted, and E-nose readings were recorded for pattern recognition up to five measurement cycles.

A sophisticated VESDA monitoring system, integrated with four sampling ports on the ceiling of the box, was configured to predetermined light obscuration thresholds: 0.0760 %/m instigating a preliminary Alarm, 0.1141 %/m initiating Action, 0.1902 %/m triggering Alarm 1, and 0.2281 %/m actuating Alarm 2 as per the manufacturers calculation for the space. Prior to the smoldering experiments, the VESDA system was already operational. In parallel, the E-nose maintained a continuous monitoring mode throughout the combustion phase. The inclusion of the BME688 sensor was imperative to gauge the predictive efficacy of algorithms precursory developed during the experiments at UMD.

For the study on the cable insulations, samples measuring a length of 90 cm were prepared, with both ends stripped to up to 15mm. Electrical voltage was then applied to these samples for 60 seconds using the Xtralis wire burner. During this period, the light obscuration measurements were completed along with the E-nose measurements.

For the fan experiments, an external aircraft power source delivering 400 Hz and 115 V was utilized to energize the fans. Given the specific interest in capturing signatures resulting from fan overload or prolonged usage, a specialized method was devised. An external resistance to the fan operations was introduced to simulate the effects of overload. This was accomplished through a custom-built mount, onto which the fans were affixed; a steel plate welded explicitly for this purpose from the top provided resistance by obstructing the impeller's motion. With the impeller effectively getting locked against the steel plate during the operation, the motor winding was driven to its limits, emitting gaseous signatures indicative of stress and potential failure. Figure 3.11 depicts the setup used for fan failures.

Figure 3.11 Experimental Setup for Fan Failure at the FAATC

4 RESULTS AND DISCUSSION

4.1 Gas Analysis Using E-Nose Capabilities in Small-Scale Testing

4.1.1 Aviation Cables

While the aviation cables utilized in the study encompassed various wire gauges, making a direct comparison of gas concentrations is inappropriate, a qualitative assessment of the gases emanating from these materials was conducted using the E-nose capabilities. In this approach, Total Volatile Organic Compounds (TVOC) in mg/m³, alongside concentrations of Alcohol (Alc), Ammonia (NH_3), Formaldehyde (CH_2O), and Ethylene (C_2H_4) in parts per million (ppm), were collected. Additionally, odor measurements were captured in Odor Units per cubic meter (OU/m³), utilizing the advanced sensing capabilities of the E-nose. This comprehensive data collection underscores the commitment to a thorough and nuanced understanding of the gas profiles generated from diverse aviation cable types, contributing significantly to the field's knowledge base, and enhancing safety and material selection protocols in aviation contexts.

The average gas concentrations are derived from the sensor values during the E-nose measurement cycle, which is succeeded by a pre-scale measurement phase during which outside gases are not sampled. The maximum value represents the peak response recorded across the various measurement cycles for all the samples tested from similar classes. Table 4.1 – shows the various gas measurements by the E-nose.

SAMPLE	B1 (PVC)		B5 (ETFE)		B3 (ETFE - Tefzel Coating)		B4 (PTFE)		B2 (Aromatic Polyimide)	
	Average	Maximum	Average	Maximum	Average	Maximum	Average	Maximum	Average	Maximum
TVOC $[mg/m^3]$	13	18	15	24	13	19	10	18	6	14
Alc [ppm]	0	1	2	4	2	4	2	2	5	10
NH_3 [ppm]	0	0	0	0	0	0	0	0	0	0
CH_2O [ppm]	0	1	1	2	1	2	1	2	1	6
C_2H_4 [ppm]	1	2	3	7	3	7	4	5	3	9
ODOR $[OU/m^3]$	236	518	331	636	439	667	399	427	486	671

Table 4.1 Gas Analysis for Different Aviation Cables
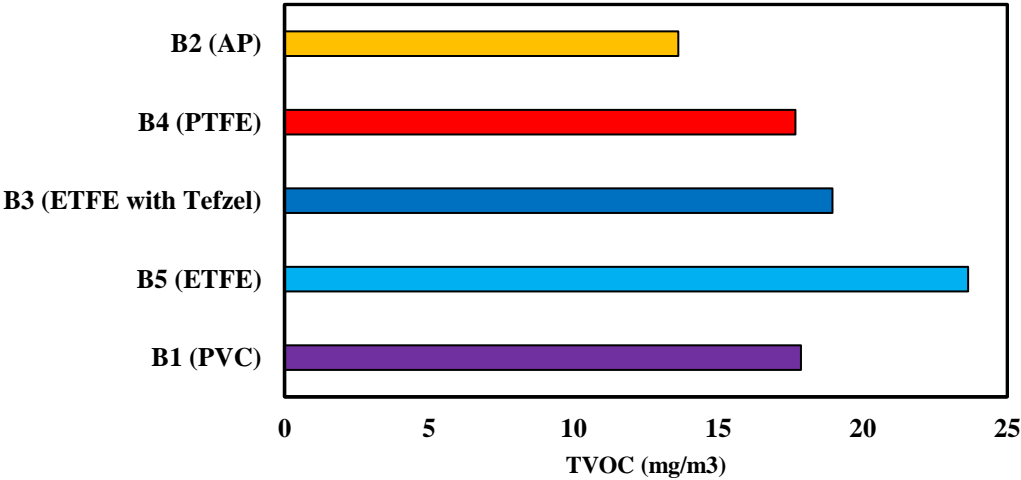
Figure 4.1 Maximum TVOC Values Recorded for the aviation cables

Focusing exclusively on these specific gases may not substantially aid the detection and identification processes. The Alc, NH_3, C_2H_4, and CH_2O evolved from the cable samples exhibit characteristics akin to noise, offering limited utility for effective detection. This insight

underscores the imperative for a more holistic and diversified early detection and identification approach.

4.1.2   Printed Circuit Boards and Other Materials

The printed circuit boards, sourced from diverse avionics, encompassed a broad array of electronic components. The potential inclusion of Total Volatile Organic Compounds (TVOC) as an auxiliary early detection metric emerged as a viable strategy to bolster detection endeavors. The analysis reported an average TVOC level of 150 mg/m³, signifying its discernible presence compared to other gases. Conversely, the other four gases under scrutiny registered levels similar to background noise, thereby underscoring their limited utility for effective detection in this context.

SAMPLE	A1		A2		A3		A4		A5		A6		A7		A8		A9	
	Avg	Max	Avg	Max	Avg	Max	Avg	Max	Avg	Max	Avg	Max	Avg	Max	Avg	Max	Avg	Max
TVOC [mg/m^3]	131	194	97	133	60	77	51	75	178	207	80	121	178	248	125	161	76	100
Alc [ppm]	2	6	3	11	5	9	2	4	6	12	3	7	2	6	2	4	2	6
NH$_3$ [ppm]	0	0	0	0	0	0	0	0	0	0	0	0	0	0	0	0	0	0
CH$_2$O [ppm]	1	2	1	4	3	6	1	1	3	6	2	3	1	3	1	2	1	4
C$_2$H$_4$ [ppm]	3	7	2	9	7	15	3	5	6	11	5	9	2	8	3	9	5	12
ODOR [OU/m^3]	1411	1876	867	1504	651	940	540	920	1566	1867	1227	1872	1121	1666	1003	1886	735	1225

Table 4.2 Gas Analysis for Printed Circuit Board Samples
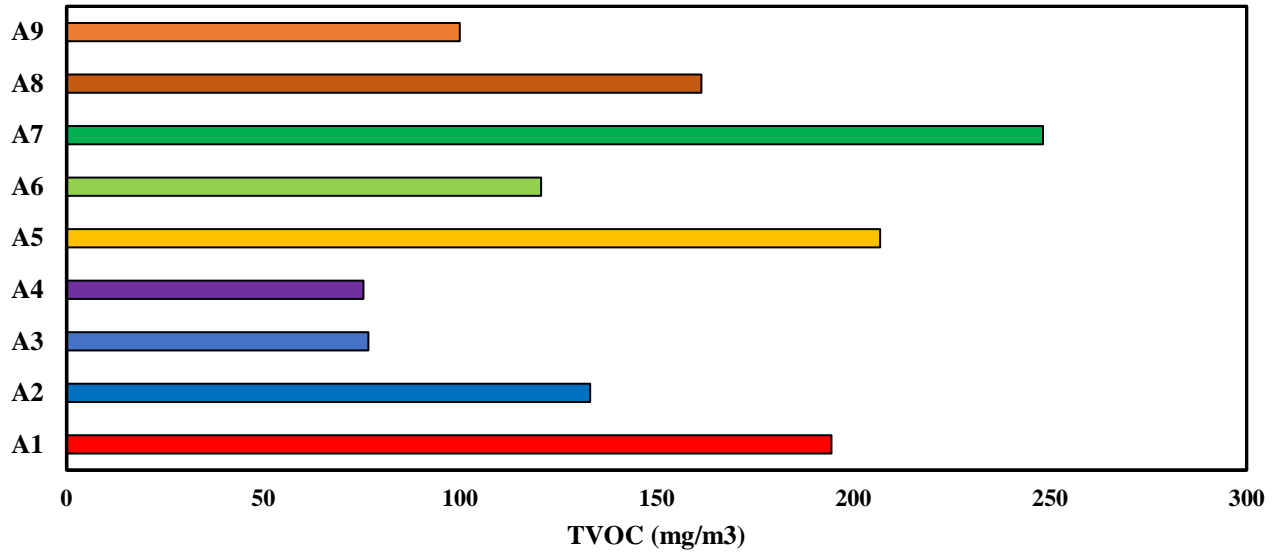
Figure 4.2 Maximum TVOC Levels Recorded for Printed Circuit Boards

The analysis of other nuisance sources revealed distinct gas emission profiles. The bread sample exhibited an average TVOC level of 169 mg/m³, while Hardwood registered a higher average of 264 mg/m³. Additionally, the Alcohol (Alc) levels in these samples were markedly elevated compared to the printed circuit boards (PCBs), with readings of 39 for bread and 99 for Hardwood, respectively

SAMPLE	Bread		Hardwood	
	Average	Maximum	Average	Maximum
TVOC [mg/m^3]	133	169	205	264
Alc [ppm]	21	39	38	99
NH$_3$ [ppm]	0	0	0	0
CH$_2$O [ppm]	3	7	2	6
C$_2$H$_4$ [ppm]	1	2	1	4
ODOR [OU/m^3]	1611	1881	1162	1886

Table 4.3 Gas Analysis for Other Materials

4.2 Light Obscuration Measurements in Small-Scale Testing

In the present scenario, although the aircrew can detect smoke in occupied areas, there is often a significant time lag between the onset of an FSF event that produces burning odors and the observation of visible smoke. The occurrence of these burning odors, in the absence of continuous smoke, may lead to confusion among the crew members due to the lack of consistent and reliable indication from the smoke detection and alarm systems. This gap in detection presents a challenge for ensuring prompt and appropriate responses to potential fire events on board.

The amount of smoke generated from the multi-stranded, single cable exhibited distinct characteristics for different samples. Specifically, the B2 and B4 samples generated considerably less smoke than their B1, B3, and B5 counterparts. A visual assessment further revealed differences in the resilience of various insulations under these conditions. By the 60-second mark, PVC and PTFE insulations had sustained significant damage, while the ETFE insulation demonstrated considerable durability, preserving its structure significantly. While undergoing a color

transformation to a deep black, the Aromatic Polyimide insulation commendably retained its structural integrity, effectively concealing the metal wires within.

In the tests involving Printed Circuit Boards and nuisance sources, the chamber became heavily saturated with thick smoke, leading to a complete, or 100%, obscuration.

Sample	Percentage Obscuration
B2 (Aromatic Polyimide)	14.62
B4 (PTFE)	12.85
B1 (PVC)	21.70
B5 (ETFE)	46.86
B3 (ETFE with Tefzel)	55.16

Table 4.4 Light Obscuration measurements for aviation cables

4.3   Gas Analysis Using E-Nose Capabilities in Large-Scale Testing

4.3.1   Aviation Cables

The gas sensor measurements provide valuable insights into the gases released during smoldering, mirroring trends observed in small-scale experiments. To ensure accuracy of the values, values were adjusted for baseline measurements. This baseline was established by recording sensor values under ambient conditions for five minutes prior to the commencement of each experiment. Notably, the TVOC levels from the newly analyzed PVC cables, which were not part of the initial

small-scale experiments, registered significantly higher than their counterparts. Similarly, the odor measurements followed a comparable trend.

SAMPLE	AP		ETFE		PTFE		PVC	
	Average	Maximum	Average	Maximum	Average	Maximum	Average	Maximum
TVOC [mg/m^3]	6	12	4	20	3	9	12	29
Alc [ppm]	2	4	2	5	1	2	1	3
NH$_3$ [ppm]	0	0	0	0	0	0	0	0
CH$_2$O [ppm]	1	3	1	4	1	2	0	1
C$_2$H$_4$ [ppm]	5	10	3	13	3	6	1	4
ODOR [OU/m^3]	222	460	150	558	167	249	318	887

Table 4.5 Gas Analysis for Aviation Cables in Large-scale testing

4.3.2   Printed Circuit Boards and Other Sources

While the measurements for Alcohol (Alc), Ammonia (NH$_3$), Formaldehyde (CH$_2$O), and Ethylene (C$_2$H$_4$) registered minimal values, the Total Volatile Organic Compounds (TVOC) levels from the Printed Circuit Boards (PCBs) were observed to be higher than those from external contaminant sources such as Hydraulic Oil (HY) and Jet Oil (JO). Moreover, the TVOC levels from the fans were also considerably elevated compared to the PCBs and other samples. This observation necessitates acknowledging the distinct setup used for the fans, wherein they were intentionally made to fail. This different setup could influence the TVOC levels, contributing to the observed measurement disparity.

SAMPLE	AC		AE		AF		FR		BF		HWF		HY		JO	
	Avg	Max	Avg	Max	Avg	Max	Avg	Max	Avg	Max	Avg	Max	Avg	Max	Avg	Max
TVOC $[mg/m^3]$	27	41	28	35	10	13	20	28	88	122	50	63	1	2	10	15
Alc [ppm]	0	1	1	2	0	1	1	2	13	25	5	9	0	0	2	4
NH_3 [ppm]	0	0	0	0	0	0	0	0	0	0	0	0	0	0	0	0
CH_2O [ppm]	0	0	0	1	0	0	0	1	7	12	4	6	0	0	1	2
C_2H_4 [ppm]	0	1	1	3	1	2	1	3	2	2	9	15	0	0	3	7
ODOR $[OU/m^3]$	84	223	204	366	147	405	269	543	1547	1887	1218	1873	16	24	55	112

Table 4.6 Gas Analysis for PCBs and Other materials in Large-scale testing
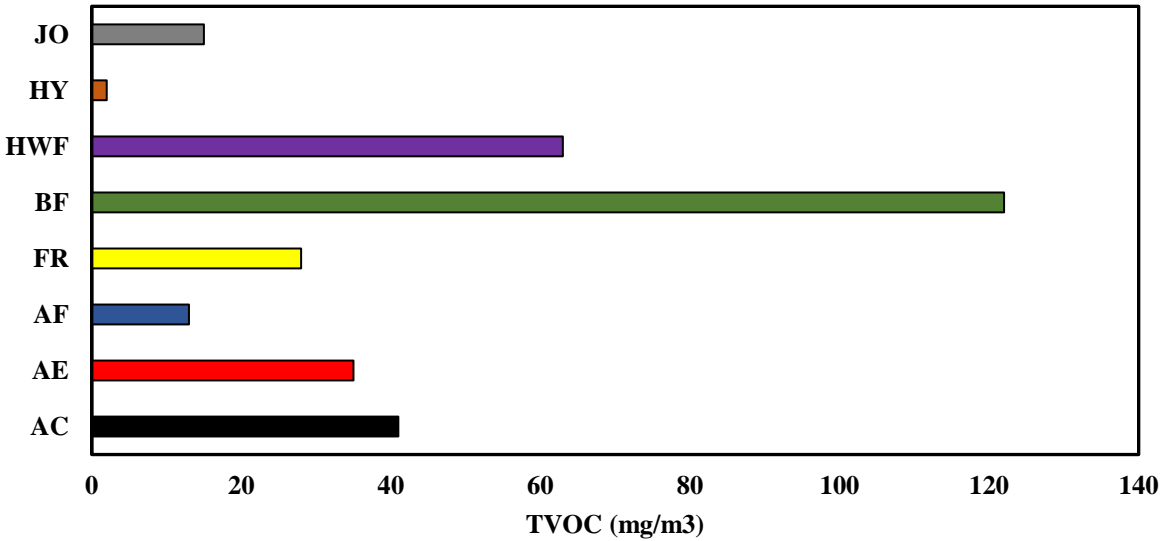
Figure 4.3 Maximum TVOC Levels Recorded for Printed Circuit Boards and Other Sources in Large-scale testing

4.4   Light Obscuration Measurements using VESDA

The VESDA VEP was employed in the FAATC Mockup tests to analyze the response time among various systems in the study. Additionally, the maximum light obscuration measurements recorded by the VEP offered valuable insights into the smoke levels associated with different materials. Within the VESDA VEP, obscuration was quantified as a percentage obscuration per meter (% obscuration/m), with a threshold of 32.8 % per meter for the laser chamber.

The average maximum measurements mirrored the trends observed in small-scale testing. Specifically, the PTFE and Aromatic Polyimide samples generated less smoke than the PVC and ETFE cables. Despite producing a significant amount of smoke, the ETFE cable preserved its mechanical integrity. In contrast, the PVC cable exhibited charring and fragmentation. The Aromatic Polyimide (AP) cables showcased superior integrity compared to the PTFE cables, with

82

less insulation damage observed. Detailed average peak responses for the cables are presented in

Table 4.7.

Sample	Obscuration (%/m)	Sustained Structural Integrity
AP	7.15 %/m	High
PVC	32.80 %/m	Low
PTFE	7.08 %/m	Medium
ETFE	32.80 %/m	High

Table 4.7 Light Obscuration measurements from VESDA

All the Printed Circuit Boards hit the threshold value of 32.8 during all the measurements, and the

Jet oil and Hydraulic oil samples registered an average measurement of 23.95 %/m.
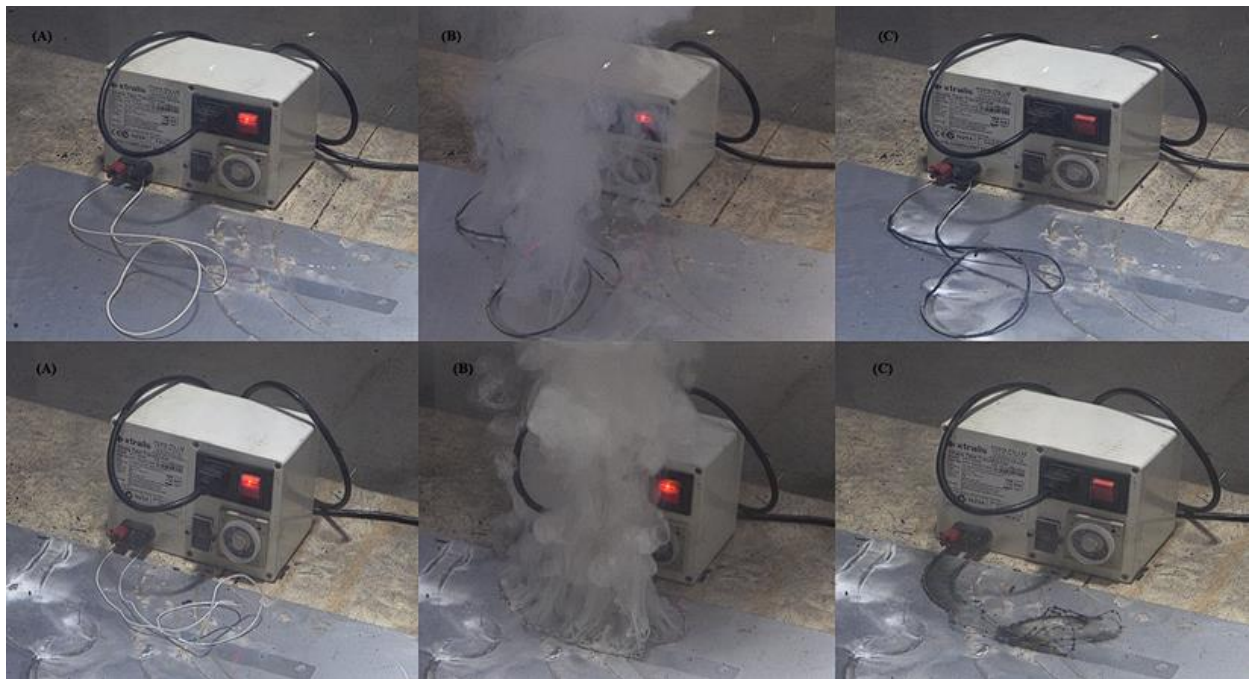
Figure 4.4 ETFE (TOP) (A) At the point of first visible smoke, (B) 20 seconds from the first smoke and (C) At the end of 60 seconds, PVC (Bottom) (A) At the point of first visible smoke, (B) 20 seconds from the first smoke and (C) At the end of 60 seconds
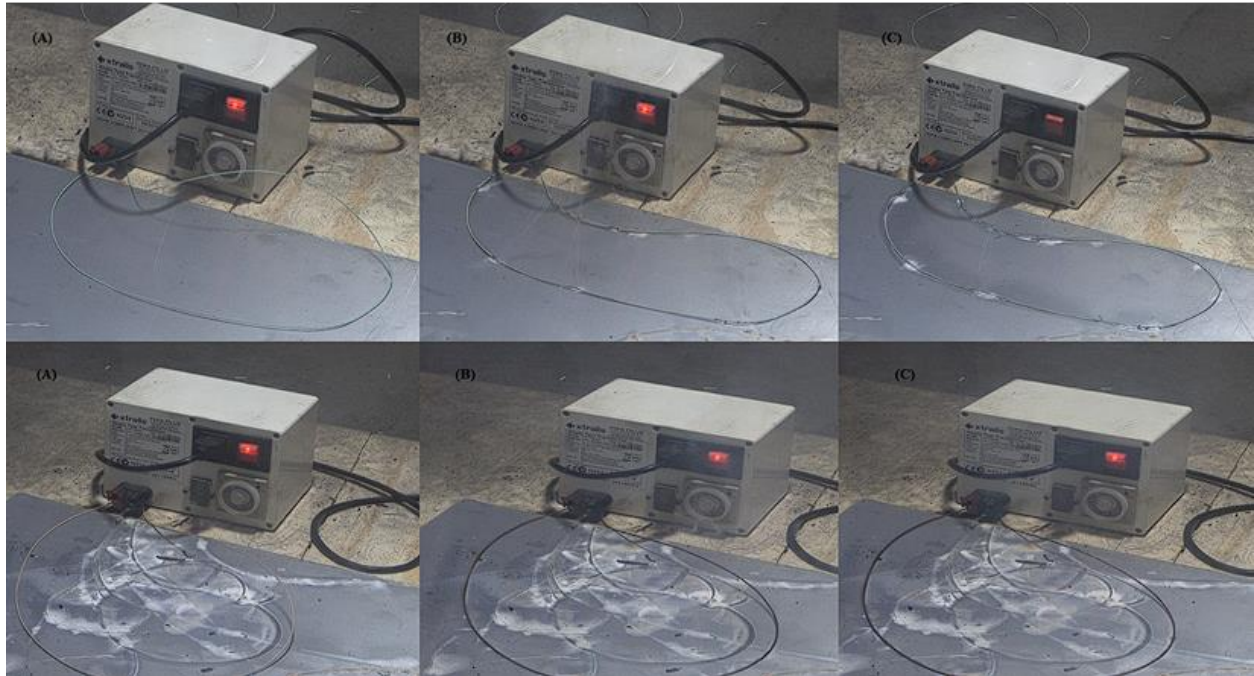
Figure 4.5 PTFE (TOP) (A) At the point of first visible smoke, (B) 20 seconds from the first smoke and (C) At the end of 60 seconds, AP (Bottom) (A) At the point of first visible smoke, (B) 20 seconds from the first smoke and (C) At the end of 60 seconds

4.5 Comparison between Visual, VESDA and E-nose detection

The FR boards subjected to testing exhibited the first visible signs of smoke after three minutes of thermal stress, followed by uninterrupted smoke production. The E-nose's TVOC responses aligned with this, showing an initial drift from the baseline measurement around the 200-second mark and continuously registering higher levels, thereafter, as depicted in Figure 4.6. The odor sensor exhibited a delayed response compared to the TVOC sensors, with a noticeable drift occurring at 260 seconds, as illustrated in Figure 4.7.

The VESDA system exhibited a rapid response in detecting the smoke, noting alterations to the baseline measurement starting at 180 seconds from the placement of the sample. For the FR-6 and FR-7 samples, the Fire-1 alarm was activated at 27 and 44 seconds, respectively. This was closely followed by the Fire-2 Alarm, which sounded at 30 and 46 seconds for the FR-6 and FR-7 samples,

respectively. The brief interval between these alarms is noteworthy, especially considering the volume of smoke produced during this phase. The system reached a 32.8 %/m threshold in a mere 74 seconds from the initial detection, underscoring its precision and reliability in monitoring evolving conditions. This prompt detection is illustrated in Figure 4.8.
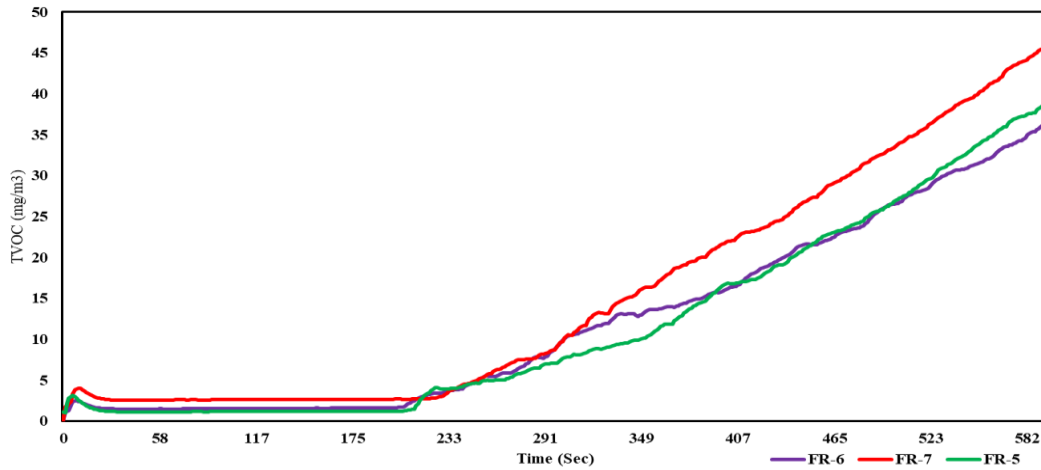
Figure 4.6 TVOC levels measured by the E-nose.
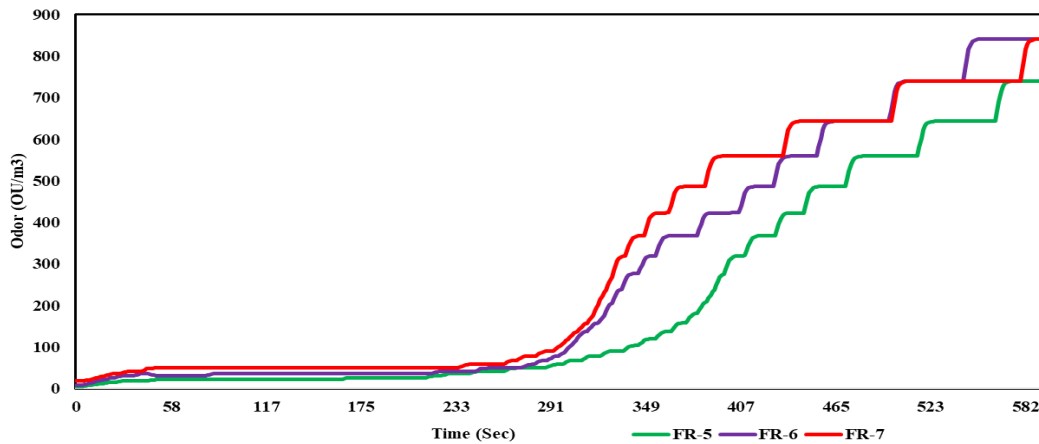
Figure 4.7 Odor measurements by the E-nose
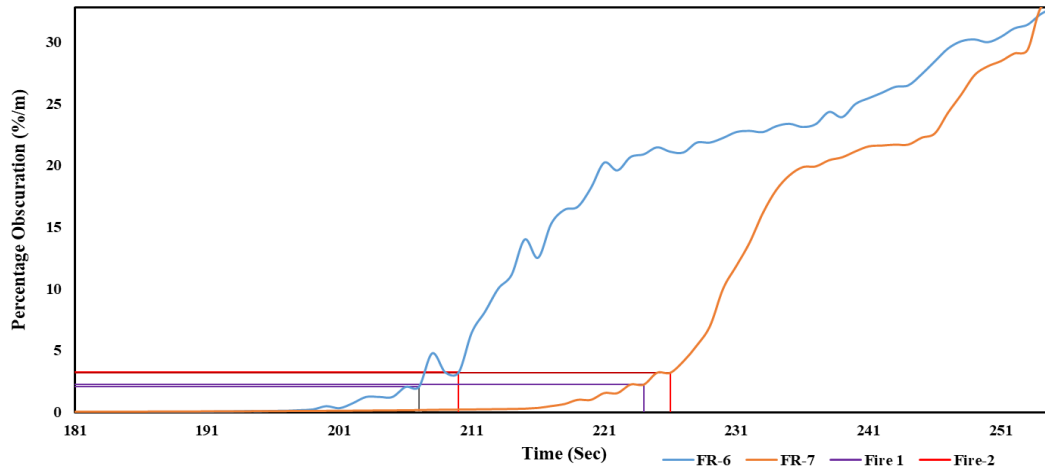
Figure 4.8 VESDA Smoke detection for two FR samples
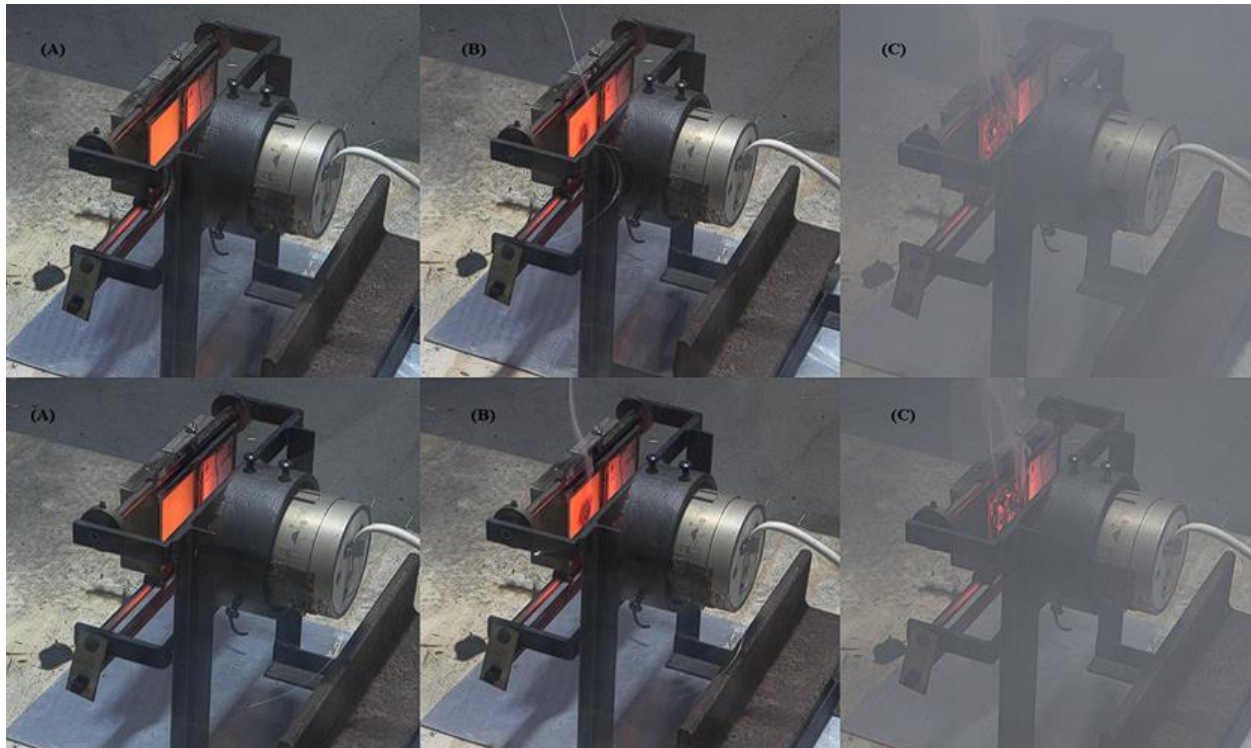
Figure 4.9 (TOP) FR-6 at (A) Time of placement of the sample (B) 3 minutes into the testing (B) 6 minutes into the testing

4.6   Gas Analysis for Large-scale Testing

In the mockup chamber at the FAATC, a comprehensive gas analysis focusing on CO, CO_2, and O_2 concentrations was conducted. CO and CO_2 measurements were consistently found within the background levels throughout the testing phase without any remarkable change. Specifically, CO concentrations fluctuated between 0.012% and 0.014% vol, and the O_2 concentrations remained stable around the ambient level of 21.6% vol. The CO_2 levels temporarily doubled before reverting to their initial values, reaching a maximum average threshold at 0.10% vol. During the initial stages of producing dense smoke, there was a noticeable increase in CO_2 levels. However, since these levels returned to normal throughout all experiments, this study did not investigate this phenomenon in more detail.

However, these levels are still within the noise threshold compared to a flaming fire condition. These observations indicate that relying solely on CO, O_2 consumption, and CO_2 measurements for detecting smoldering events, particularly in the context of PCB samples from avionics, might yield unreliable results, and alternative detection methodologies could be integrated to enhance accuracy. Figure 4.10 shows the changes recorded in the gas analysis for an FR board sample.
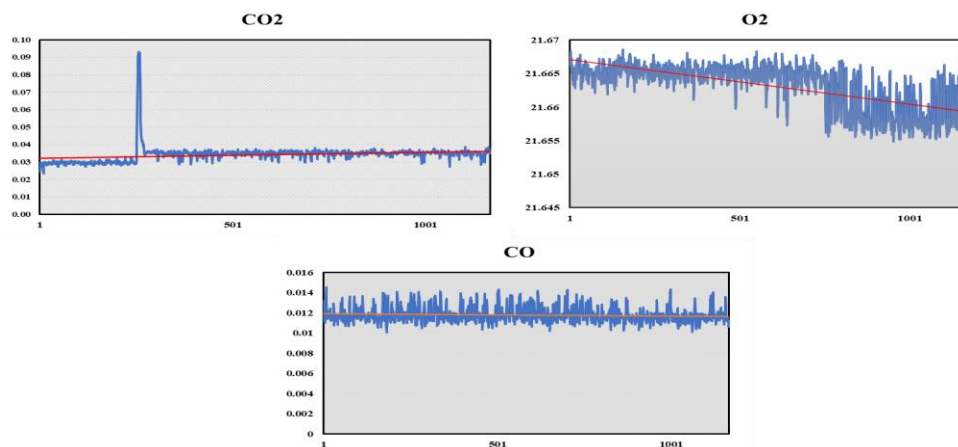
Figure 4.10 CO2, O2, and CO measurements recorded for an FR board sample

4.7 Explorative Multivariate Analysis of the Aviation Cables during Small-Scale-Testing

In this part, data acquisition was conducted using an electronic nose (E-nose) apparatus, followed by uniform post-processing protocols to ensure consistency across the datasets. Utilizing the Sensigent Proprietary software suite, multivariate analyses were performed. The software facilitated cross-validation with a predetermined training and validation data partition, which served to yield a cross-validation confidence metric. This metric estimates the likelihood of accurate prediction on subsequent production data. For the algorithms developed with the Bosch BME sensor suite, the dataset was bifurcated into a 70-30 split, with 70% utilized for training and the remaining 30% for validation purposes.

The aggregated data set, referred to as the 'Training set,' was employed for both the development and validation of the algorithms' predictive models. After this phase, an independent 'Prediction set,' comprised of production data derived from identical or similar sources, was utilized to assess the algorithms' predictive proficiency. The production data was entirely separate from the training and validation sets to ensure an unbiased model performance evaluation in each methodology. The cross-validation approach was not limited to a single model assessment but was extended to compare various machine learning models. This comparative analysis aimed to identify the model with the highest predictive accuracy potential, thereby suggesting the most reliable model for practical application in predicting outcomes with unseen production data.

Various aircraft cables, each distinguished by their unique insulation attributes, were tested for the prediction capabilities of E-nose through multivariate analysis. Four types of these cables were used at this stage of the study. B1 (PVC), B2 (Aromatic Polyimide), B4 (PTFE) and B5 (ETFE). Initially, five samples of each cable variant were subjected to the thermal impact setup, with each

sample undergoing five distinct measurement cycles. An additional three specimen for each cable type were then evaluated to analyze the prediction reliability of the E-nose responses and algorithms, with 2 predictive cycle measurement for each type.

Ni et al. (2008) adopted the Principal Component Analysis (PCA) and K-Nearest Neighbors (KNN) for their study. Other algorithms like, Support Vector Machines (SVM), K-Means clustering, Canonical Discriminant Analysis (CDA), and Soft Independent Modeling of Class Analogies (SIMCA) were explored in this study.

All the sensor responses were processed into the same scale by $\Delta R/R$. All four specimens were analyzed under two distinct data-centering techniques: Mean Centering and Autoscaling, along with area (Norm1) and vector (Norm2) normalization and without normalizing the data. By comparing the non-normalized data with its normalized counterpart, the goal is to interpret the underlying influences of concentration on sensor readings and its subsequent affect on predictive accuracy.

The sensor responses from the five samples were averaged to prepare a training set for the samples named 'Training Set-1'. Upon executing cross-validation of the training set for these cable insulation samples, the KNN model, in conjunction with the Mean-centering technique for Norm1, showed a correction probability of 70%. While the MSEM does not incorporate the SVM algorithm in its cross-validation options, the SVM independently showcased a correct rate of 96.3%. On evaluating the classification performance of various algorithms using Autoscale under Norm1, K-Means clustering classified all the samples, achieving 100% accuracy. Meanwhile, other models, including KNN, CDA, SVM, and SIMCA, demonstrated commendable performance with an accuracy of 91.6%, as one of the 12 samples was misclassified. Table 4.8 shows the correct performances of various algorithms with the samples.

	KNN	K-Means	CDA	SVM	SIMCA
B1 (PVC)	6/6	6/6	6/6	6/6	6/6
B2 (Aromatic Polyimide)	6/6	6/6	6/6	6/6	6/6
B4 (PTFE)	4/6	6/6	4/6	4/6	4/6
B5 (ETFE)	6/6	6/6	6/6	6/6	6/6

Table 4.8 Multivariate analysis of the cables using Norm1, Auto-scaling

From the analysis of various combinations of data-scaling and normalization techniques, the distinction between Norm1 and Norm2 methods appeared to have minimal influence on various multivariate algorithms' predictions. Notably, the classification accuracies consistently surpassed those predicted through the cross-validation operation. For subsequent samples, primary reliance was on the mean-centering and Autoscaling approach, complemented by cross-validation results. The similarity in experimental setups and samples must have resulted in akin signatures and raw sensor responses even when the data is not normalized, which seemingly did not deter the prediction performance. Other combinations of mean-centering and two data-scaling approaches have been studied but showed less accuracy than Norm1 with Autoscaling. Figure 4.11 shows the PCA plot under different data-scaling and normalization methods for training set-1.
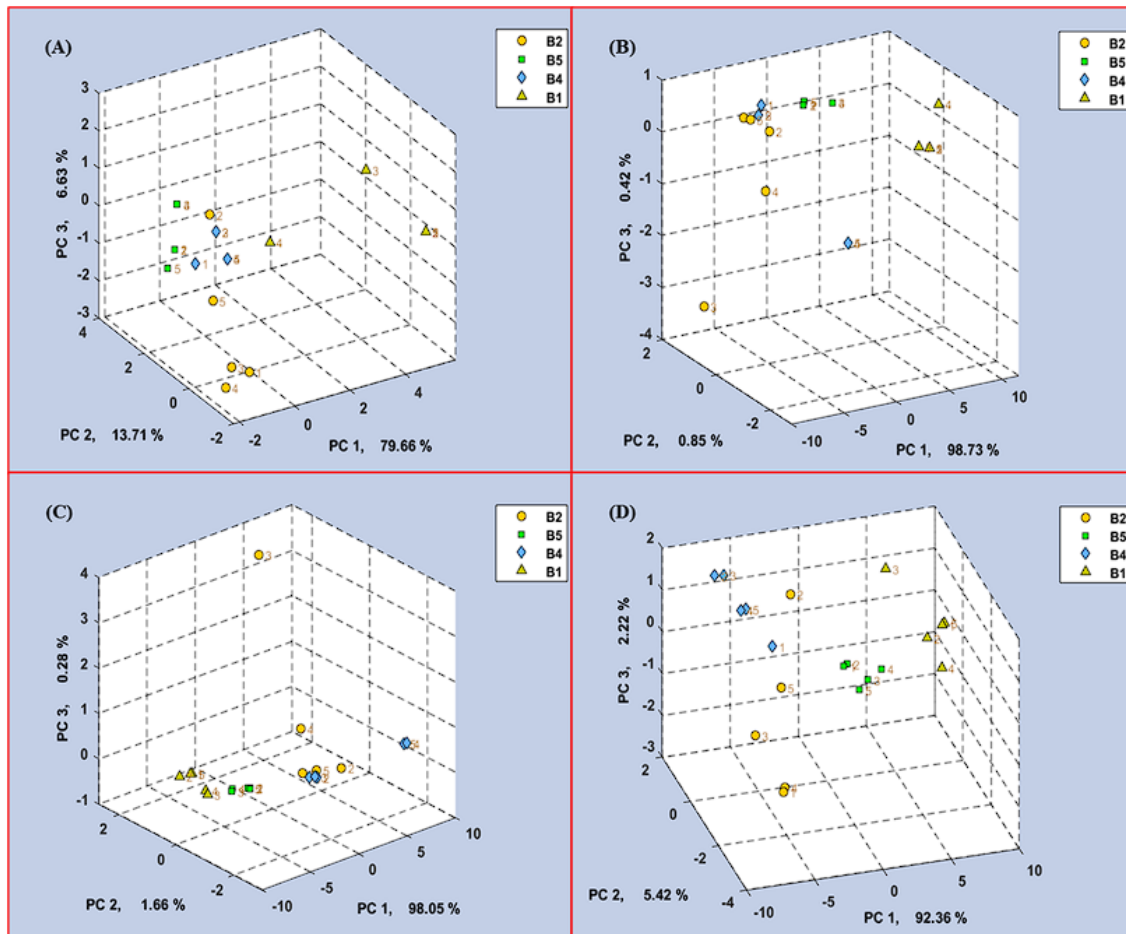
Figure 4.11 The CDA plot for Training Set-1. Figure (A) utilizes norm1 with Mean-centering, (B) employs norm1 with Autoscale, (C) applies no normalization but uses Autoscale, and (D) showcases results with no normalization paired with Mean-centering

K-means Goodness Value
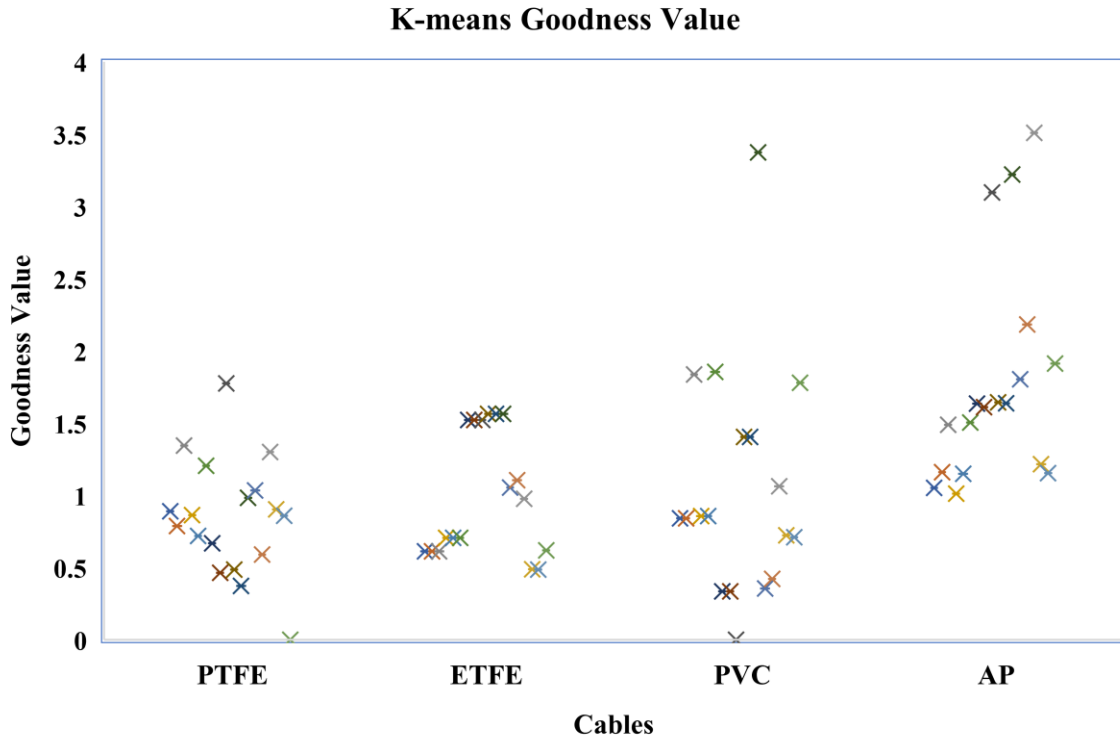
Figure 4.12 K-Means goodness value for samples with Training Set -1

CDA MDistance Values
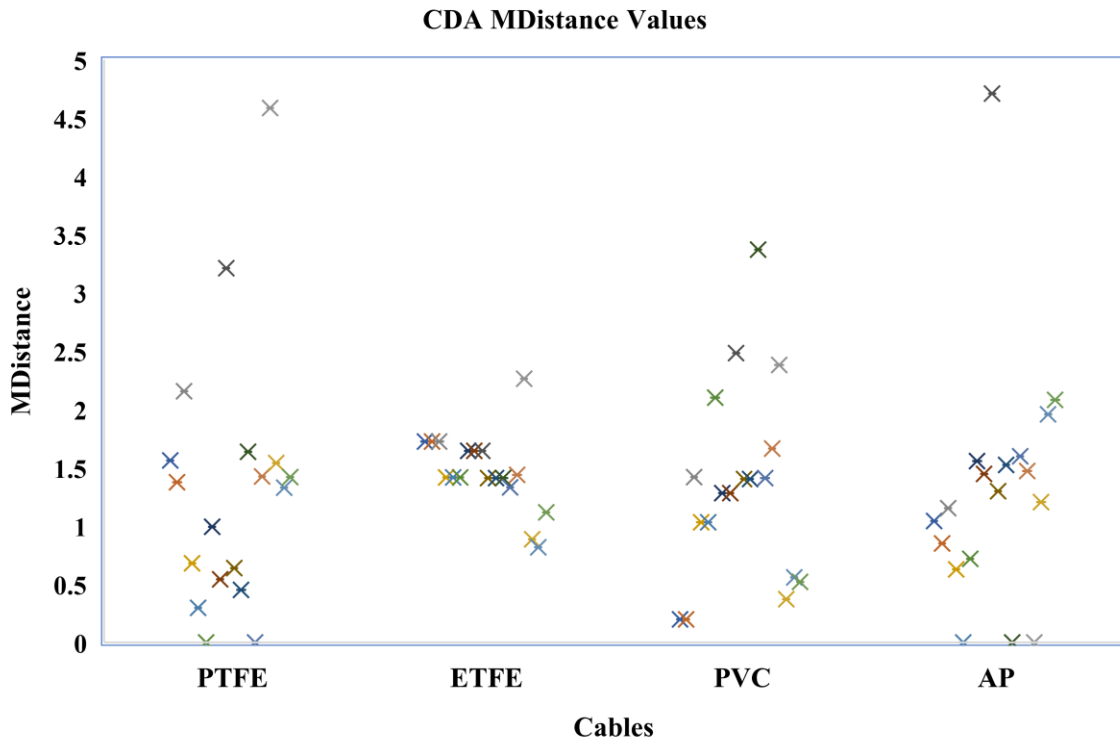
Figure 4.13 CDA Algorithm M-Distance Values for Various cable insulations

92

Figure 4.12 and 4.13 shows the Goodness Value (Gvalue) and Mahalanobis Distance (MDisatnce) value for various samples with K-Means and CDA algorithms. In applying the K-Means algorithm for the samples, the "Goodness Value" (Gvalue) is introduced as a metric reflecting the confidence level of the algorithm regarding its classification predictions. A lower Gvalue is indicative of better classification confidence. Notably, a Gvalue hovering around 1 is perceived as optimal, while any value less than 4 suggests that the classification into the respective class is reliable. However, for illustration purposes any misclassifications were adjusted to a Gvalue of 0. All the sample's Gvalue were found to be near one, indicative of a confident classification within the training set.

For the CDA (Canonical Discriminant Analysis) assessment, another crucial parameter, termed the "Mahalanobis Distance" (MDistance), was employed. This parameter quantifies the proximity of the predicted sample to its respective training class within the Mahalanobis space. Similar to the Gvalue, for representation any misclassifications in this approach adjusted to a MDistance of zero. Notably, the distance values for most cable samples across various data scaling methodologies predominantly resided around the benchmark value 1.

4.8   Utilizing a Singular Training Set for Classification Algorithms

Fujinaka et al. (2008) achieved an accuracy of 98.3% using one single training set for their samples from each fire source using a K-Means algorithm. Considering the earlier method for the cables with 'Training set-1', where the training set was developed using multiple data from a set of 5 experiments on each sample. As shown in Figure 4.11, the samples are scattered in the canonical space when evaluations were conducted using an averaged value. But this second approach of the study used data from one experiment to create the training set, and the data from the further experiments were used for prediction analysis.

The created training set, 'Training set-2', achieved a correction prediction rate of 75% for Norm1, 85% for Norm2, and 95% for no-normalization with Autoscale, through cross-validation. The SVM produced the highest correction rate of 96.3% for Auto-scale. Further, as per the cross-validation, either auto-scaling or mean-centering data scaling methods were employed.

With Auto-scale and Norm1 normalization, it was observed that the CDA and SIMCA algorithms stood out, flawlessly predicting all the samples across the four insulation types with an accuracy of 100%. Meanwhile, the K-means algorithm followed closely with a 96.4% accuracy. The SVM displayed a respectable performance, accurately classifying 92.2% of the samples and the KNN algorithm showed an accuracy of 85.5%. Table 4.9 shows the performance of different algorithms.

	KNN	K-Means	CDA	SVM	SIMCA
B1 (PVC)	14/14	14/14	14/14	14/14	14/14
B2 (Aromatic Polyimide)	10/14	14/14	14/14	10/14	14/14
B4 (PTFE)	12/14	14/14	14/14	14/14	14/14
B5 (ETFE)	12/14	12/14	14/14	14/14	14/14

Table 4.9 Multivariate Analysis for Training Set-2 using Norm1, Autoscaling
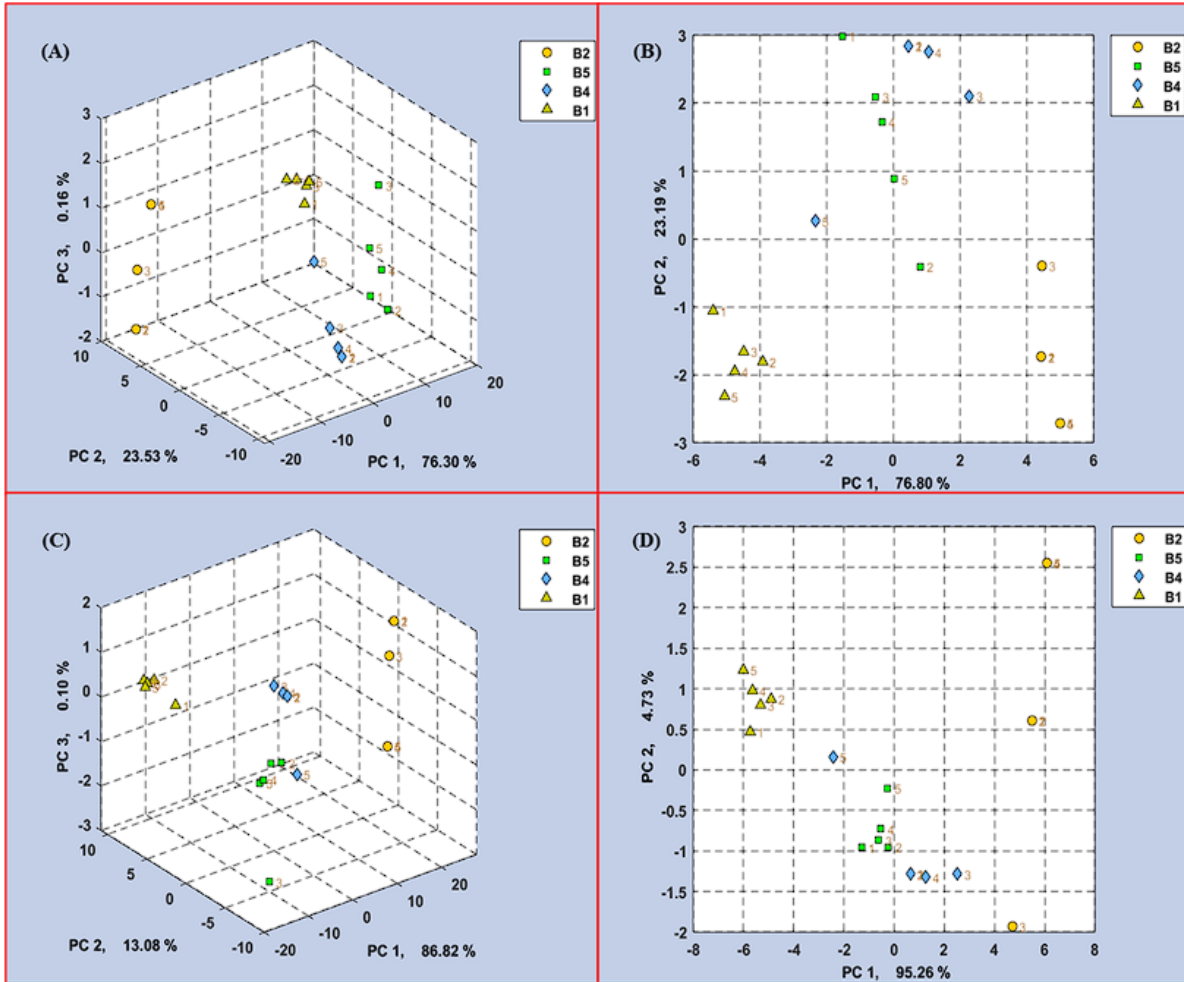
Figure 4.14 CDA Plot for four distinct cable types with Training Set-2. Figure (A) utilizes norm1 with Auto-scale, (B) employs norm1 with mean centering (C) applies norm2 with Auto-scale, and (D) showcases results with no normalization paired with Auto-scale

In contrast to the first method, which utilized averaged data from multiple experiments to construct the training set, the decision to draw datasets from a singular experiment led to a more pronounced variance or separation in sensor responses and good separation in the PCA plot, as shown in figure 4.14, culminating in improved prediction outcomes. Also, the Auto-scale results are grouped more closely than the mean-centering results for this approach.

An increase in the number of samples or training classes seems to instigate a certain ambiguity during data processing, likely because of minimal variance between the datasets. To counteract this challenge, the training set was limited to encompassing an identical sample pertinent to a particular experiment and its associated specimens.

4.9   Simplified Sensor Array Configurations with Cable Insulations

While every sensor in the E-nose plays a pivotal role in fulfilling its multifaceted functionalities, it becomes evident that employing all the sensors for pattern identification in smoke signatures introduces excessive noise, impeding the algorithm's identification efficacy. Moreover, a streamlined sensor array simplifies manufacturing processes and streamlines data management, enhancing operational efficiency. Similar observations regarding the use of multiple sensors were noted by Ni et al. (2008) in their respective study.

MSEM proprietary metric, the Important Index Weighting (IIW) algorithm, within the CDAnalysis was used to address this challenge. This algorithm assigns differential weights to sensors, with precedence given to those demonstrating a superior ability to distinguish between samples based on the training set data. Subsequently, sensor responses were filtered in accordance with their discriminating weightage, enabling a more refined and efficient pattern identification.

In 'Training set – 2', the Important Index Weighting (IIW) pinpointed 19 sensors with an index value surpassing 1. Subsequent cross-validation with these 19 sensors instead of the 32 sensors highlighted a 95% probability across Norm1, Norm2, and the No-normalization approach. Remarkably, both KNN and K-Means, previously registering accuracies of 85.5% and 96.4%, respectively, now exhibited an accuracy rate of 100%.

SAMPLE	KNN	K-Means
B1 (PVC)	14/14	14/14
B2 (Aromatic Polyimide)	14/14	14/14
B4 (PTFE)	14/14	14/14
B5 (ETFE)	14/14	14/14

Table 4.10 Multivariate Analysis for Training Set-2 using Norm1, Autoscaling under simplified Sensor Array Approach

The streamlined sensor array design suggests that not all sensors are crucial for discrimination analysis for the signature detection purposes, with the necessity contingent upon the data variance. This is further investigated with PCB and Nuisance Source samples.

4.10 Classification Algorithms with PCB for small-scale Testing

The study utilized printed circuit boards (PCBs) sourced from various avionic equipment, including Navigation Displays, Infotainment displays, and cockpit control modules. A significant challenge encountered was obtaining multiple, consistent samples for analysis. These samples contained diverse electronic components such as microcontrollers, transmitters, capacitors, and resistors.

The first training set, 'T1', consisted of PCB samples A1, A2, A3, and A5. Predictive analyses were conducted on these same samples, subjecting them to a burn duration of an additional 10 minutes to collect data for 5 prediction cycles. Cross-validation of the training set, T1 yielded a 95% accuracy rate, irrespective of whether normalization methods were applied. Remarkably, this accuracy surged to 100% when the IIW was employed, and eight sensors with an index value below one was excluded. Every algorithm identified the sample set with a 100% accuracy rate, attributed to the pronounced separation between the samples, as shown in Figure 4.15.

	KNN	K-Means	CDA	SVM	SIMCA
A1	5/5	5/5	5/5	5/5	5/5
A2	5/5	5/5	5/5	5/5	5/5
A3	5/5	5/5	5/5	5/5	5/5
A4	5/5	5/5	5/5	5/5	5/5

Table 4.11 Multivariate Analysis for T1 using Norm1, Autoscaling with all sensor values

	KNN	K-Means	CDA	SVM	SIMCA
A1	5/5	5/5	5/5	5/5	5/5
A2	5/5	5/5	5/5	5/5	5/5
A3	5/5	5/5	5/5	5/5	5/5
A4	5/5	5/5	5/5	5/5	5/5

Table 4.12 Multivariate Analysis for T1 using Norm2, Autoscaling after omitting 8 sensors with IIW less than 1
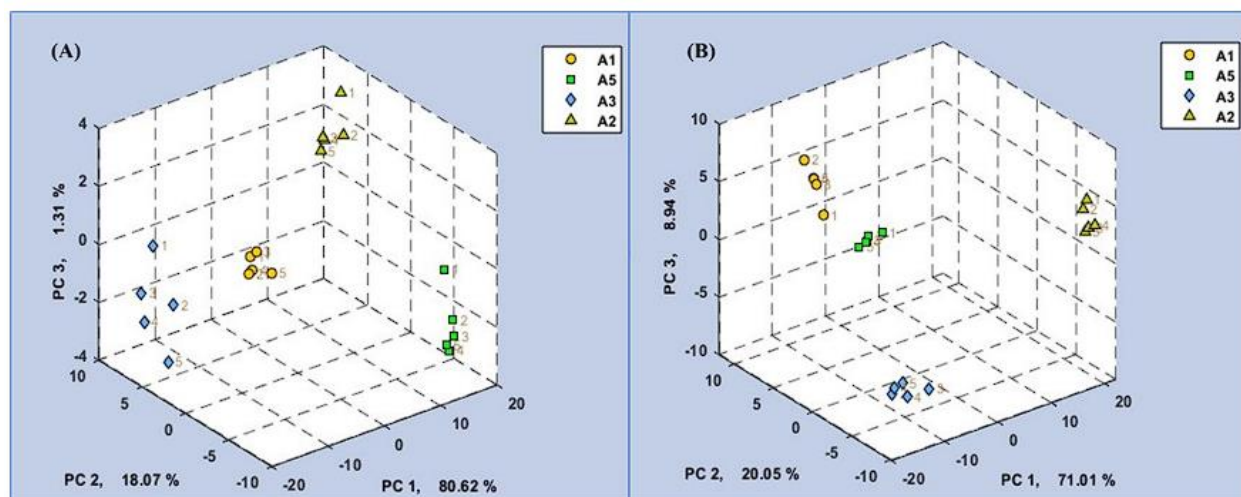
Figure 4.15 (A) T1 CDA Plot for 'Norm1' and 'Autoscale' using all 32 sensors. (B) 'Norm2 Autoscale' CDA representation, omitting eight sensors with an IIW below 1

Another training set, labeled as 'T2', was established using samples A4, A6, A7, A8, and A9, which were then subjected to predictive analysis. Cross-validation yielded a 76% accuracy rate for both normalization techniques and an improved 84% accuracy without normalization. This outcome with higher probability with no-normalization, can be attributed to the signature similarities among the samples. All tested algorithms accurately identified the samples from the prediction set. When ten sensors with an IIW value below one was excluded, cross-validation accuracy raised to 96%. This enhancement is illustrated in Figure 4.16, where the exclusion of sensors with lower weightage led to a more distinct PCA score plot for T2.

	KNN	K-Means	CDA	SVM	SIMCA
A4	5/5	5/5	5/5	5/5	5/5
A6	5/5	5/5	5/5	5/5	5/5
A7	5/5	5/5	5/5	5/5	5/5
A8	5/5	5/5	5/5	5/5	5/5
A9	5/5	5/5	5/5	5/5	5/5

Table 4.13 Multivariate Analysis for T2 using Norm1, Autoscaling with all the sensor values
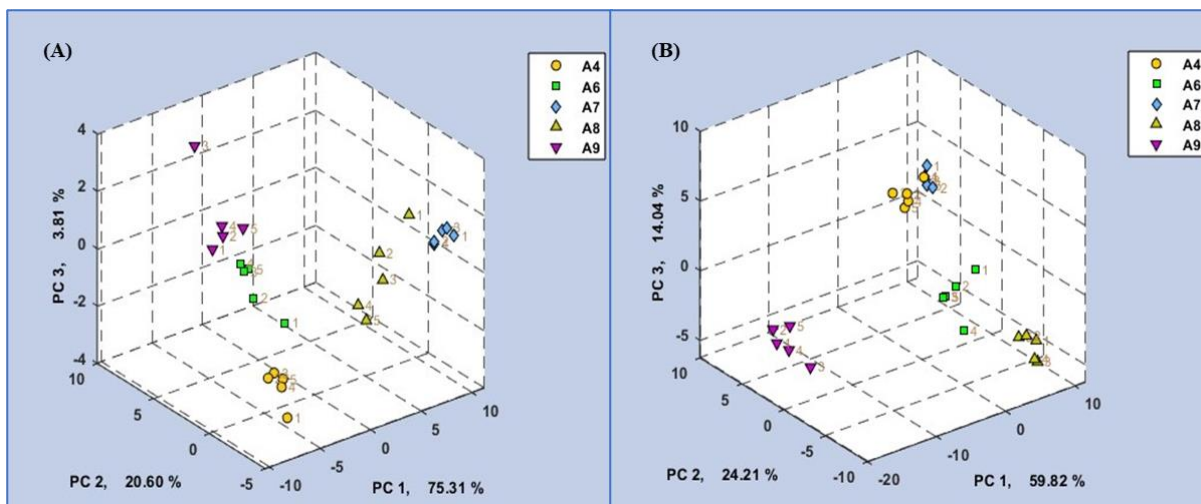
Figure 4.16 T2 (A) CDA Plot with 'Autoscale' using all 32 sensors. (B) CDA plot, after excluding 10 sensors with an IIW below 1

The signatures emanating from fire events can exhibit significant dynamism. Given the heightened sensitivity of E-nose systems to minimal sample alterations, accurate repeated prediction of these signatures poses a substantial challenge. This sensitivity may inadvertently introduce unwarranted noise, further complicating the prediction landscape. The adoption of a streamlined sensor array by exclusively employing sensors that contribute meaningfully to the prediction of fire-related signatures enhances the precision and reliability of fire detection and identification functions. This strategic approach mitigates the impact of unwanted noise, bolstering the E-nose system's efficacy in timely and accurate fire signature detection and classification.

4.11 Analysis of Prediction Repeatability for Different Electronic Components

Prediction data derived from a specific avionic circuit board, but containing different electronic components were evaluated for prediction using training set 'T1', these boards were cut into 7.62 X 7.62 cm samples and tested under the same setup. While these samples originated from the same PCB, they contained multiple distinct electronic components. Upon subjecting them to predictive analysis, the CDAnalysis could not match the samples to the training set, labeling them as "unidentifiable", across all algorithms. Also, some of the Mdistance values were exceeding 100. A plausible explanation for this inconsistency is that even though the signatures come from the same equipment, different samples might house many varied components, resulting in different signatures. Figure 4.17 illustrates the disparity in the PCA plot for additional samples from A3 and A2 tested against the other A3 and A2 samples in the training set-1.
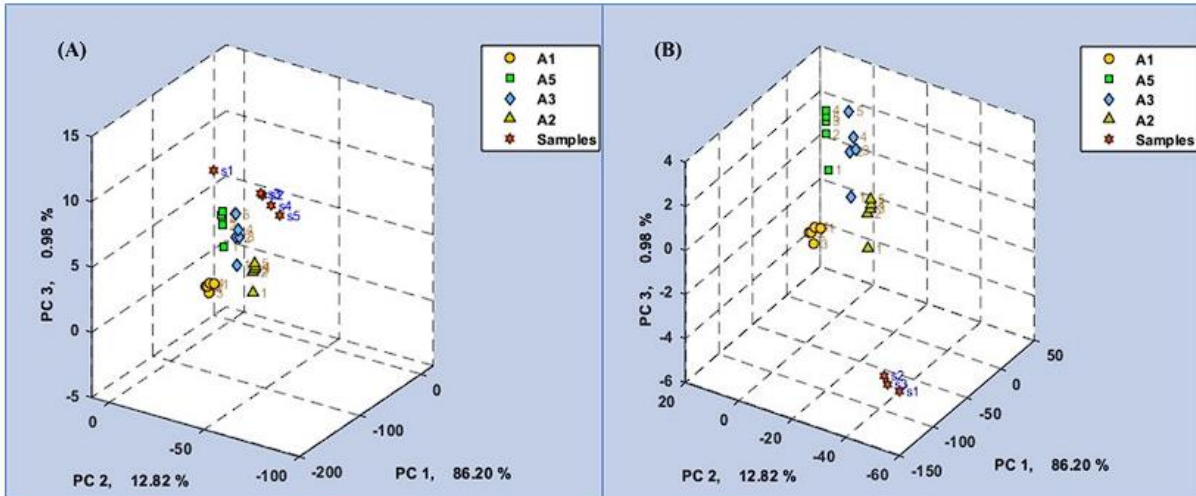
Figure 4.17 CDA plot (A) 2nd sample from A3 and (B) a 2nd sample from A2

4.12 Repeatability of Prediction Algorithms with Similar Components

A collection of identical samples was obtained from the PCB set comprising A7, A8, and A9 to evaluate the predictive repeatability of the E-nose, with a set of similar components from different avionics. A training set was constructed using singular measurements, and subsequent signatures from smoldering of similar samples were employed to verify the sample predictions. Figure 4.18 displays two samples from A8, both Pre and Post-thermal stress.
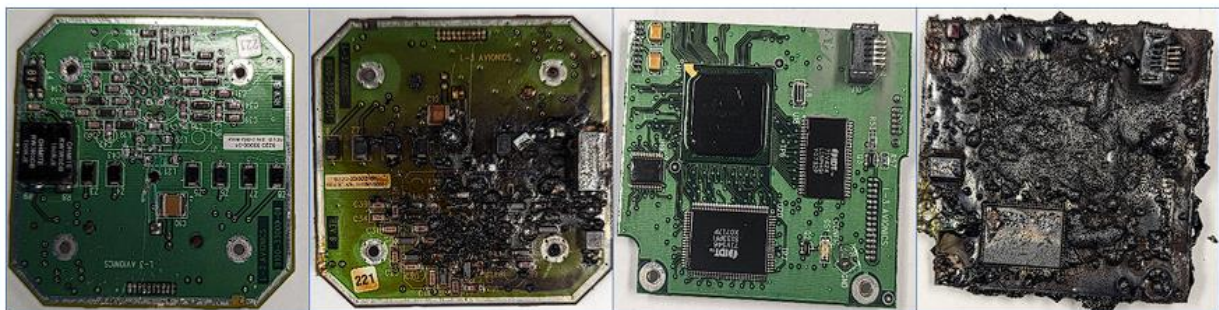
Figure 4.18 Sample A8 Pre and Post thermal stress

The training set, 'T3', derived from the sample set, achieved a prediction accuracy of 95% across all normalization methods with the data from all 32 sensors. The accuracy reached 100% upon excluding two sensors with an IIW value below 1.

For 'T3', made from a single training of 2 different samples from component A8 and 1 sample from A7, A9. For prediction, 1 sample from A7, A8, A8', and two others from A9 were used for collecting data for 5 prediction cycles. All the algorithms accurately matched the samples with their predecessors in the training set, suggesting a consistent signature and underscoring the repeatability of the E-nose in its predictions. However, one sample from the second set of A9 was misclassified by the KNN, CDA, and SIMCA algorithms. Figure 4.19 – Shows the Training and Prediction set in the PCA plot with all the sensor values chosen for the analysis.

	KNN	K-Means	CDA	SVM	SIMCA
A7	5/5	5/5	5/5	5/5	5/5
A8	5/5	5/5	5/5	5/5	5/5
A8'	5/5	5/5	5/5	5/5	5/5
A9	4/5	5/5	4/5	5/5	4/5

Table 4.14 Multivariate Analysis for 'T3' using Norm1, Autoscaling with all the sensor values
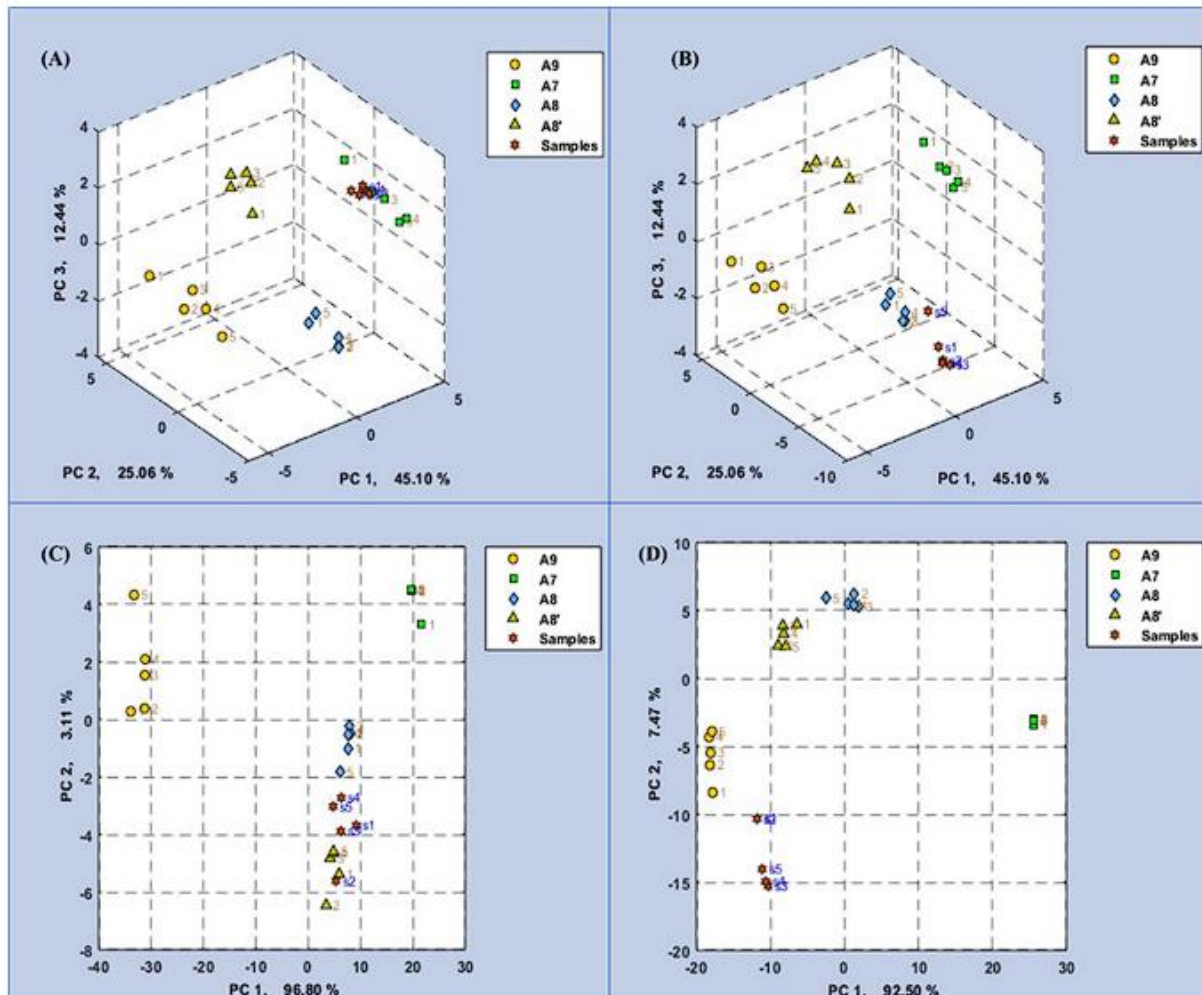
Figure 4.19 Prediction PCA plot for (A) Sample A7 (B) Sample A8 (C) Sample A8' and (D) Sample A9

4.13 Simplified Sensor Array Configurations with Printed Circuit Boards

As explored in the study by Ni et al. (2008), an abundance of signatures from various sensors can introduce a higher noise, leading to less precise predictions. To mitigate this, the IIW (weightage index algorithm) used in the Canonical Discriminant Analysis (CDA) proves beneficial in examining variance and filtering out sensors that contribute minimally to the discriminative analysis. An alternative approach focusing only on the MOS sensors, MOS sensors are widely used in gas detection applications. By focusing solely on the responses from 8 MOS sensors in the

predictive analysis for T3, the cross-validation achieved 100% prediction accuracy. Furthermore, every algorithm accurately predicted all samples, including the previously misclassified one sample from A9. This suggests the potential efficacy of E-nose systems with fewer sensors, emphasizing discriminative functions tailored for fire detection and the discrimination of signatures. Figure 4.20 – Shows the A7 and A9 sample prediction plots with only MOS sensors.
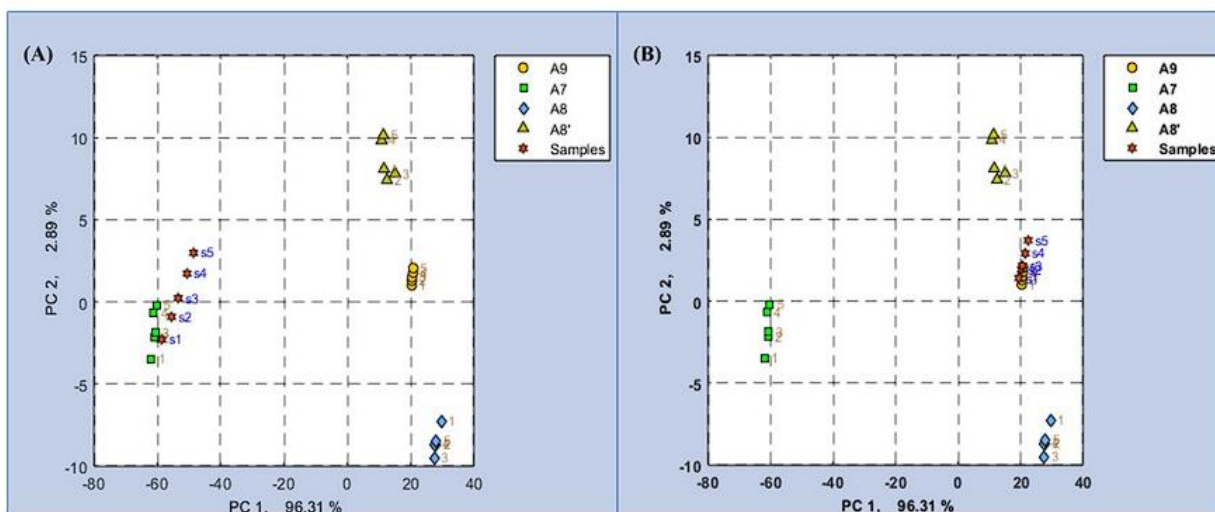
Figure 4.20 Prediction PCA Plot for Samples from A7 and A9 with values from only MOS sensors

4.14 Utilizing Classification Algorithms for Other Materials

In fire detection, interference from unrelated or nuisance sources presents a significant challenge. Such interferences often lead to false alarms, which, in turn, compromise the trustworthiness and reliability of detection systems. In this part of the study, materials not typically associated with internal contaminant sources, specifically 'bread' and 'hardwood,' are sourced locally, and three samples from both classes were induced thermal stress and subjected to predictive analysis, utilizing data for 2 prediction cycles. A new training set named 'T4', which consisted of Bread (BR), Hardwood (HW), A7 (PCB), A8 (PCB), B1 (PVC), and B2 (AP) were formed for this analysis. When this 'T4' set was evaluated, the KNN method displayed 100% correct-prediction

probability during the cross-validation, with data from all 32 sensors. However, with the analysis of the 'bread' and 'hardwood' samples, most algorithms successfully identified the 'bread' sample, but only the KNN method accurately recognized all the 'hardwood' samples, with all 32 sensor values used for the analysis.

Interestingly, when the data was limited to 8 MOS sensors, every algorithm accurately classified all the samples. However, the results were inconsistent when other sensor types like PID or EC were utilized for this specific training set in the E-nose. These findings indicate that a large dataset with closely related signatures from many sensors in multivariate analysis can introduce confusion, especially if the samples are sensitive to environmental changes. Nevertheless, carefully selecting appropriate sensors can enhance the system's predictive accuracy, offering a more dependable fire detection solution. Table 4.15 shows the analysis with all the sensors and Table 4.16 shows the analysis with using 8 MOS sensors.

	KNN	K-Means	CDA	SVM	SIMCA
HW	6/6	5/6	5/6	5/6	5/6
BR	6/6	6/6	6/6	5/6	5/6

Table 4.15 Multivariate Analysis for T4 using Norm2, Autoscaling with all the sensor values

	KNN	K-Means	CDA	SVM	SIMCA
HW	6/6	6/6	6/6	6/6	6/6
BR	6/6	6/6	6/6	6/6	6/6

Table 4.16 Multivariate Analysis for T4 using Norm2, Autoscaling with 8 MOS sensors

4.15 Classification Algorithms in Largescale Testing

In the large-scale testing, wire samples from four distinct insulation types utilized in aircraft were examined (Similar ones used in the UMD small-scale experiments, except for PVC cable) at the FAATC mockup flight deck facility. The data gathered from these samples were used to create a training set. Subsequently, another identical sample set was tested to obtain measurements to assess the predictions' accuracy, with data for 2 prediction cycles. The training set, 'TS-1', exhibited a cross-validation correction probability of 85% with the Norm1 technique, 90% with the Norm2 technique, and 85% without normalization, with all sensor values chosen for the cross-validation.

The cross-validation correct probability remained at 85% when the five sensors with an Important Index Weighting (IIW) of less than one was deselected. Consequently, the analysis proceeded with all sensors selected for both cross-validation and prediction. In the prediction evaluation employing the Norm2 technique, various classification methods yielded diverse results. The KNN algorithm accurately classified all eight samples. Conversely, the K-Means algorithm misclassified two AP and one ET sample. The CDA also incorrectly classified one AP sample. The SVM algorithm misclassified two AP and PT samples, and the SIMCA algorithm incorrectly classified two PT samples. Table 4.17 shows the detailed list of the analysis.

	KNN	K-Means	CDA	SVM	SIMCA
AP	4/4	2/4	2/4	0/4	4/4
ET (ETFE)	4/4	2/4	4/4	4/4	4/4
PT (PTFE)	4/4	4/4	4/4	0/4	0/4
PVC	4/4	4/4	4/4	4/4	4/4

Table 4.17 Multivariate Analysis with Norm2, Auto-scaling for TS-1 with all sensor values

4.16 Multivariate Analysis with Printed Circuit Boards in FAATC Tests

4 PCBs from different avionics were subjected to thermal stress in the FAATC setup, and the signatures were subjected to classification algorithms. The consistency of PCB samples still remained as a challenge, and for avionic samples, boards from the same equipment were subjected to testing multiple times for predictive analysis, and a flame retardant, Garolite, was used for repeated testing of an identical sample.

The training set, 'TS-2' from these four Printed Circuit board samples, exhibited a remarkable accuracy of 100% across all data scaling techniques, with all sensor values selected for cross-validation. The Important Index Weighting (IIW) recorded only one sensor value below 1, and its removal did not enhance the cross-validation results further. All employed classification algorithms successfully predicted all eight samples accurately. The consistent signatures recorded with the smoke trapped in the chamber facilitated the recording of uniform responses, significantly aiding the prediction process. Figure 4.21 visually represents the plots for the samples in the PCA space.

	KNN	K-Means	CDA	SVM	SIMCA
AC	2/2	2/2	2/2	2/2	2/2
AE	2/2	2/2	2/2	2/2	2/2
AF	2/2	2/2	2/2	2/2	2/2
FR	2/2	2/2	2/2	2/2	2/2

Table 4.18 Multivariate Analysis without any normalization, Auto-scaling for TS-2 with all sensor values
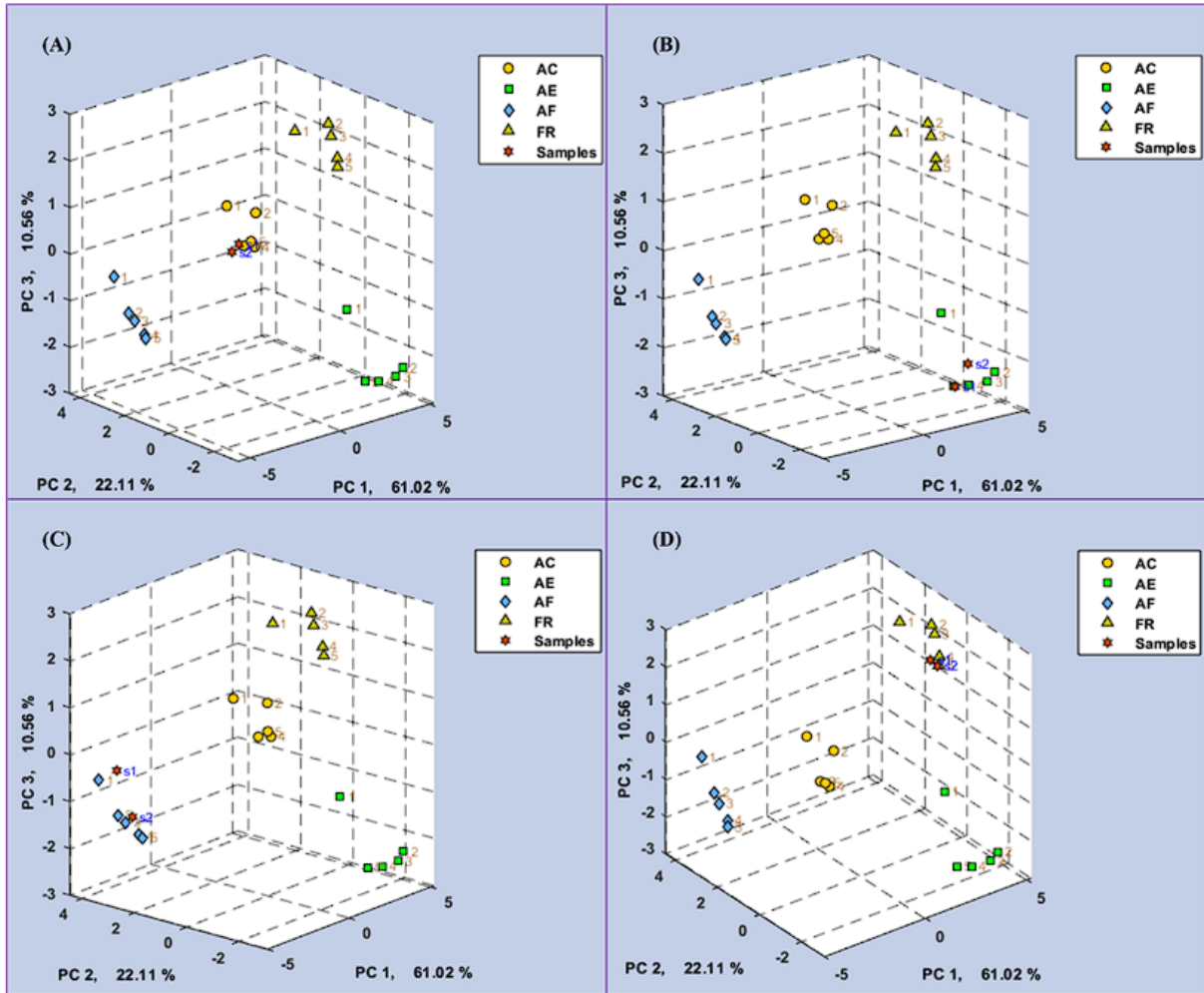
Figure 4.21 Canonical Plot with prediction samples for (A) AC, (B) AE, (C) AF, and (D) FR with training set TS-2

Two additional samples, sourced from the avionic AE, were subjected to prediction analysis to discern the similarity in signatures originating from diverse components of the same avionic equipment. As explained in Table 4.19, Signatures from one sample (denoted as AE') successfully aligned with the signatures from the training set when analyzed using the KNN, K-Means, and SIMCA algorithms. Conversely, the other sample did not exhibit a match with the training set, highlighting the variability in signatures across different components of the same avionics.

	KNN	K-Means	CDA	SVM	SIMCA
AE	0/2	0/2	0/2	0/2	0/2
AE'	2/2	2/2	0/2	0/2	2/2

Table 4.19 Multivariate Analysis with Norm1, Auto-scaling for TS-2 with all sensor values for additional samples

Six identical samples from the Fire Retardant Garolite board were subjected to the thermal setup, and signatures were analyzed with the 'FR' sample in 'TS-2' for prediction. All the produced samples measured from each FR board matched the Fire Retardant (FR) sample in the training set when all the sensor values were used for prediction using KNN, K-Means and SIMCA algorithms. This outcome robustly suggests the Electronic Nose's (E-nose) proficiency in accurately identifying the signatures.

	KNN	K-Means	CDA	SVM	SIMCA
FR1	5/5	5/5	0/5	0/5	5/5
FR2	5/5	5/5	0/5	0/5	5/5
FR3	5/5	5/5	0/5	0/5	5/5
FR4	5/5	5/5	0/5	0/5	5/5
FR5	5/5	5/5	5/5	0/5	5/5
FR6	5/5	5/5	5/5	5/5	5/5

Table 4.20 Multivariate Analysis with Norm1, Auto-scaling for TS-2 with all sensor values for similar FR samples

The samples were further explored by exclusively focusing on responses from the MOS sensors. When the Fire Retardant (FR) samples were subjected to cross-validation, they consistently exhibited 100% confidence across all data scaling techniques. The KNN and K-means algorithms adeptly identified all the samples correctly. The Canonical Discriminant Analysis (CDA) also correctly identified some previously misclassified samples (FR2 and FR3), enhancing the overall

accuracy. However, the SIMCA analysis encountered difficulties. This comprehensive analysis robustly supports employing a minimized sensor array with only MOS sensors for efficient and accurate detection and identification of early fire signatures. The accompanying figure 4.22 visually represents the plots for FR3 and FR5 with all sensor values Vs exclusively with MOS sensors.
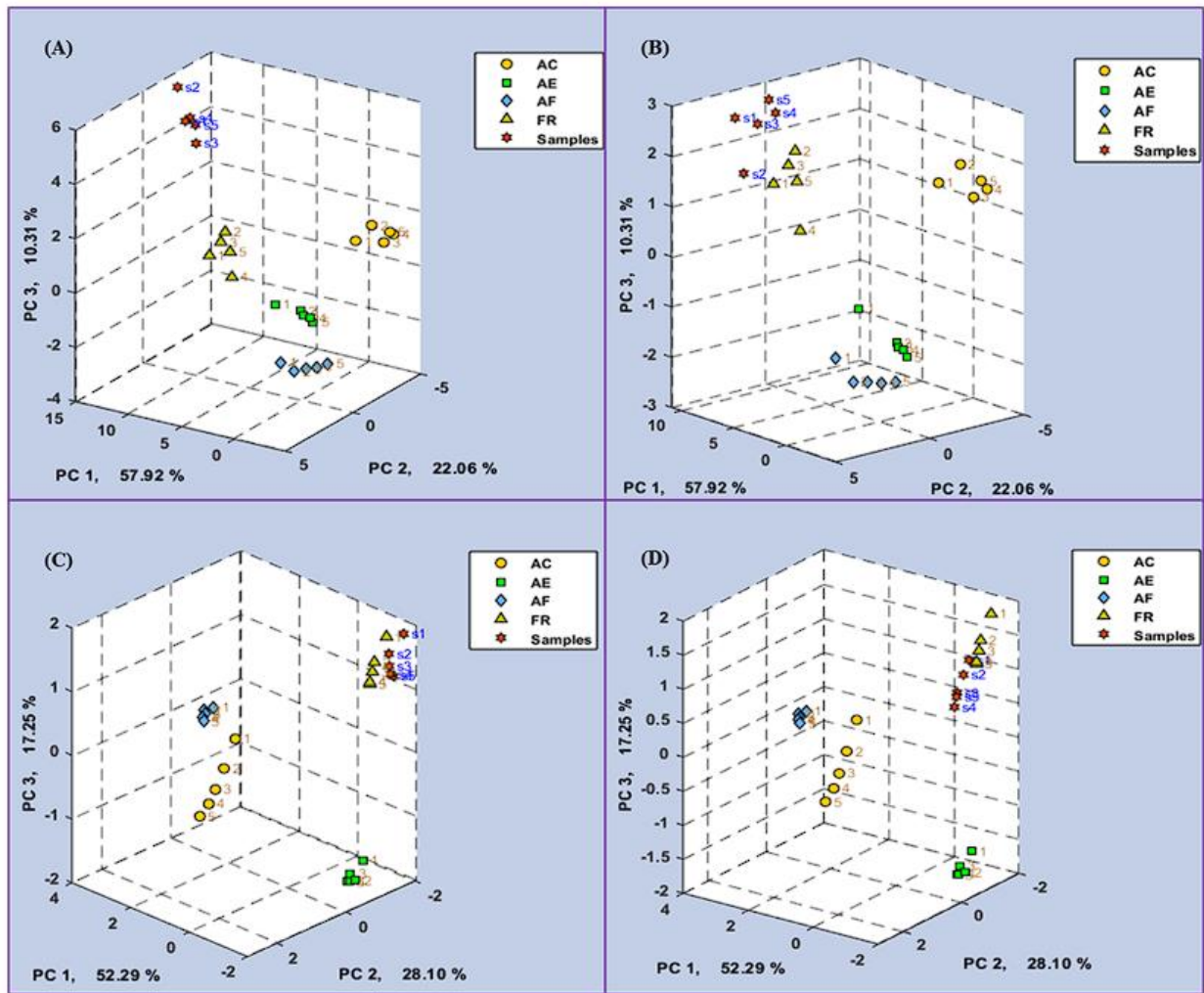

Figure 4.22 Canonical Plot with training set TS-2 for (A) FR3 with all sensor values, (B) FR5 with all sensor values, (C) FR3 with 8 MOS sensor values, and (D) FR5 with 8 MOS sensor

4.17 Classification Algorithms with Training Set Developed from Various Materials

A comprehensive new training set, 'TS-3', was developed, incorporating responses from two fan samples (BF and HWF) that were subjected to failure and responses from Hydraulic Oil (HY) and Jet Oil (JO) exposed to overheating using a hot plate. The FR and PVC sensor responses used to create the earlier training set were also included in TS-3. The cross-validation of this diverse training set yielded an 80% confidence with Norm1 and 86.7% with no-normalization. Remarkably, upon omitting 14 sensors with an Important Index Weighting (IIW) less than 1, the cross-validation confidence raised to 96.7% across all data-scaling techniques, highlighting the significant impact of selective sensor value inclusion on prediction accuracy. Further samples from the fan failure experiment and identical samples for the Hydraulic and Jet oil in the same heating setup were analyzed for predictions with 'TS-3'. Barring one instance with a HY sample in SIMCA, all algorithms correctly classified all the samples. This consistent accuracy was mirrored when only 8 MOS sensor responses were used for the analysis, akin to the earlier iteration.

Figure 4.23 provides a visual representation, showcasing the PCA plot for the training set with 8 MOS sensor values selected vs. the training set after the omission of 14 sensor values with IIW less than 1. The PCA score plot further illustrates closely aligned responses for the signatures from the fan samples. This alignment underscores the potential of employing training algorithms to develop extensive classes of similar samples for efficient and accurate identification on a large scale, suggesting similar signatures from the failures.

	KNN	K-Means	CDA	SVM	SIMCA
BF	2/2	2/2	2/2	2/2	2/2
HWF	2/2	2/2	2/2	2/2	2/2
JO	2/2	2/2	2/2	2/2	2/2
HY	2/2	2/2	2/2	2/2	0/2

Table 4.21 Multivariate Analysis with Norm1, Auto-scaling for TS-3 with only MOS Sensor Values
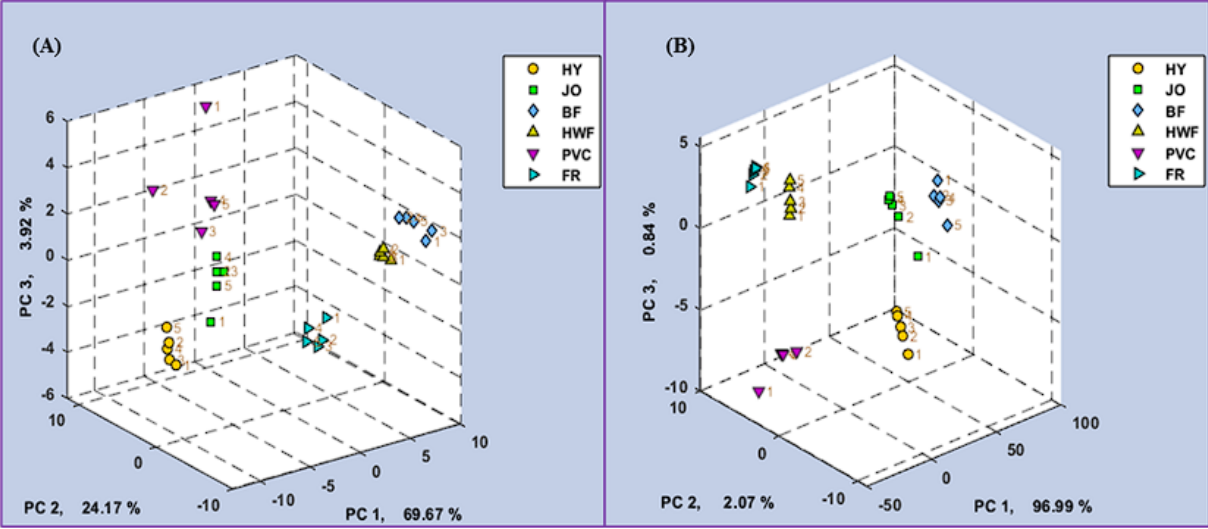
Figure 4.23 PCA score plot with (A) 18 sensor responses and (B) 8 MOS sensor responses

4.18 Performances of Classification Algorithms Under Reduced Pressure

An experiment was conducted within a low-pressure chamber at the FAATC to emulate the cabin pressure at 8000 ft and assess the functionality of the E-nose under high altitude conditions. To mitigate the impact of reduced pressure and facilitate the introduction of signatures to the sensor array, a 30 LPM diaphragm pump, and a flow control valve were employed upstream of the inline filter. The training set, TS-4, showed 100% confidence across all data-scaling techniques.

112

Further, additional prediction samples, denoted as FR' - signatures from the same FR board, FR" - A new similar FR board, exhibited perfect matches across all the algorithms. This outcome robustly suggests the adaptability and reliability of E-nose measurements across diverse environmental conditions, reinforcing the E-nose's potential as a versatile and dependable tool across different environments.

	KNN	K-Means	CDA	SVM	SIMCA
FR'	3/3	3/3	3/3	3/3	3/3
FR''	3/3	3/3	3/3	3/3	3/3

Table 4.22 Classification Algorithms with Norm1, Mean-centering for TS-4 with all Sensor Values

To check the similarity of signatures in various environments from similar samples. the Fire Retardant (FR) sample, tested under three distinct conditions - the UMD scale experiment, FAATC Mockup, and FAATC reduced pressure vessel- was subjected to predictive analysis to further explore the repeatability across diverse conditions. A new training set, 'TS-5' was constituted, incorporating values gathered during the FAATC mockup testing, including JO, PVC, AF, and FR samples.

FR1 sample encompassed signatures collated during the small-scale experiment, while FR2 comprised those obtained from the reduced pressure vessel using the earlier FR'. The cross-validation process yielded a 100% confidence level observed with both Norm2 and Norm1 techniques.

During the analysis, only the K-means algorithm correctly predicted both samples in the analysis where all sensor values were selected. Contrarily, all other algorithms faltered with inaccurate sample classification. Further exploration utilizing only eight MOS sensors also did not yield

favorable results. None of the algorithms correctly classified the sample from the reduced pressure test. However, K-means and Canonical Discriminant Analysis (CDA) adeptly classified the small-scale experiment sample.

This classification challenge is attributed to the substantial drift in individual sensor responses and baseline. Additionally, the reduced pressure test's distinct flow rate, differing from other setups, further compounded the classification complexity.

	KNN	K-Means	CDA	SVM	SIMCA
FR1	0/2	2/2	0/2	0/2	0/2
FR2	0/2	2/2	0/2	0/2	0/2

Table 4.23 Classification Algorithms with Norm2, Auto-scale for TS-4 with all Sensor Values

4.19 Application of Bosch BME688 for Predictive Analysis

The Bosch BME688 sensors played a crucial role in all the analyses conducted. These sensors were employed during small-scale experiments to gather comprehensive sensor information and gas channel data. The collected data was classified based on the sample type, providing a robust neural network training dataset.

Initially, attempts to train the sensor with various cable insulations for prediction within the different insulations in the experimental setup did not yield successful results. This led to a different approach, focusing on class preparation based on material types (e.g., Cable Insulation/Ambient Air / PCBs)and using it for predictive analysis of the sample. The neural network was then trained incrementally with each additional sample tested. The newly created classes included eight specimens for Ambient Air, eleven specimens for PCBs, and four for cables.

Class A consisted of Ambient Air specimens, Class B – Printed Circuit Boards, and Class C contained sensor responses for cable insulations.

A predefined neural network architecture tailored for the BME688 was employed, utilizing the ADAM optimizer with a batch size 32. This structured approach led to significant improvements in model performance. The trained algorithm consistently demonstrated an accuracy exceeding 95% across all four heater profiles, showcasing the effectiveness of the refined training and classification strategy.

Heater Profile and Duty Cycle	Accuracy	F1 Score	Miss Rate
HP-301 / RDC-1-0	99.75%	99.65%	0.33%
HP-354 / RDC-1-0	96.61%	94.43%	5.05%
HP-411 / RDC-1-0	96.36%	93.84%	5.56%
HP-501 / RDC-1-0	95.08%	91.84%	6.94%

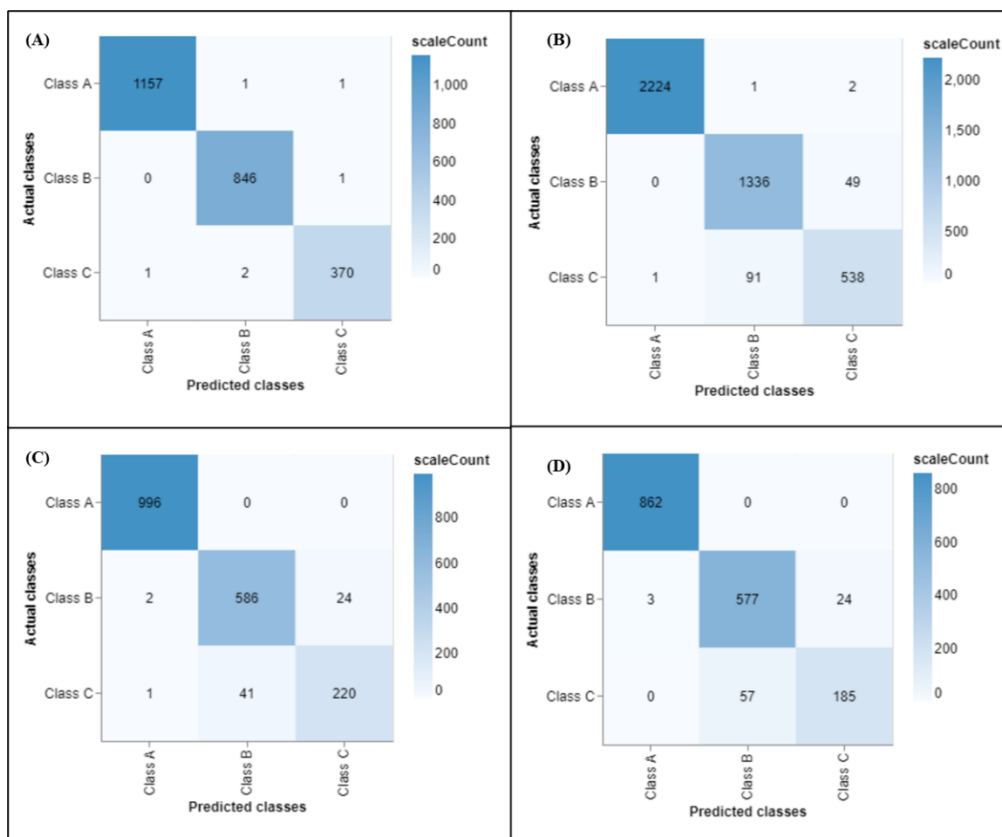Table 4.24 Algorithm evaluation parameters for different heater profiles

Figure 4.24 Confusion Matrix for (A) HP-301, (B) HP-354, (C) HP-411 and (D) HP-501

This algorithm was deployed during large-scale experiments conducted at the FAATC. During these tests, the BME688 sensor exhibited a delay ranging from 30 to 60 seconds between the appearance of visible smoke and the sensor's response to detect the samples. Despite this delay, the sensor successfully and accurately classified all the PCB samples in the mockup and reduced the pressure vessel as 'Board' (Class-B).

However, two cable types, PTFE and AP (Aromatic Polyamide), were incorrectly classified as 'Air' (Class – A) and 'Board' (Class-B). This misclassification could be attributed to the observations made during the gas analysis using the E-nose. It was noted that the signatures from both these cable types were significantly lower than other cable samples, which might have led to

116

their misidentification as air. The detailed prediction results with BME688 are presented in Table 4.25 for further reference and analysis.

Sample	Correct Class	Predicted Class
AE	Class - B	Class - B
AC	Class - B	Class - B
AF	Class - B	Class - B
FR	Class - B	Class - B
AP	Class - C	Class - B
ETFE	Class - C	Class - C
PTFE	Class - C	Class - A
PVC	Class - C	Class- C
Reduced Pressure Environment		
FR	Class – B	Class - B

Table 4.25 Prediction Results with the BME688 Algorithm

Even though the BME688 sensor failed to identify the elements within similar classes, integrating Artificial Intelligence (AI) capabilities is helpful in training the neural networks with a wide variety of samples. While the multi-sensor array E-nose successfully identified elements within different sets of classes, it faced challenges in applying training from one environment to predictions in another for similar samples. This transition introduced additional noise and confusion into the data, leading to inaccurate predictions.

5   CONCLUSION AND FUTURE WORK

The in-depth thermal impact and failure analysis of potential internal contaminant sources in aircraft, especially those from the cockpit, has yielded valuable insights into their behavior. A consistent observation across all samples showed elevated odor levels compared to ambient conditions, a trait also shown by the nuisance sources. While individual gases such as NH_3, Alcohol, CH_2O, and C_2H_4 exhibited minimal responses during testing, C_2H_4 levels were slightly higher than the rest. Interestingly, TVOC levels from printed circuit boards exceeded those from external contaminants like Jet Oil and Hydraulic Oil. However, they were lower than 'burned bread' and 'hardwood' levels, suggesting TVOC can be a potential marker to current smoke detection systems for improved alarm reliability.

When examining aviation cable insulation materials, PVC and ETFE insulations were more smoke-intensive than other materials. Even though ETFE insulation stood out for its resilience and integrity, PVC insulation deteriorated completely, although both produced considerable smoke during the induced failure using a high current setup. On the other hand, aromatic polyimide demonstrated reduced smoke emission and enhanced durability. The ASD system's promptness in detecting escalating smoke levels met anticipations set by the test volume and the system's aspiratory efficiency.

The minimal changes in CO, CO_2, and O_2 levels during the tests indicate that relying only on measuring these gases alone was not adequate for early detection of specific ICS events. Even with its limited aspirating capacity, the E-nose's performance was respectable, it also showed a faster response and sensor peak with a higher flow rate in the low-pressure vessel tests.

Exploratory algorithm studies revealed that incorporating all sensor responses from a conventional multi-sensor array may not be imperative for fire detection and discrimination. Implementing an approach with 8 MOS sensors or using the Important Index Weighing algorithms yielded superior results to configurations utilizing all 32 sensors in the array. This indicates the potential for adopting a more streamlined sensor array, which serves the primary objectives of fire detection and discrimination and offers advantages in data management, reduced sensor drift, and equipment maintenance. MOS sensors, while advantageous for their sensitivity, face critical limitations such as poor selectivity, which can lead to difficulty distinguishing target gases from other substances, resulting in false positives. Additionally, MOS sensors can suffer from aging effects, leading to a decline in sensitivity over time, and may experience sensor drift, necessitating regular calibration to maintain accuracy. Despite these limitations, MOS sensors are still popular because of their low cost and ability to detect a wide range of gases.

The intelligent algorithms' performance was closely tied to the variance and consistency of sensor responses inherent in the developed training datasets. Training sets derived from averaged sample values produced more dispersed canonical plots and less precise predictions than those constructed from singular specimen values. In the small-scale tests with various samples, using all 32 sensors, K-Means achieved the highest accuracy at 98%, followed by CDA at 97.4%, SIMCA at 96.8%, KNN at 92.9%, and SVM at 94.9%. When the analysis was narrowed down by either the 8 MOS sensors or using the IIW matrix, every algorithm reached a perfect 100% accuracy. For the large-scale tests, KNN led with an accuracy of 96.5%, trailed by both K-Means and SIMCA at 89.6%, CDA at 55%, and SVM at 36.2%. When the focus was shifted to only the MOS sensors, which were selected based on their enhanced cross-validation probability relative to the full sensor set, every algorithm demonstrated 100% accuracy. K-Means was the sole algorithm that consistently

and accurately predicted samples from diverse testing conditions using chemometric analysis, suggesting its potential as the optimal choice for quick analysis and discrimination of ICS sources. While similar samples, like PCB and aviation cables, exhibited comparable signatures, there was also a marked difference in signatures from different samples within a single avionic equipment. This underscores the need for a diverse training dataset and the possible challenges of diverse signatures from different parts of the same PCB / avionic.

The BME688 sensor, with a single MOS sensor, effectively categorized distinct classes, especially those that produced considerable markers, but faced challenges in differentiating various samples within classes. The AI capabilities through the BME688 AI studio were highly helpful in training the neural network with a new sample.

In practical applications, classifying similar samples into shared categories and using an optimized metal oxide sensor array with machine learning techniques can strengthen the reliability of alarms, facilitate the identification of combusting materials, and reduce false alarms. For practical implementations, it is essential to adopt advanced machine learning methods, like those found in the BME AI Studio, for training sensors across a range of conditions and target environments rather than solely relying on a direct multivariate approach.

This research has been limited to experiments involving a single type of sample subjected to thermal stress. Future studies could expand on this by examining multiple similar samples or nuisance sources subjected to thermal stress together. Utilizing data from these experiments for production would enable an evaluation of the algorithms' ability to identify each sample accurately. Additionally, it would offer insight into how the correct prediction rates are influenced by the presence of multiple sources and whether the algorithms can effectively distinguish between them in a more complex detection environment. Future works can explore combining machine learning

with multi-gas sensors, especially when paired with existing fast detection methods. A deeper dive into the specific gases released from signature ICS can provide insights into their potential as unique markers. While detecting gases from every individual ICS might be challenging due to their wide variety, a broader strategy could involve training sensors on gases from similar ICS types and examining their response parameters.
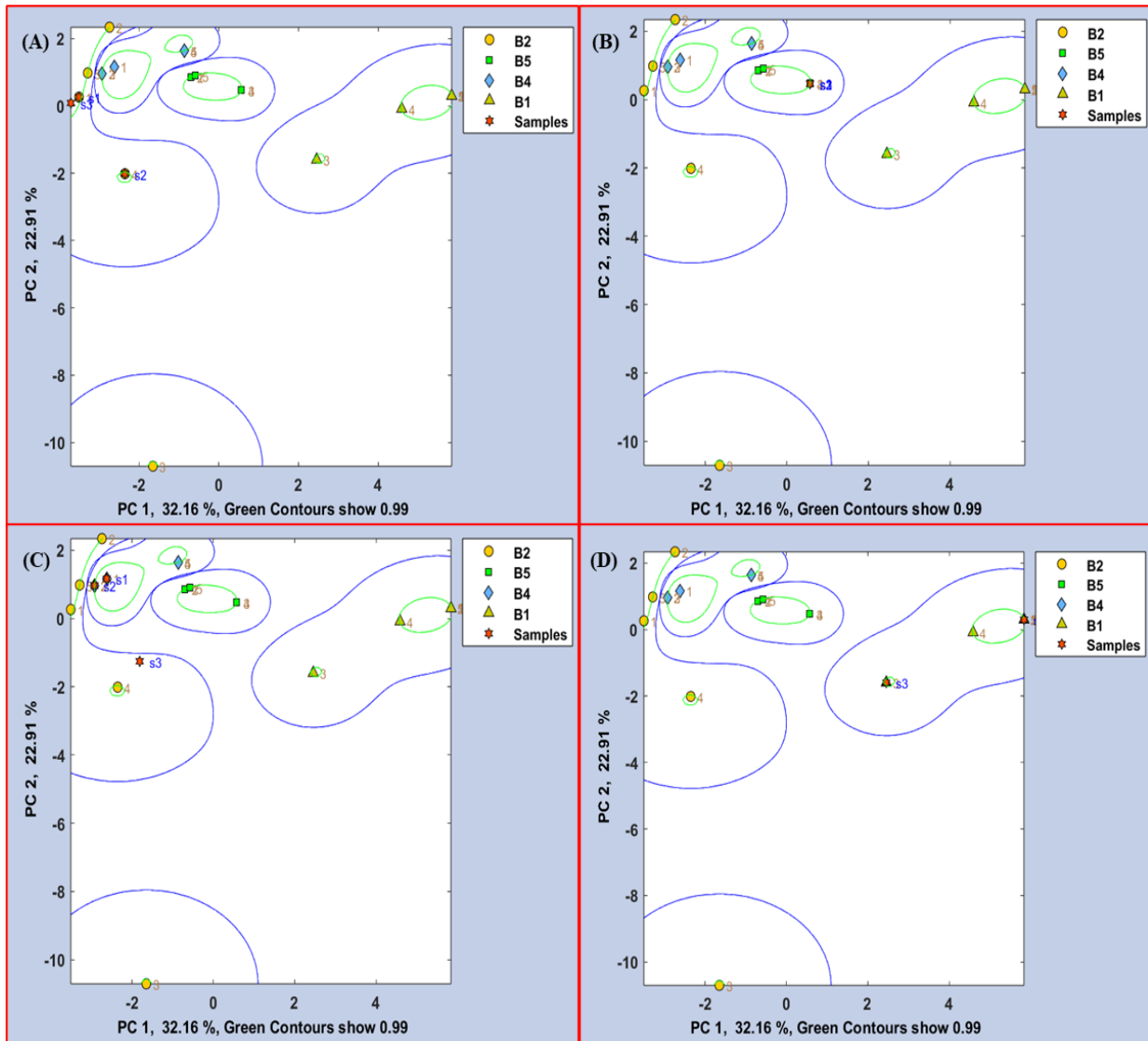
6   Appendix

Figure 6.1 SVM Plot with Autoscale and norm1 scaling for various cable samples with Training Set-1 - (A) Aromatic Polyimide, (B) ETFE, (C) PTFE, and (D) PVC. Contour lines delineate SVM boundaries.

TEST MATRIX		
SAMPLE	**FAA**	**UMD**
Printed Circuit Board		
200-09058-000		X
634-2698-002		X
105-02307-00		X
153-018105-02		X
634-3517-005		X
440-00059-03		X
NEC, NL10276BC20-04		
Multi-Function Displays		X
105-02133-00		X
FR-4 1/8"	X	X
105-01134-00 Ver 3	X	
105-02109-00 Ver 1	X	
S4151-009060720020	X	
Wire Samples		
M81381 / 12-20	X	X
M22759/ 34-16-9	X	X
BMS13-60-19	X	X
M5086/1-22-9	X	
55A0811-20-9		X
PVC 10/0.1 Equip Wire		X
Other Materials		
Jet Oil	X	
Hydraulic Oil	X	
Hardwood		X
Bread		X
FAN SAMPLES		
645405-1	X	
4100941D	X	

Table 6.1 Test Matrix

Figure 6.2 Xtralis Test Transformer used for cable failure tests

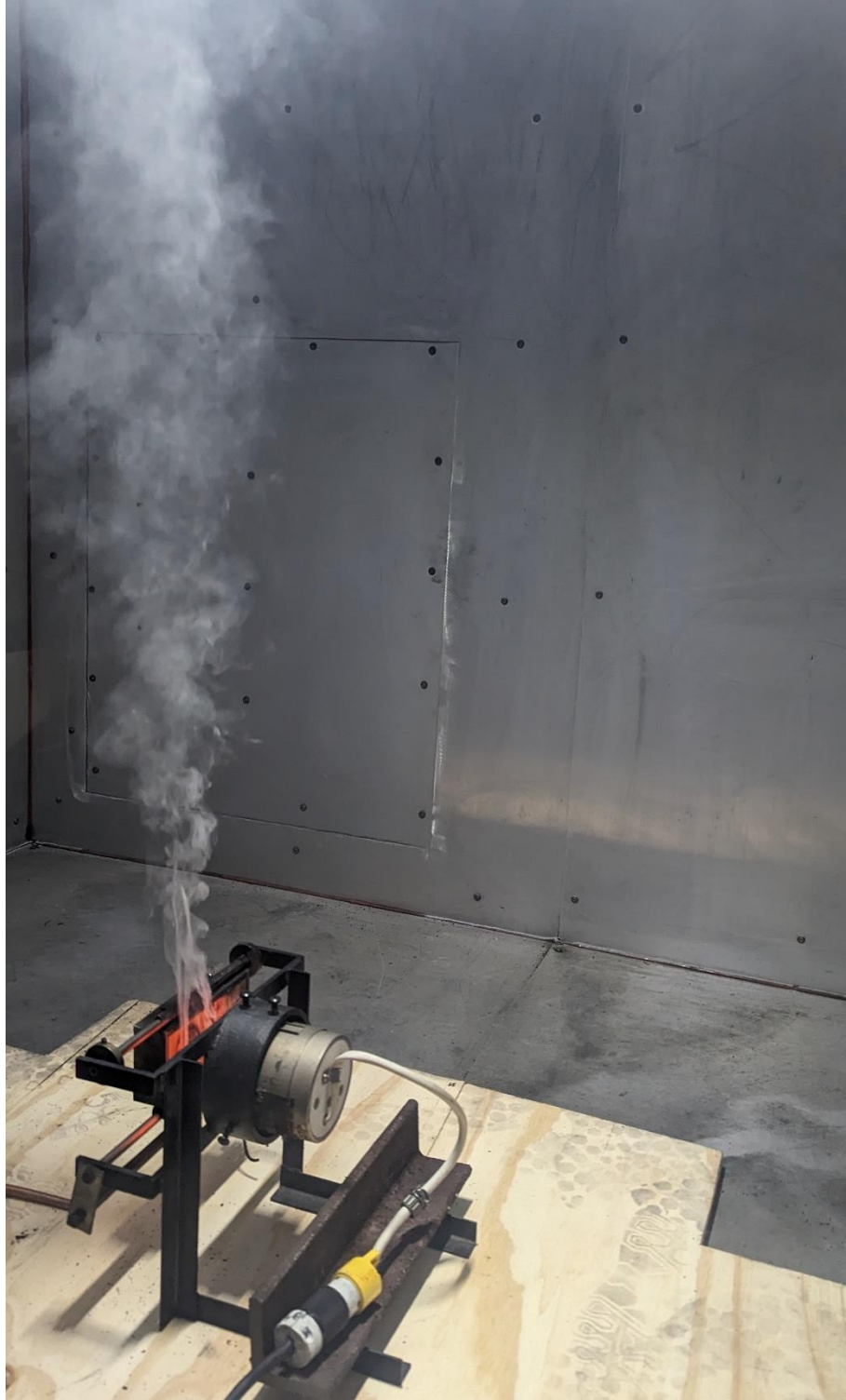Figure 6.3 ASTME662 chamber used for UMD tests
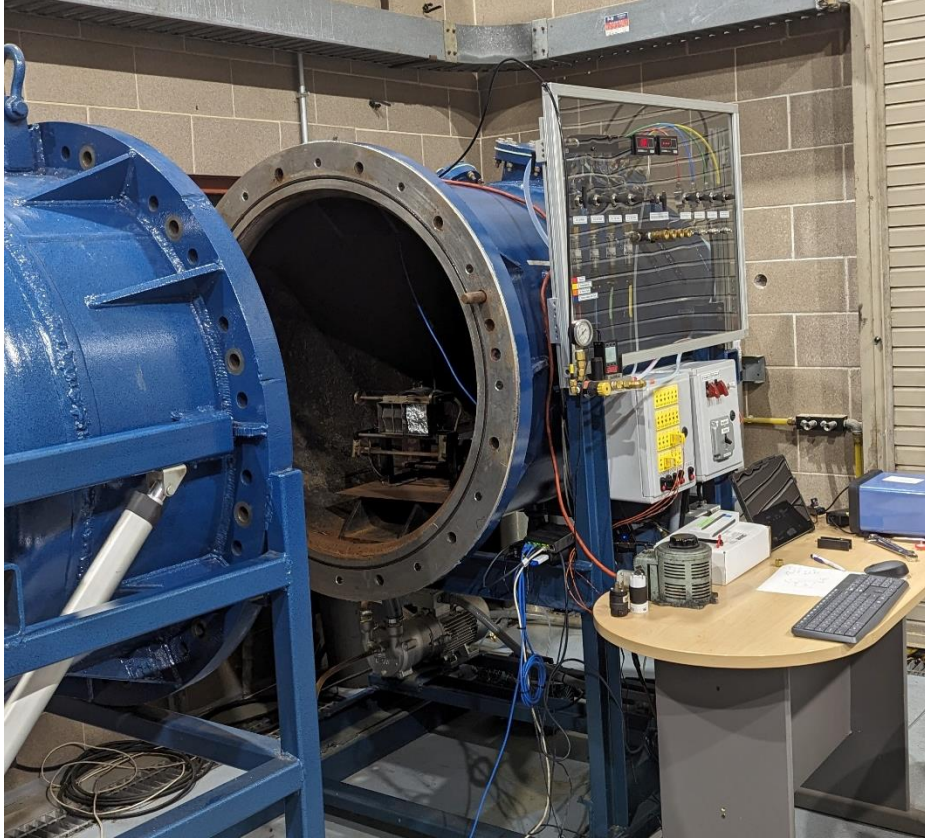
Figure 6.4 Inside view from the FAA box during testing
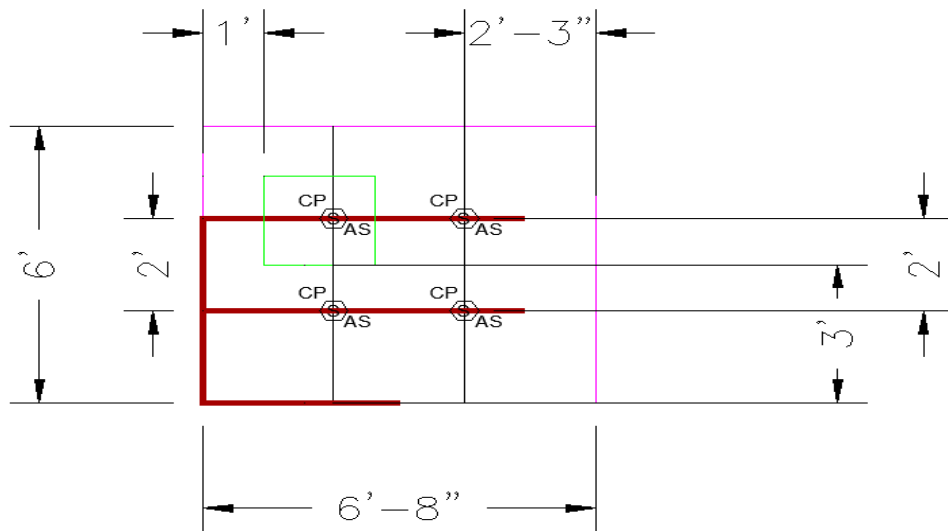
Figure 6.5 Low-Pressure Vessel at FAATC

Figure 6.6 VESDA Piping top view by Xtralis

7   REFERENCES

- Cherry, R.G.W. & Associates Limited. (2017). Research Into Fire, Smoke or Fumes Occurrences on Transport Airplanes (DOT/FAA/TC-16/49). https://www.fire.tc.faa.gov/pdf/TC-16-49.pdf

- Cestari, L. A., Worrell, C. L., & Milke, J. A. (2005, February 1). *Advanced fire detection algorithms using data from the home smoke detector project*. Fire Safety Journal; Elsevier BV. https://doi.org/10.1016/j.firesaf.2004.07.004

- Breznitz, S. (1984). *Cry Wolf: The Psychology of False Alarms*. Hillsdale, N.J.: Lawrence Erlbaum Associates. https://doi.org/10.4324/9780203781203

- Bukowski, R., Mulholland, G. W., & Center for Fire Research (U.S.) (1978). *Smoke Detector Design and Smoke Properties*. Washington: Dept. of Commerce, National Bureau of Standards, National Engineering Laboratory, Center for Fire Research. (NBS Technical Note; 973). https://doi.org/10.6028/nbs.tn.973

- Karp, M.E., 2017. 'False Alarm Smoke Detection and Smoke Generators', paper presented at the International Aircraft Systems, November 2017, DOI: 10.13140/RG.2.2.30256.58881

- Hagen, B.CHR. and Milke, J.A., 2000. The use of gaseous fire signatures as a mean to detect fires. *Fire Safety Journal*, 34(1), pp.55-67. Available at: https://doi.org/10.1016/S0379-7112(99)00046-6

- Klote, J.H. and Milke, J.A. (2002) *Principles of Smoke Management*. American Society of Heating, Refrigerating and Air-Conditioning Engineers & Society of Fire Protection Engineers, Atlanta.

- National Fire Protection Association (NFPA) (2019). *NFPA 72: National Fire Alarm and Signaling Code*.

- Gaur, A., Singh, A., Kumar, A., Kumar, A., & Kapoor, K. (2020). Video Flame and Smoke Based Fire Detection Algorithms: A Literature Review. *Fire Technology*, 56, 1943-1980. https://doi.org/10.1007/s10694-020-00986-y

- Taylor, G., Cooper, S., D'Agostino, A., Melly, N., & Cleary, T., 2016. *Determining the Effectiveness, Limitations, and Operator Response for Very Early Warning Fire Detection Systems in Nuclear Facilities*. U.S. Nuclear Regulatory Commission & National Institute of Standards and Technology, September.

- Sensigent, n.d. [Online]. Available at: https://www.sensigent.com/software.html (Accessed Aug, 2023).

- FAA Reauthorization, 2018. *Interim Report on Aircraft Air Quality*, Section 326 Aviation Safety. Page 6 of 17. Issued on November 2020.

- Kos, J. et al., 2018. *On-board air quality - Final Report*. EREA.

- Milke, J.A. et al., 2008. *Validation of a Smoke Detection Performance Prediction Methodology*. Fire Protection Research Foundation.

- Fabian, T.Z. and Gandhi, P.D., 2007. *Smoke Characterization Project*. UL.

- Overfelt, R.A. and Jones, B.W., 2012. *Sensors and Prognostics to Mitigate Bleed Air Contamination Events: 2012 Progress Report*.

- Milke, J. and Zevotek, R., 2016. *Analysis of the Response of Smoke Detectors to Smoldering Fires and Nuisance Sources*. *Fire Technology*,52,pp.1235–1253.Available at: https://doi.org/10.1007/s10694-015-0465-2.

- Milke, J.A., 1999. Monitoring Multiple Aspects of Fire Signatures for Discriminating Fire Detection. *Fire Technology*, 35(3).

- Ramesham, R., 2001. *Detection of Outgassing Species from the Electrical Insulators Using Cyranose E-Nose.* Jet Propulsion Laboratory.

- Fujinaka, T., Yoshioka, M., & Omatu, S. (2008). Intelligent Electronic Nose Systems for Fire Detection Systems Based on Neural Networks. In *The Second International Conference on Advanced Engineering Computing and Applications in Sciences*. Graduate School of Engineering, Osaka Prefecture University, Osaka, Japan

- Scorsone, E., Pisanelli, A.M. & Persaud, K.C. (2006). Development of an electronic nose for fire detection. *Sensors and Actuators B: Chemical*, 116(1–2), pp.55-61. https://doi.org/10.1016/j.snb.2005.12.059.

- Ni, M., Stetter, J. R., & Buttner, W. J. (2008). Orthogonal gas sensor arrays with intelligent algorithms for early warning of electrical fires. *Sensors and Actuators B: Chemical*, 130(2), 889-899. https://doi.org/10.1016/j.snb.2007.10.070.

- CEN (2022) *EN 13725:2022 Stationary source emissions - Determination of odour concentration by dynamic olfactometry and odour emission rate*. Available at: https://standards.iteh.ai/catalog/standards/cen/67f31e88-f81d-4e78-bbf6-ce1dcb766eeb/en-13725-2022 (Accessed: Sept 2023)

- UL (2023) *UL 268, 8th Edition, UL Standard for Safety Smoke Detectors for Fire Alarm Systems*

- ASTM (2021) *ASTM E662-21AE01 Standard Test Method for Specific Optical Density of Smoke Generated by Solid Materials*. DOI: 10.1520/E0662-21AE01

- ASTM (2018) *ASTM E544-18 Standard Practice for Referencing Suprathreshold Odor Intensity*. DOI: 10.1520/E0544-18. Available at: https://doi.org/10.1520/E0544-18